NUREG/CR-5854

# Universal Treatment of Plumes and Stresses for Pressurized Thermal Shock Evaluations

Prepared by
T. G. Theofanous, S. Angelini, H. Yan

Department of Chemical and Nuclear Engineering
Center for Risk Studies and Safety
University of California at Santa Barbara

Prepared for
U.S. Nuclear Regulatory Commission

NUREG/CR-5854

# Universal Treatment of Plumes and Stresses for Pressurized Thermal Shock Evaluations

Prepared by
T. G. Theofanous, S. Angelini, H. Yan

Department of Chemical and Nuclear Engineering
Center for Risk Studies and Safety
University of California at Santa Barbara

Prepared for
U.S. Nuclear Regulatory Commission

## AVAILABILITY NOTICE

Availability of Reference Materials Cited in NRC Publications

Most documents cited in NRC publications will be available from one of the following sources:

1. The NRC Public Document Room, 2120 L Street, NW., Lower Level, Washington, DC 20555

2. The Superintendent of Documents, U.S. Government Printing Office, P.O. Box 37082, Washington, DC 20013-7082

3. The National Technical Information Service, Springfield, VA 22161

Although the listing that follows represents the majority of documents cited in NRC publications, it is not intended to be exhaustive.

Referenced documents available for inspection and copying for a fee from the NRC Public Document Room include NRC correspondence and internal NRC memoranda; NRC bulletins, circulars, information notices, inspection and investigation notices; licensee event reports; vendor reports and correspondence; Commission papers; and applicant and licensee documents and correspondence.

The following documents in the NUREG series are available for purchase from the GPO Sales Program: formal NRC staff and contractor reports, NRC-sponsored conference proceedings, international agreement reports, grant publications, and NRC booklets and brochures. Also available are regulatory guides, NRC regulations in the *Code of Federal Regulations*, and *Nuclear Regulatory Commission Issuances*.

Documents available from the National Technical Information Service include NUREG-series reports and technical reports prepared by other Federal agencies and reports prepared by the Atomic Energy Commission, forerunner agency to the Nuclear Regulatory Commission.

Documents available from public and special technical libraries include all open literature items, such as books, journal articles, and transactions. *Federal Register* notices, Federal and State legislation, and congressional reports can usually be obtained from these libraries.

Documents such as theses, dissertations, foreign reports and translations, and non-NRC conference proceedings are available for purchase from the organization sponsoring the publication cited.

Single copies of NRC draft reports are available free, to the extent of supply, upon written request to the Office of Administration, Distribution and Mail Services Section, U.S. Nuclear Regulatory Commission, Washington, DC 20555.

Copies of industry codes and standards used in a substantive manner in the NRC regulatory process are maintained at the NRC Library, 7920 Norfolk Avenue, Bethesda, Maryland, for use by the public. Codes and standards are usually copyrighted and may be purchased from the originating organization or, if they are American National Standards, from the American National Standards Institute, 1430 Broadway, New York, NY 10018.

## DISCLAIMER NOTICE

This report was prepared as an account of work sponsored by an agency of the United States Government. Neither the United States Government nor any agency thereof, or any of their employees, makes any warranty, expressed or implied, or assumes any legal liability of responsibility for any third party's use, or the results of such use, of any information, apparatus, product or process disclosed in this report, or represents that its use by such third party would not infringe privately owned rights.

NUREG/CR-5854
R4

# Universal Treatment of Plumes and Stresses for Pressurized Thermal Shock Evaluations

Manuscript Completed: May 1991
Date Published: June 1992

Prepared by
T. G. Theofanous, S. Angelini, H. Yan

Department of Chemical and Nuclear Engineering
Center for Risk Studies and Safety
University of California
Santa Barbara, CA 93106

**Prepared for**
**Division of Systems Research**
**Office of Nuclear Regulatory Research**
**U.S. Nuclear Regulatory Commission**
**Washington, DC 20555**
**NRC FIN D1634**

# ABSTRACT

The thermal field in a reactor vessel downcomer and resulting thermal/stress response in the adjacent reactor vessel wall during high-pressure safety injection are examined, especially with regard to departures from one-dimensional behavior. Similarity solutions for the stratification (in the cold leg) that creates the downcomer plumes, and scaling considerations for the thermal conduction and stress fields in the vessel wall are developed to provide generalized criteria for the adequacy of the one-dimensional treatment.

# TABLE OF CONTENTS

## LIST OF FIGURES

## LIST OF FIGURES (cont.)

## LIST OF TABLES

## ACKNOWLEDGMENTS

The thermal mixing aspects of this work derive from previous work sponsored by the U.S. Nuclear Regulatory Commission.

# NOMENCLATURE

| | |
|---|---|
| $A_i$ | cross-section area of system component $i$ |
| $a$ | minor ellipse semiaxis |
| $b$ | major ellipse semiaxis |
| $c_p$ | specific heat |
| $D$ | diameter of cold leg |
| $D^*$ | $= D_{CL}/D_{HPI}$ diameter ratio |
| $D_i$ | diameter of fluid stream, or system component $i$ |
| $d^*$ | $= d_e/D_{CL}$ |
| $d_i$ | depth of fluid stream $i$ |
| $E$ | Young's modulus |
| $\mathrm{Fr}_i$ | $= U_i\{D_i g\Delta\rho/\rho\}^{-1/2}$, Froude number of stream $i$ |
| $\mathrm{Fr}_{HPI,CL}$ | $= (Q_{HPI}/A_{CL})\left\{gD_{CL}\frac{\Delta\rho}{\rho}\right\}^{-1/2}$, superficial Froude number in the cold leg |
| $g$ | acceleration due to gravity |
| $h$ | heat transfer coefficient |
| $k$ | thermal conductivity |
| $L, \ell$ | vertical distance from cold-leg centerline in downcomer toward lower plenum |
| $\dot{m}_{HPI}$ | $HPI$ mass flow rate |
| $Q_i$ | volumetric flow rate of stream $i$ |
| $Q^*$ | $= Q_e/Q_{HPI}$ dimensionless entrainment rate |
| $T$ | temperature |
| $t$ | time |
| $U_i$ | velocity of fluid stream $i$ |
| $V$ | volume of the whole system |
| $x$ | horizontal distance from the cold-leg centerline in downcomer |

## Greek

| | |
|---|---|
| $\alpha$ | coefficient of thermal expansion, or thermal diffusivity |
| $\beta$ | fraction of entrainment from downcomer side |
| $\Delta T$ | temperature difference |
| $\Delta_{ij}$ | $\rho_i - \rho_j$ where $_{i,j}$ the two streams to which Fr is referred to |
| $\delta$ | thermal penetration length |
| $\zeta$ | elongation of the plume |
| $\theta$ | $= \frac{T_m - T}{T_m - T_j}$, dimensionless temperature |
| $\xi$ | thickness of vessel wall |
| $\rho_i$ | density of the fluid stream $i$ |
| $\rho^*$ | $= \rho_h/\rho_{HPI}$ |
| $\tilde{\rho}$ | $= \rho_m/\rho_{HPI}$ |
| $\sigma$ | stress |
| $\tau$ | characteristic time scale |

## Subscripts

| | |
|---|---|
| $c$ | cold stream, or conduction |
| $CL$ | cold leg |
| $e$ | entrainment |

## NOMENCLATURE (cont.)

| | |
|---|---|
| $HPI$ | high pressure injection |
| $h$ | hot stream |
| $j$ | the position of $2D_{CL}$ from cold-leg centerline down into the downcomer |
| $m$ | well mixed or "ambient" |
| $o$ | initial |
| $p$ | thermal penetration |
| $s$ | system |
| $x$ | horizontal coordinate |
| $y$ | vertical coordinate |

# 1. INTRODUCTION

Thermally-induced stresses in a reactor pressure vessel (RPV) wall, as a result of high-pressure safety injection (HPI) are an essential component of integrated risk analyses of pressurized thermal shock (PTS) transients (Selby et al. 1985a, Selby et al. 1985b). Limiting cooldowns (i.e., the most severe conditions) arise when this injection occurs under stagnated loop conditions (loss of natural circulation due to voiding in the steam generator tubes) which, in turn, corresponds to a rather narrow range* (in size) of small-break loss-of-coolant accidents (Theofanous et al 1989). For a given system the actual break sizes in this range can be determined from the HPI pump characteristic. This characteristic also ties in the corresponding injection flow rates and system pressures which are the key parameters concerning cooldown and state of stress.

Even though the net loop flow is zero, the cold safety injection causes a recirculating flow pattern that involves (in mixing) all parts of the primary system that can be reached from the point of injection by a sequence of horizontal and *downwards* vertical traverses (Theofanous & Nourbakhsh 1982, Theofanous & Iyer 1987). The recirculation, which is schematically illustrated in Figure 1, has been shown to have a drastic moderating effect on the global cooldown, as well as on the degree of stratification. The global cooldown is referred to the decrease of $T_m$, the mixed mean temperature, which physically represents the fluid temperature in the lower plenum, and in the downcomer outside the plume regions. The degree of stratification refers to the temperature difference between the hot and cold streams in the cold leg. In practice, the hot stream temperature is close to $T_m$; thus the degree of stratification reflects also the initial "strength" of cold plume created by the spilling of the cold stream into the downcomer. This flow, and thermal field, structure is the basis of the Regional Mixing Model (RMM), and the associate computer programs, REMIX and NEWMIX, utilized in the NRC Integrated PTS study (Iyer & Theofanous 1991a), and it has been confirmed experimentally (Iyer & Theofanous 1985, Iyer & Theofanous 1991b); a comprehensive comparison with data in experimental simulations ranging from 1/5 to full scale has been compiled recently (Theofanous & Yan 1991).

For the IPTS plants (Calvert Cliffs, H.B. Robinson and Oconnee) the degree of stratification was found to be minimal, and this behavior is expected to be applicable to the vast majority of US-designed plants (Iyer & Theofanous 1991a). Quantitatively, this stratification behavior, along with the predicted cooldown, can be summarized in the form of Figures 2 and 3 (for a Calvert Cliffs example), which provide the boundary conditions for the stress analysis. The significance of $T_j$ in Figure 2 (refer to Figure 1 also) is that it characterizes, in an approximate fashion, the "source" of the planar downcomer plume. Guided by experimental data, this "source" point is taken at 2 cold leg diameters below the cold-leg centerline (Iyer & Theofanous 1991a). Below this point the cold plume decays in the manner shown in Figure 3 (obtained from well-known plume decay laws, i.e., Turner 1973). Above it there is a very complex, three-dimensional, temperature/flow distribution and mixing pattern that although unknown in detail seems to have been adequately characterized as producing an equal volume mixing between the cold stream and the ambient downcomer fluid (this is how $T_j$ is computed). As a rough approximation

* In general, larger breaks lead to system depressurization, while for smaller breaks the HPI is sufficient to collapse the steam generator tube voids leading to reestablishment of natural circulation. The former case is clearly of no interest to PTS, while the latter leads to cooldown significantly less severe since both decay heat and the secondary side of the steam generators are now coupled to the thermal response of the downcomer region.

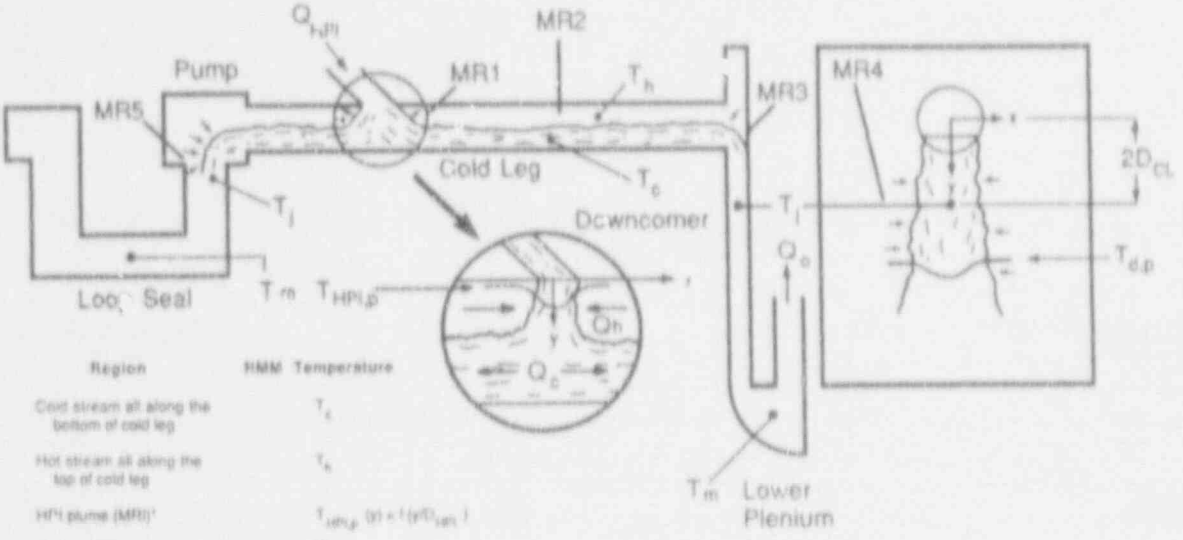


| Region | RMM Temperature |
|---|---|
| Cold stream all along the bottom of cold leg | $T_c$ |
| Hot stream all along the top of cold leg | $T_h$ |
| HPI plume (MR1)* | $T_{HPI,p}(y) = f(\dot{y}^2)_{HPI}$ |
| Pump (MR5) | $T_j$ |
| Loop Seal | $T_m$ |
| Downcomer plume at MR3 | $T_j$ |
| Downcomer plume (MR4)** | $T_{d,p}(0,y) = g(\dot{y}^2)_{DC}$ |
| Outside of downcomer plume | $T_m$ |
| Lower plenum | $T_m$ |

* Mixed mean temperature is computed using entrainment as a function of y and $Fr_{HPI}$

** This temperature is the lowest for the given level

Figure 1. Schematic representation of the Regional Mixing Model (RMM).

in REMIX/NEWMIX, the temperature field in this region is obtained by linear interpolation between $T_c$ and $T_j$.

In the IPTS, the stress analysis was carried out in a one-dimensional (1D) approximation believed to conservatively bound the stresses everywhere in the RPV wall (Cheverton et al. 1984, Selby et al. 1985a, Selby et al. 1985b). Specifically, the $T_j$ transient was applied, through a heat transfer coefficient, *everywhere* on the inside of the RPV wall, which was taken as a complete cylinder (i.e., without the cold-leg openings). In practice, conduction controls and the procedure is tantamount to imposing (within a few degrees) the $T_j$ transient directly on the inside face of the RPV wall.

A recent publication (Neubrech et al. 1988) strongly questions this procedure and provides analyses which in comparison with data from a full-scale "simulation" imply that the above-described 1D treatment may be highly non-conservative. This, in turn, has created intense concerns about the validity of the IPTS study. The IPTS study, through regulatory guides, has become a sort of prototype for future ones expected to be numerous, in the years to come, as plants age and come up against the specified PTS screening criteria.

The concern is simply illustrated with the help of Figures 4 and 5, reproduced from Geiß (1987) which seems to be the source of the material presented by Neubrech et al. (1988). Exactly the same, non-conservative, trends were shown also for strains. Note that the positions to which

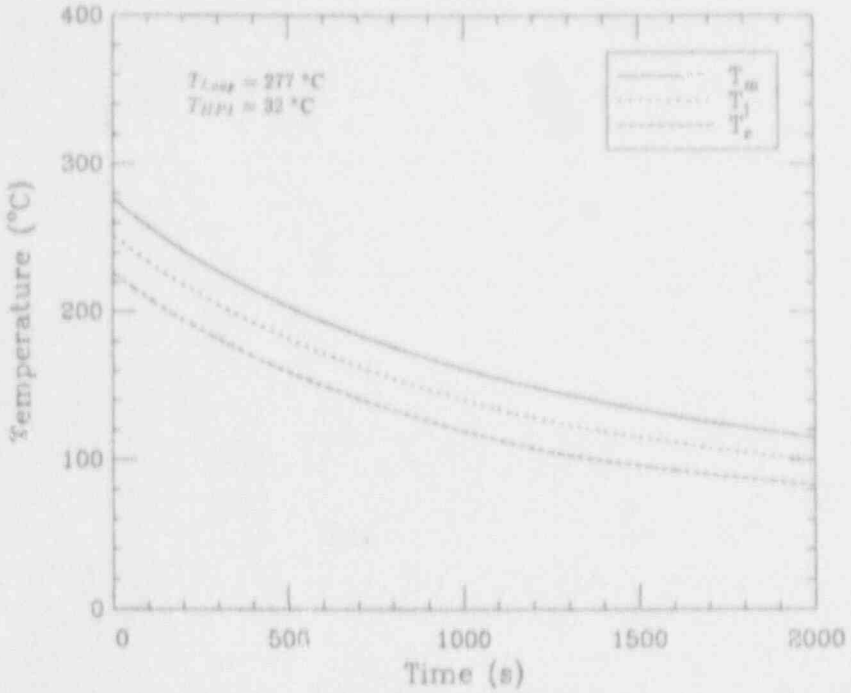


Figure 2. Predicted cooldown transient in Calvert Cliffs for an HPI of 13.5 kg/s in each of the 4 cold legs.

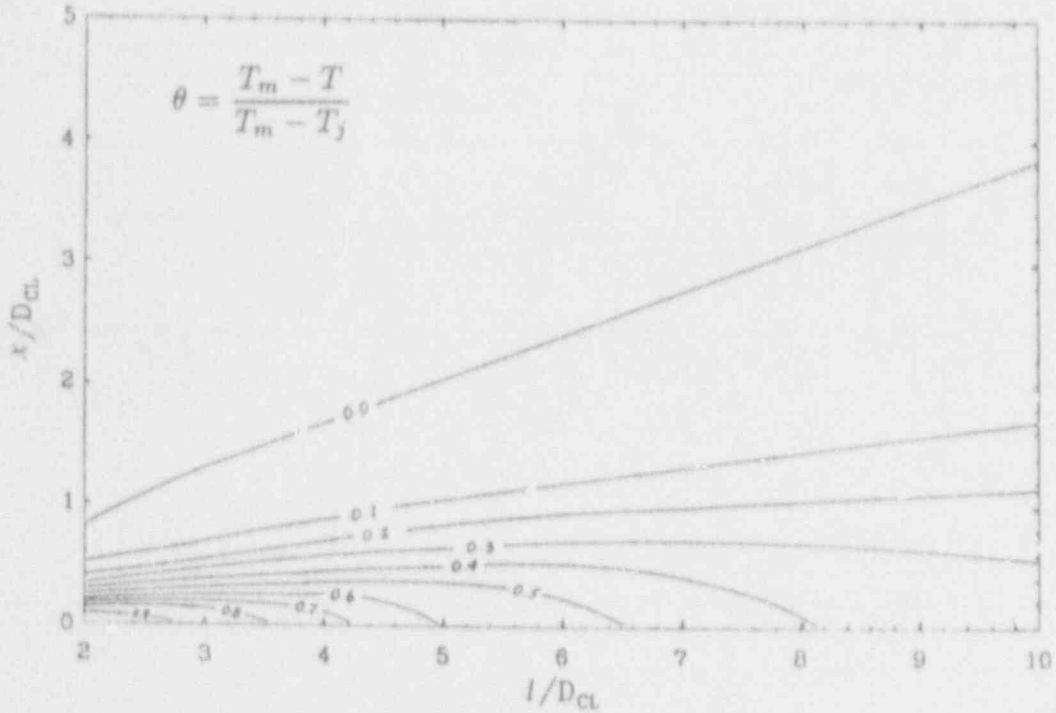


Figure 3. Plume decay (dimensionless) in the downcomer. Actual temperature at any time can be obtained with the help of Figure 2 providing the $T_j$ and $T_m$ values.

Figure 4 refers is 2.6 cold-leg diameters below the cold-leg centerline; that is, the temperature at the plume centerline corresponds closely to $T_j$ and hence the 1D treatment shown should closely correspond to the 1D treatment of the IPTS prescription. At the lower position, Figure 5, the 1D treatment based on the measured local temperature is clearly inadequate; however, it is evidently bounded by the 1D treatment based on $T_j$.

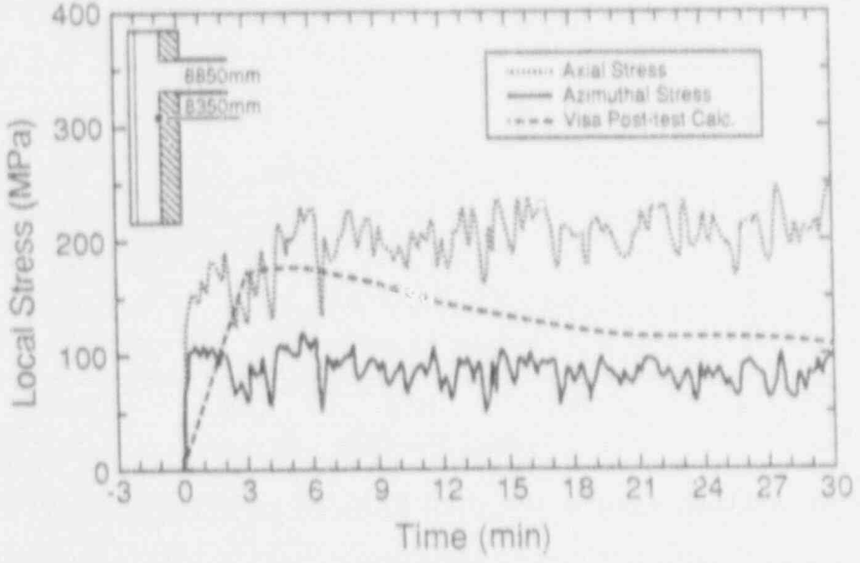


Figure 4. Comparison of calculated stresses in the 1D approximation (VISA) with measured values in HDR test T32.18 (reproduced from Geiß1987). The point shown (measurement) is 2.6 cold-leg diameters below the cold-leg centerline.

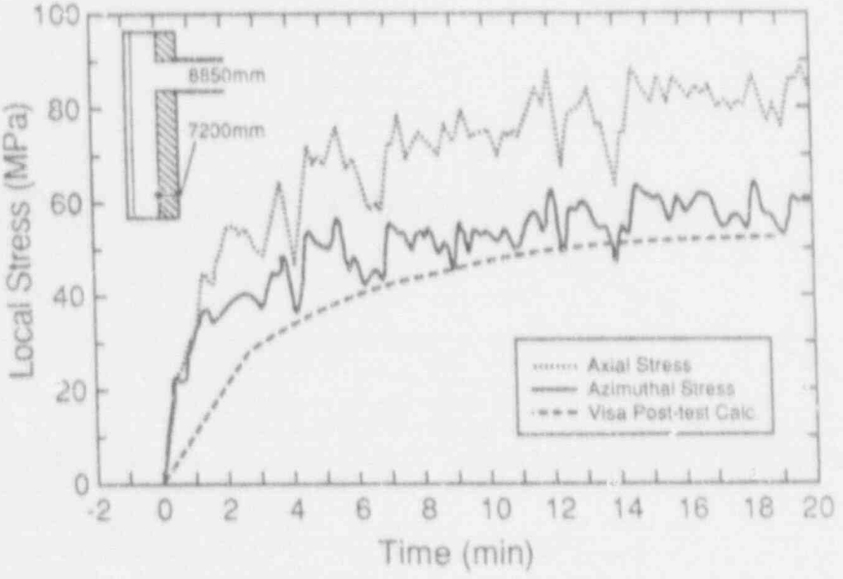


Figure 5. Comparison of calculated stresses in the 1D approximation (VISA) with measured values in HDR test T32.18 (reproduced from Geiß1987). The point shown (measurement) is 7.9 cold-leg diameters below the cold-leg centerline.

This measured, strongly asymmetric, stress field is related to the elongated plume structure and should not have been unexpected. Consider, for example, the thermal stresses in a plane wall assigned a cold, uniform through the wall, elliptical spot. For a temperature difference of $\Delta T$, and major and minor ellipse semiaxis $b$ and $a$ aligned with the $y$ and $x$ coordinates, respectively, we have

$$\sigma_x = -E\left\{\frac{a}{a+b}\right\}\alpha\Delta T \tag{1}$$

$$\sigma_y = -E\frac{b}{a+b}\alpha\Delta T \tag{2}$$

Thus

$$\frac{\sigma_y}{\sigma_x} = \frac{b}{a} \tag{3}$$

and the stress asymmetry increases with the elongation of the ellipse. On the other hand, the through-the-wall temperature gradient, in this example, would be zero, and so the calculated stress in the 1D approximation would also be zero.

The discrepancy in the above example is clearly an exaggeration; it serves to vividly illustrate, however, that the potential concern is legitimate. What remains to be done is to explore quantitatively the impact of this concern on reactor predictions and to examine under what conditions, if any, the 1D treatment is adequate. The reason for this latter aspect is that in the scope of an IPTS study a very large number of wall stress calculations need to be carried out to properly sample the space of uncertainty in the key parameters, and transients, that have to be considered; as a consequence, a full 3D treatment becomes rather impractical. The purpose of this report is to provide some results relevant to these goals. We begin, with section 2, by discussing similarity of stratification and associated fluid thermal transients in the downcomer. We demonstrate that the particular HDR test (T32.18) chosen by Geiß (1987) and Neubrech et al. (1988) suffers from gross dissimilarity to US reactor conditions. We find another HDR test, T32.34, to provide a very close simulation; unfortunately, no stress/strain data have been published for it. REMIX results are found to be in excellent agreement with both of these tests. In section 3 we develop finite element models for 1D and 3D treatments of the RPV and demonstrate that the 3D model accurately depicts the measured stress/strain fields shown in Figures 2 and 3 (for test T32.18). As expected, we find that the 1D treatment, based on $T_j$ as per IPTS study, is non-conservative for a significant fraction of the downcomer area (down to ~7 cold-leg diameters below the cold-leg centerline). By contrast for test T32.34 this area of non-conservative behavior is predicted to shrink down to an axial distance of only 4 cold-leg diameters. The same structural model is applied to the Calvert Cliffs geometry and thermal-hydraulic conditions similar to those of test T32.34. We find that the 1D treatment is even more appropriate than in test T32.34; only an area down to 2 cold-leg diameters is affected (i.e., the axial stress being greater than that computed in the 1D IPTS approximation); that is, the 1D treatment is entirely adequate. Finally, in section 4 we generalize these structural analysis results to four simple, generalized similarity maps that define the regions of potential difficulty with the 1D IPTS prescription. These maps show rather clearly that *all* HDR tests are far from applicable to simulate the thermal stress field in a reactor vessel wall, because they have failed (single loop injection) to represent the global cooldown.

## 2. THERMAL TRANSIENTS AND SIMILARITY CONSIDERATIONS

A scaled representation of the HDR in comparison to the world PTS facilities is shown in Figure 6. The particular geometric data and those relevant to a large US PWR are shown in Tables 1 and 2, respectively. The complete experimental matrix on thermal mixing (TEMB) is summarized in Table 3. These data represent a cornerstone of the total available data base because they uniquely combine full-scale (prototypic) pressure/temperature conditions in a large reactor-like geometry. In fact, as seen in Figure 6, with the exception of the relatively smaller cold-leg diameter (19 vs. 76 cm) and downcomer gap (13 vs. 26 cm) dimensions, the *HDR is essentially a full-scale representation* of a PWR. Another unique aspect of these tests is the stress (strain) measurements on the vessel wall.

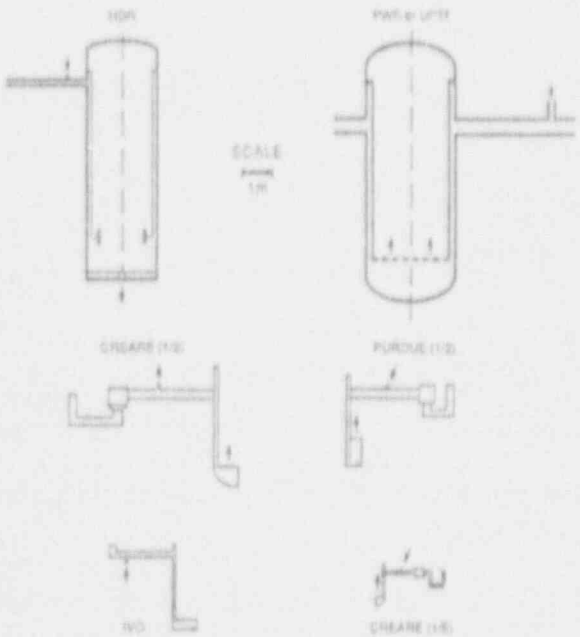

Figure 6. Schematic scaled representation of the HDR in relation to the world integral thermal mixing facilities for PTS.

As already mentioned, the complete TEMB series tests have been very favorably compared with the REMIX predictions; indeed, blind pretest calculations of the first two tests provided excellent predictions of the test data. As we will see in section 3, with accurate thermal boundary conditions the measured stress fields are also easily predictable by a full 3D finite element model. Application of these tools to reactor geometries indicate considerably different trends with regard to the issues mentioned in the introduction. The purpose of this section is to provide the thermal-hydraulic similarity considerations necessary to understand some of the origins of these differences. Structural considerations enter this understanding also; these are developed in section 3.

The stratification behavior has been shown to be universally represented by two dimensionless groups (Theofanous & Yan 1991), namely*

$$Fr_{HPI,CL} = \frac{Q_{HPI}}{A_{CL}} \left\{ g D_{CL} \frac{\Delta\rho}{\rho_{HPI}} \right\}^{-1/2} \quad \text{and} \quad D^* = D_{CL}/D_{HPI} \tag{4}$$

When they are matched (in two different systems with the same $T_m$ and $T_{HPI}$) the difference in cold stream and hot stream temperature is also matched. The actual solution is embodied in the intersection of two plots such as those shown in Figures 7 and 8. Figure 7 represents the entrainment in the HPI plume (MR1 in Figure 1), and it is parametrized by $D^*$, the value of 3.8 being appropriate for the HDR geometry. For a PWR with $D^* = 2.9$ the result is shown

* Note that with these definitions, $Fr_{HPI} = Fr_{HPI,CL} D^{*5/2}$.

Table 1. Geometric data of HDR full-scale test facility.
Injector diameter: 5.0 cm

| | Cold Leg | Vessel/ Downcomer | Lower Plenum | Pump | Loop Seal | Core Barrel | Thermal Shield |
|---|---|---|---|---|---|---|---|
| Inner Diameter (cm) | 18.70 | 296.00 | --- | --- | --- | 266.00 | --- |
| Length (cm) | 600.00 | 694.26 | --- | --- | --- | 694.26 | --- |
| Base Metal Wall Thickness (cm) | 1.52 | 11.20 | 17.10 | --- | --- | 2.30 | --- |
| Clad Thickness (cm) | --- | 0.80 | 0.80 | --- | --- | --- | --- |
| Insulation Thickness (cm) | 10.00 | 10.00 | 10.00 | --- | --- | --- | --- |
| Wall Heat Transfer Area to Water ($cm^2$) x $10^{-4}$ | 3.52 | 64.56 | 23.35 | --- | --- | 58.02 | --- |
| Fluid Volume ($cm^3$) x $10^{-5}$ | 1.65 | 78.47 | 129.80 | --- | --- | --- | --- |

Table 2. Geometric data of a US PWR.+
Injector diameter: 25.7 cm

| | Cold Leg | Vessel/ Downcomer | Lower Plenum | Pump | Loop Seal | Core Barrel | Thermal Shield |
|---|---|---|---|---|---|---|---|
| Inner Diameter (cm) | 76.2 | 436.9 | --- | --- | 76.2 | 375.9 | --- |
| Length (cm) | 623.7 | 685.3 | --- | --- | 456.1 | 685.3 | --- |
| Base Metal Wall Thickness (cm) | 6.35 | 21.9 | 11.1 | --- | 6.35 | 4.45 | --- |
| Clad Thickness (cm) | 0.318 | 0.794 | 0.794 | --- | 0.318 | --- | --- |
| Insulation Thickness (cm) | 0.30 | 0.30 | 0.30 | --- | 0.30 | --- | --- |
| Wall Heat Transfer[a] Area to Water [($cm^2$) x $10^{-5}$] | 1.49 | 2.35 | 0.745 | 0 | 1.09 | 2.02 | --- |
| Internal structures: Heat Transfer Area [($cm^2$) x $10^{-5}$] | --- | --- | --- | 3.08[b] | --- | --- | --- |
| thickness (cm) | --- | --- | --- | 6.35 | --- | --- | --- |
| Fluid Volume [($cm^3$) x $10^{-6}$] | 2.84 | 5.76 | 5.46 | 3.17 | 2.08 | --- | --- |

[a] Per cold leg.
[b] Pump casing and internal structures have been lumped to 33,700 lb equivalent of stainless steel
+ Calvert Cliffs Unit 1

Table 3. Test conditions of HDR full-scale experiments

| Test # | HPI nozzle # | $T_{loop}$ (°C) | $T_{HPI}$ (°C) | $\dot{m}_{HPI}$ (kg/s) | $Fr_{HPI}$ |
|---|---|---|---|---|---|
| T32.11 | 1 | 300 | 20 | 0.12 | 0.1 |
| T32.12 | | 300 | 20 | 0.24 | 0.3 |
| T32.13 | | 300 | 20 | 0.37 | 0.5 |
| T32.14 | | 300 | 20 | 0.49 | 0.6 |
| T32.15 | | 300 | 20 | 0.99 | 1.3 |
| T32.18 | | 300 | 20 | 1.49 | 2.0 |
| T32.19 | | 300 | 20 | 2.37 | 3.2 |
| T32.20 | | 150 | 20 | 2.30 | 5.9 |
| T32.21 | | 300 | 20 | 5.56 | 7.4 |
| T32.22 | | 300 | 20 | 2.37 | 3.2 |
| T32.31 | 2 | 300 | 20 | 0.12 | 0.1 |
| T32.32 | | 300 | 20 | 0.24 | 0.3 |
| T32.33 | | 300 | 20 | 0.37 | 0.5 |
| T32.34 | | 300 | 20 | 0.49 | 0.6 |
| T32.36 | | 300 | 20 | 0.99 | 1.3 |
| T32.41 | | 300 | 20 | 1.48 | 2.0 |
| T32.51 | 3 | 300 | 20 | 0.49 | 0.6 |
| T32.52 | | 300 | 20 | 0.99 | 1.3 |
| T32.57 | | 300 | 20 | 1.48 | 2.0 |
| T32.58 | | 225 | 20 | 0.74 | 1.3 |
| T32.61 | | 150 | 20 | 0.52 | 1.3 |

in Figure 9 (similar plots for $D^*$ values in the range $2 < D^* < 10$ can be found elsewhere, Theofanous & Yan 1991). Figure 8 represents the counter-current flow requirement at the cold-leg downcomer junction expressed by

$$Fr_c^2 + Fr_h^2 = 1 \tag{5}$$

This figure is parametrized by $\rho^* = \rho_h/\rho_c$ and $\beta$. For reactor (and HDR) conditions $0.8 < \rho^* < 1$, and the results vary insignificantly in this range. The parameter $\beta$ expresses whether the system geometry allows back-flow of the cold stream, towards the pump and loop seal volumes. When back-flow is possible and the pump and loop seal volumes represent a significant fraction of the total volume of the system, the $\beta = 1/2$ is appropriate. When such back-flow is not allowed, we set $\beta = 1$, and the result is shown in Figure 10. Returning now to the solution, the intersection (choose the one with the lower value) at the same value of $Fr_{HPI,CL}$, yields the dimensionless entrainment rate, in the plume region, i.e., $Q^* = Q_c/Q_{HPI}$. From $Q^*$ the cold stream temperature, $T_c$, and the downcomer plume "source" temperature, $T_j$, can be simply obtained from

$$T_c \simeq \frac{\rho_{HPI} T_{HPI} + \rho_m T_m Q^*}{\rho_{HPI} + \rho_m Q^*} \tag{6}$$

$$T_j \simeq \frac{1}{2}(T_c + T_m) \tag{7}$$

Applying this procedure to HDR test T32.18 ($Q_{HPI} = 1.49$ kg/s, $T_{HPI}$ =20 °C) we find $Fr_{HPI,CL} = 0.07$ and from Figures 7 and 8 we read $Q^* = 1.1$. With $T_m \sim T_m(0) = 300$ °C, i.e., early in the transient, we thus obtain $T_c = 143$ °C and $T_j = 221$ °C; that is $T_m - T_j = 79$ °C. Using an IPTS plant (Calvert Cliffs as an example with $Q_{HPI} = 13.5$ kg/s, $T_{HPI} = 32$ °C) on the other hand we obtain $Fr_{HPI,CL} = 0.022$ and $Q^* = 3.8$ ($\beta = 1/2$, Figures 8 and 9). For

$T_m \sim T_m(0) = 277$ °C, this translates to $T_c = 214$ °C and $T_j = 245$ °C; that is $T_m - T_j = 32$ °C. Even for $Q_{HPI} = 20$ kg/s, the $Q^*$ decreases to 2.4, which yields $T_c = 190$ °C, $T_j = 234$ °C and $T_m - T_j = 43$ °C. A major discrepancy on the severity of stratification between the plant and the HDR "simulation" is evident. In fact, a much better simulation is provided by another HDR test, the T32.34 ($Q_{HPI} = 0.49$ kg/s, $T_m \sim T_m(0) = 308$ °C, $T_{HPI} = 20$ °C). From Figures 7 and 8 we read $Q^* = 2.5$, which yield $T_c = 203$ °C and $T_j = 256$ °C; that is $T_m - T_j = 52$ °C. Incidentally, ignoring the back-flow in the Calvert Cliffs calculation ($\beta = 1$) would yield (for $Q_{HPI} = 13.5$ kg/s) $Q^* = 3.5$, $T_c = 210$ °C and $T_j = 244$ °C, i.e., the sensitivity to this parameter is not great.

Turning next to the downcomer plume, its "strength" and hence the degree of departure from symmetric behavior are strongly related to how cold the plume is at its source ($T_j$) in relation to its surroundings (at $T_m$). From Equations (6) and (7) above we have

$$T_m(t) - T_j = \frac{1}{2}\frac{T_m(t) - T_{HPI}}{1 + \tilde{\rho}Q^*}, \qquad \tilde{\rho} = \frac{\rho_m}{\rho_{HPI}} \tag{8}$$

During a cooldown transient $\tilde{\rho}$ increases slowly from 0.76 to 1 and $Q^*$ decreases very slowly from its initial value to less than 1 (note that the $Q^*$ change is due to the $\tilde{\rho}$ change). In fact, actual computations (with REMIX) indicate that the two variations compensate each other such that the plume "strength" remains nearly a constant fraction of $T_m(t) - T_{HPI}$. Specifically, this factor is 0.27, 0.19, and 0.15 for HDR/T32.18, HDR/T32.34, and the Calvert Cliffs example mentioned above, respectively. The nature of the thermal stress transient, and the role of the plume in inducing significant departures from the approximate 1D treatment, must therefore be understood in terms of the time constant that characterizes the $T_m(t)$ transient itself.

The global cooldown transient, $T_m(t)$, is characterized, primarily by the system volume ($V$) and the injection flow rate ($Q_{HPI}$), combined into a system time constant, $\tau_s$

$$\frac{T_m(t) - T_{HPI}}{T_m(0) - T_{HPI}} \sim e^{-t/\tau_s} \qquad \tau_s = \frac{V}{Q_{HPI}} \tag{9}$$

where $Q_{HPI}$ is the total injection rate in all the loops. The HDR tests involved only one-loop injection; hence, the $\tau_s$ is rather large: $1.4 \times 10^4$ s and $4.3 \times 10^4$ s for T32.18 and T32.34, respectively, as compared to a value for the Calvert Cliffs example of $1.3 \times 10^3$ s for $Q_{HPI} = 13.5$ kg/s and $9.6 \times 10^2$ s for $Q_{HPI} = 20$ kg/s. This means that even test T32.34, which, as discussed above, provides a good simulation of the stratification, badly misses (to simulate) the thermal stress behavior.* Specifically, in HDR we obtain relatively steady plumes in extremely slowly varying surroundings and the measured stresses are essentially all due to these plumes; while in Calvert Cliffs (or similar reactors) we obtain plumes of rapidly (in time) diminishing strength in relatively rapidly varying surroundings, i.e., the plume-induced stresses diminish in comparison to stresses due to the global cooldown — the latter being uniform and hence more in line with a 1D treatment. This suggests that an effective screening for multi-dimensional effects could be made on the basis of the interplay between plume strength and global cooldown; the details are presented in section 4.

---

* This is exacerbated by the considerably thinner HDR wall (12 cm) compared to that of a large PWR (22 cm).

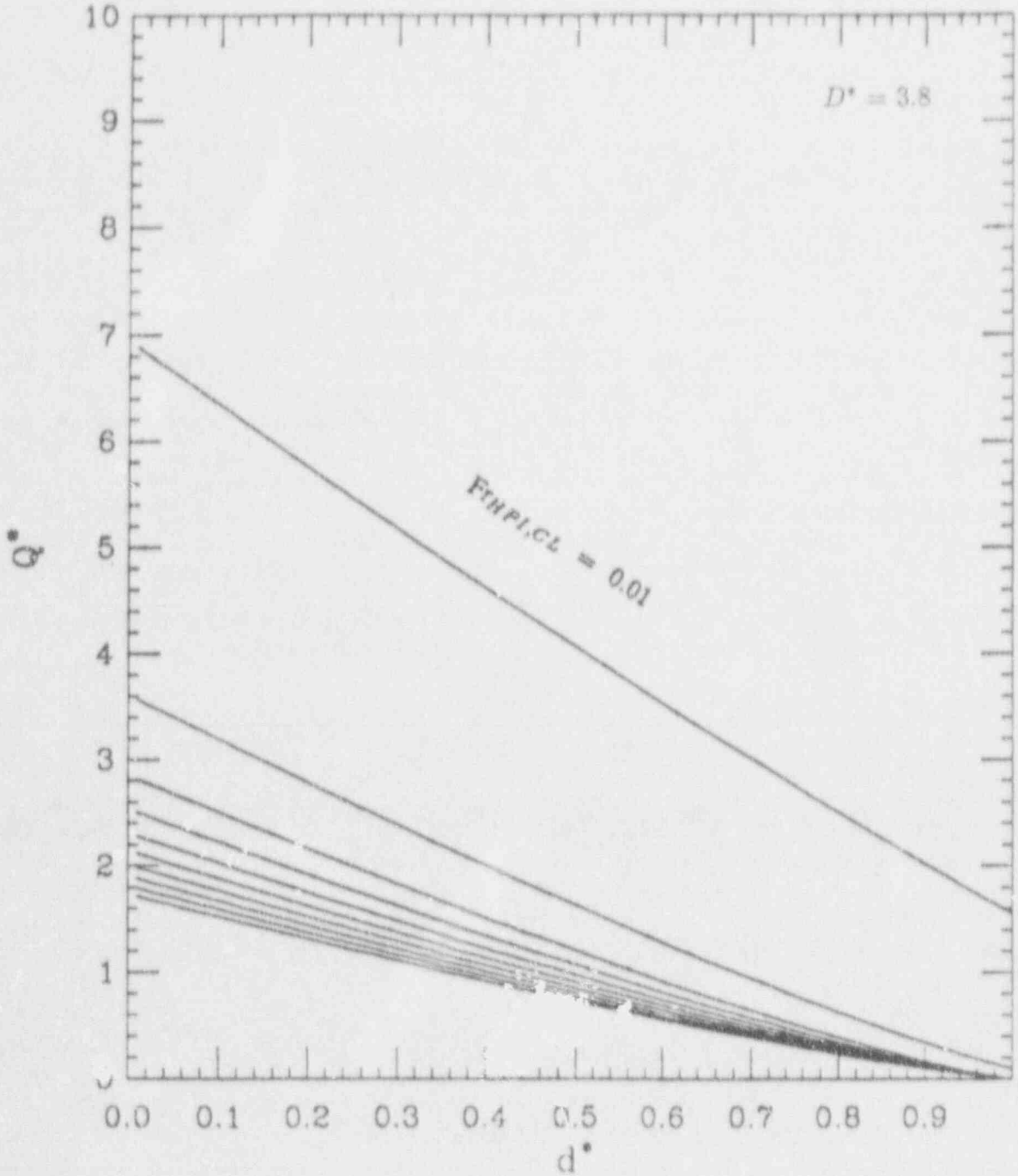


Figure 7. Illustration of plume entrainment for $D^* = 3.8$. $Fr_{HPI,CL}$ is ranging from 0.01 to 0.10 in increments of 0.01.

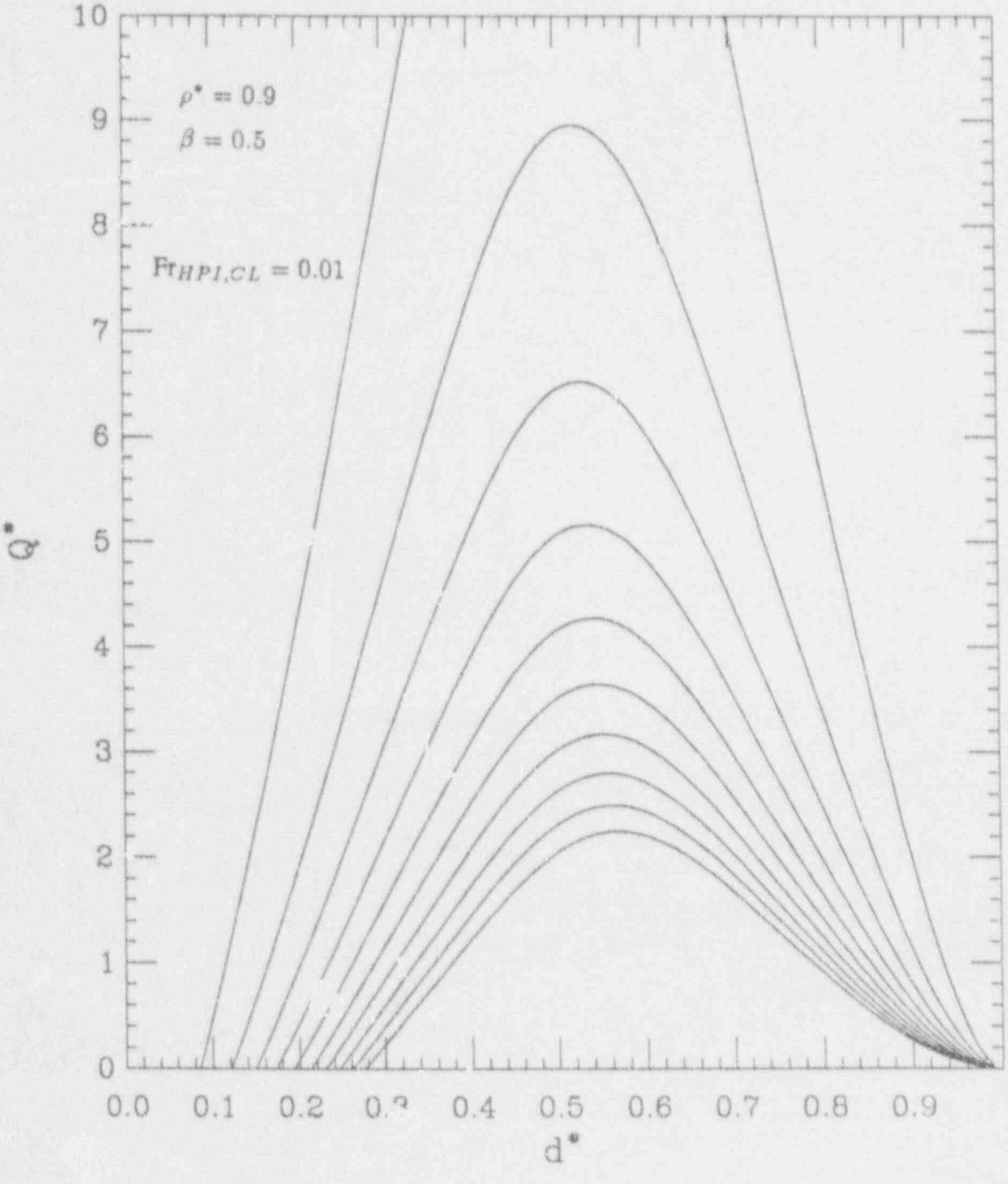


Figure 8. Illustration of counter-current flow-limited entrainment for $\rho^* = 0.9$ and $\beta = 1/2$ $Fr_{HPI,CL}$ is ranging from 0.01 to 0.10 in increments of 0.01.

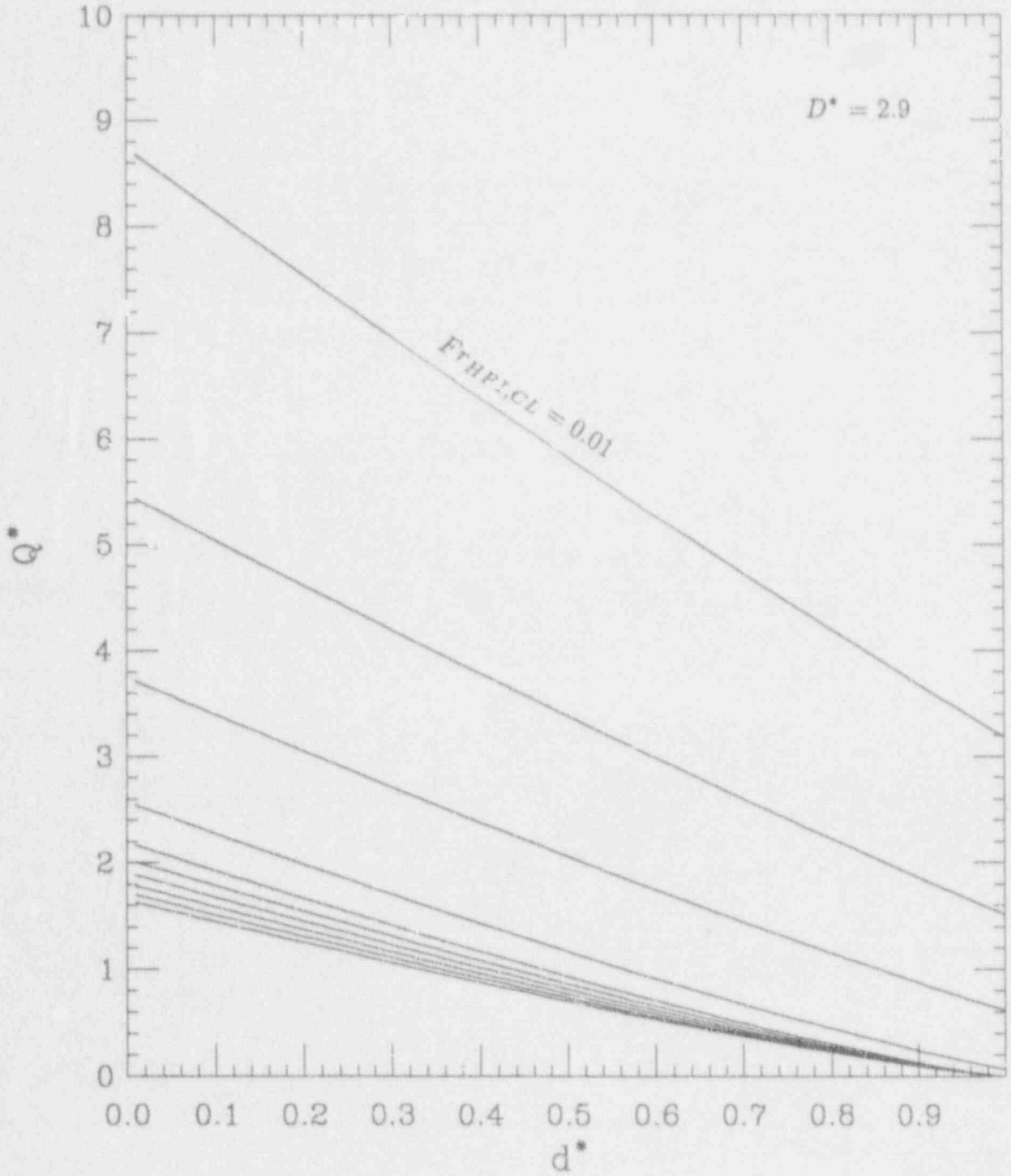


Figure 9. Illustration of plume entrainment for $D^* = 2.9$. $Fr_{HPI,CL}$ is ranging from 0.01 to 0.10 in increments of 0.01.

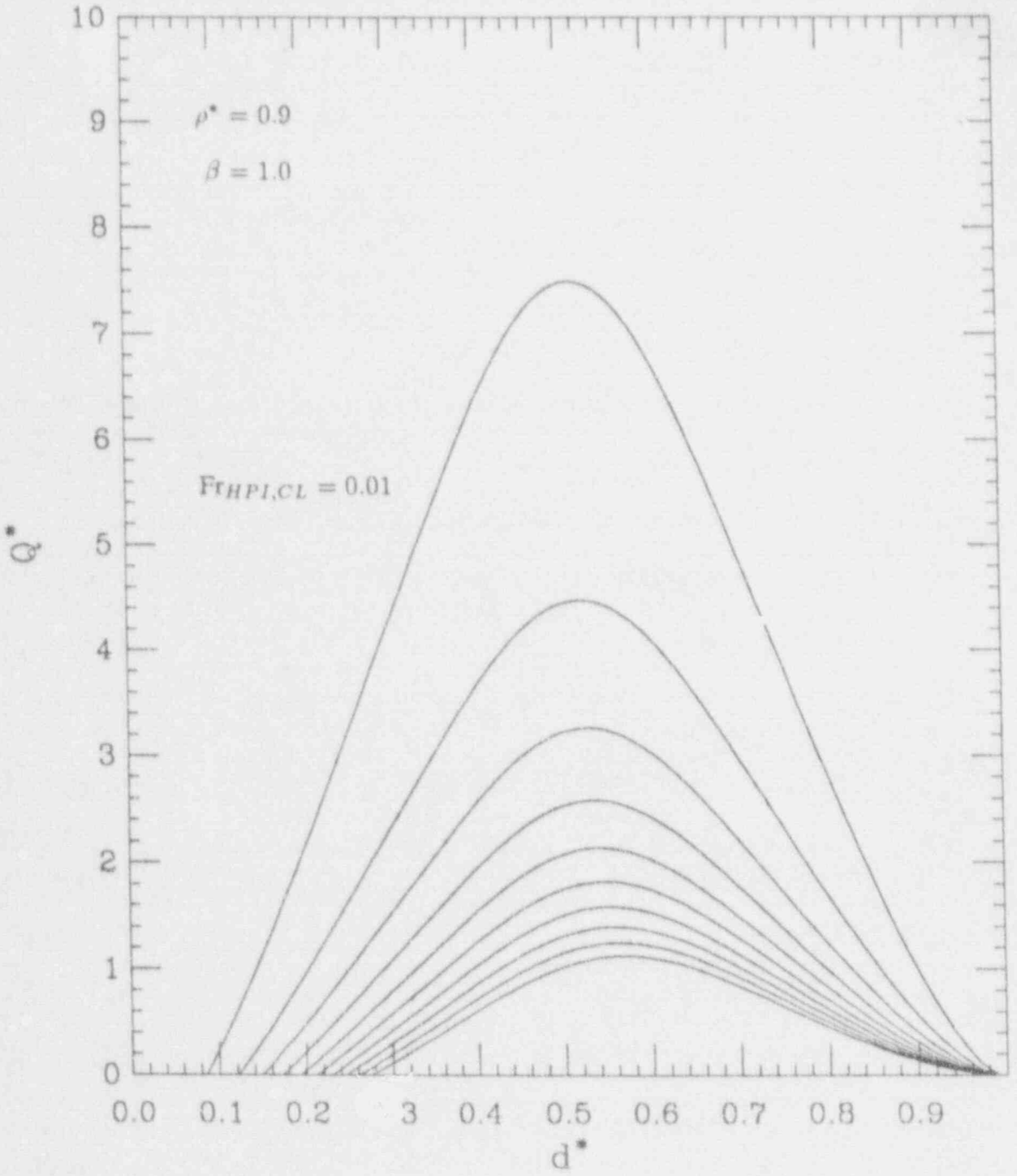


Figure 10. Illustration of counter-current flow-limited entrainment for $\rho^* = 0.9$ and $\beta = 1.0$. $Fr_{HPI,CL}$ is ranging from 0.01 to 0.10 in increments of 0.01.

For the stress analyses of section 3 we also need the shape of the downcomer plumes. From the data, it appears that the HDR plumes are well-behaving (i.e., steady, straight-down descent) and well-characterized (a lot of measuring points); hence, they are ideal for our purposes. Note also that since T32.34 provides a good simulation of stratification in a PWR, the plume behavior in it is also most appropriate. It turns out that when the local plume temperatures are normalized by the plume "strength," $T_m - T_j$, discussed above, even the very severe T32.18 plume takes on a quite similar form. These two experimental plumes are shown in Figures 11 and 12. In terms of stresses, and the discussion in the introduction, we expect that the plume of T32.18 is slightly more severe than that of T32.34, and both are well bounded (in severity) by the plume of Figure 3, used in conjunction with REMIX.

In closing this section, it may be worth remarking that both the stratification and transient cooldown solutions utilized above are in excellent agreement with the more detailed REMIX results, and the quality of comparisons with the HDR experiments T32.18 and T32.34 at the locations of interest (the elevations in Figures 4 and 5) are shown in Figures 13 and 14, respectively.

## 3. THERMAL STRESSES AND SIMILARITY CONSIDERATIONS

The thermal stress computations were carried out with the computer code ABAQUS (Version 4.8) using a three-dimensional finite element model, in a planar geometry, as illustrated in Figure 15. The fine-mesh regions can adequately represent the "hole" corresponding to the cold-leg nozzle as well as the thermal gradients within the plume beneath it. The large-mesh zones were incorporated so as to add an adequate amount of wall material surrounding the plume as is the case for the intended simulation. This plate model was fully encastered in all its four sides. As such, it is applicable to situations where the plume remains in steady surroundings (as in the HDR tests) with minimal restrictions on the duration of the transient. For transients involving also global cooldown, the applicability is restricted to short (conduction) penetration times. In both cases the idea is that thermal stresses in the cooled regions are accurately developed (in the model) as long as there is sufficient material in the initial state ("hot") to resist motion. Under these conditions a plate model free on all its four sides actually yielded the same results. Comparisons with the HDR data (at 7 and 14 minutes) justify this position for the plumes-only case. To judge the effect of global cooldown time (on the model accuracy) we compared the plate model prediction with a cylindrically symmetric full-vessel model, both driven with a sudden change on the inside wall temperature. The results for a reactor vessel wall of 22 cm in thickness are shown in Figure 16, indicating that the plate representation is quite adequate for at least up to 100 s. At this time, the thermal penetration ($\delta \sim 2\sqrt{\alpha t}$) corresponds to 32% of the wall thickness. The full-vessel, cylindrical finite element model is used, below, to compute stresses in the 1D approximation. According to the IPTS procedure, these calculations are based on a global cooldown referred to the $T_j(t)$ transient. Thus, as a matter of nomenclature in the following, 1D results refer to the cylindrical model and 3D results refer to the plate model. Note that the 1D model does not contain the cold-leg "hole." As illustrated in Figure 17, this results in an overprediction of stresses in the immediate vicinity of the "hole."

A first set of results is contained in Figures 18(a), (b) and (c). All these results are for 7-min transients in HDR test T32.18 (18a), test T32.24 (18b), and a hypothetical Calvert Cliffs transient (18c) run in the manner of the HDR tests, i.e., with only 1 nozzle injection and negligible global cooldown in 7 minutes. For the HDR calculations we used the respective experimental plumes (Figures 11 and 12), while for the reactor example we used the plume of Figure 12.

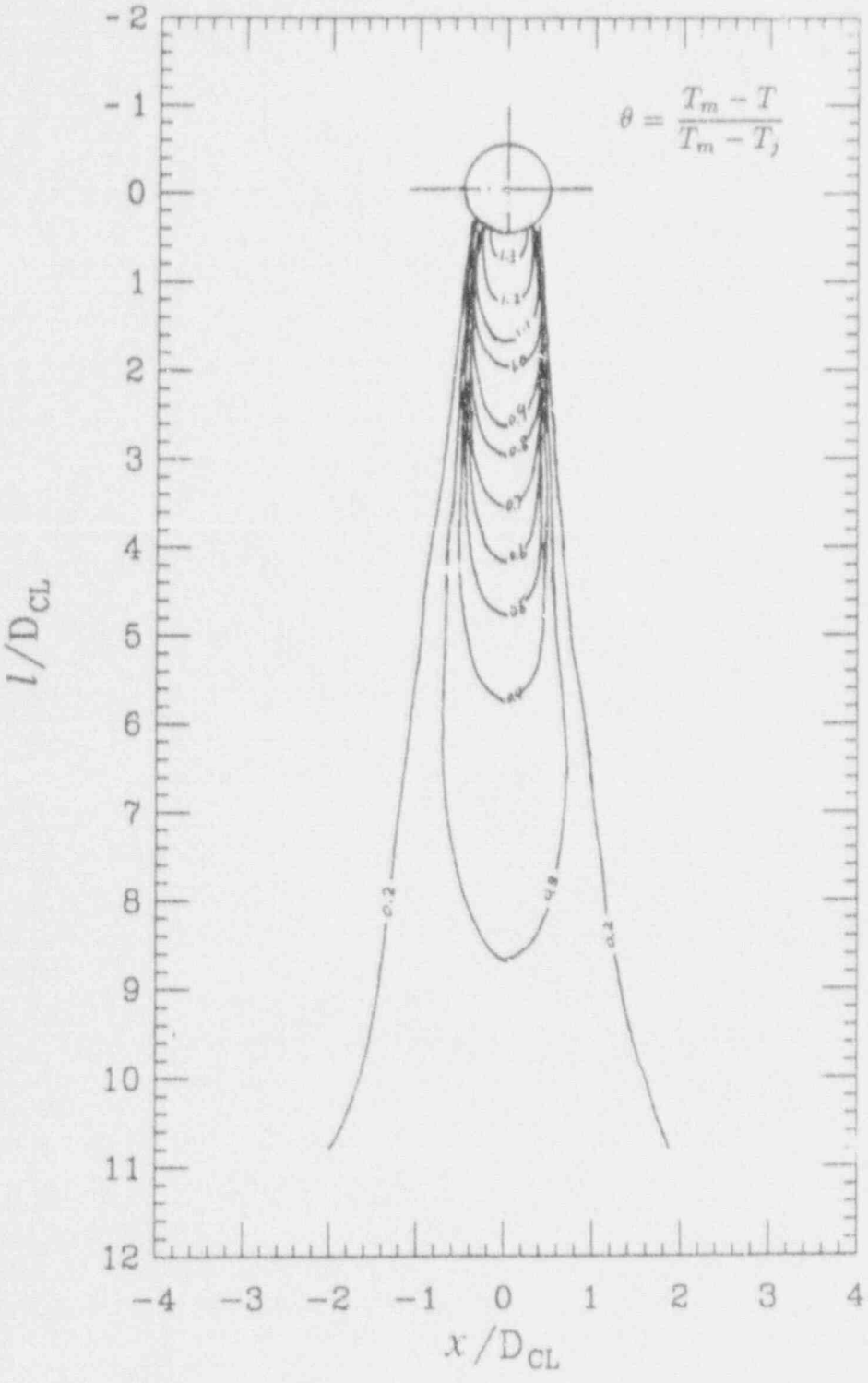


Figure 11. Rough representation of downcomer plume from HDR (test T32.18) data at 420 s.

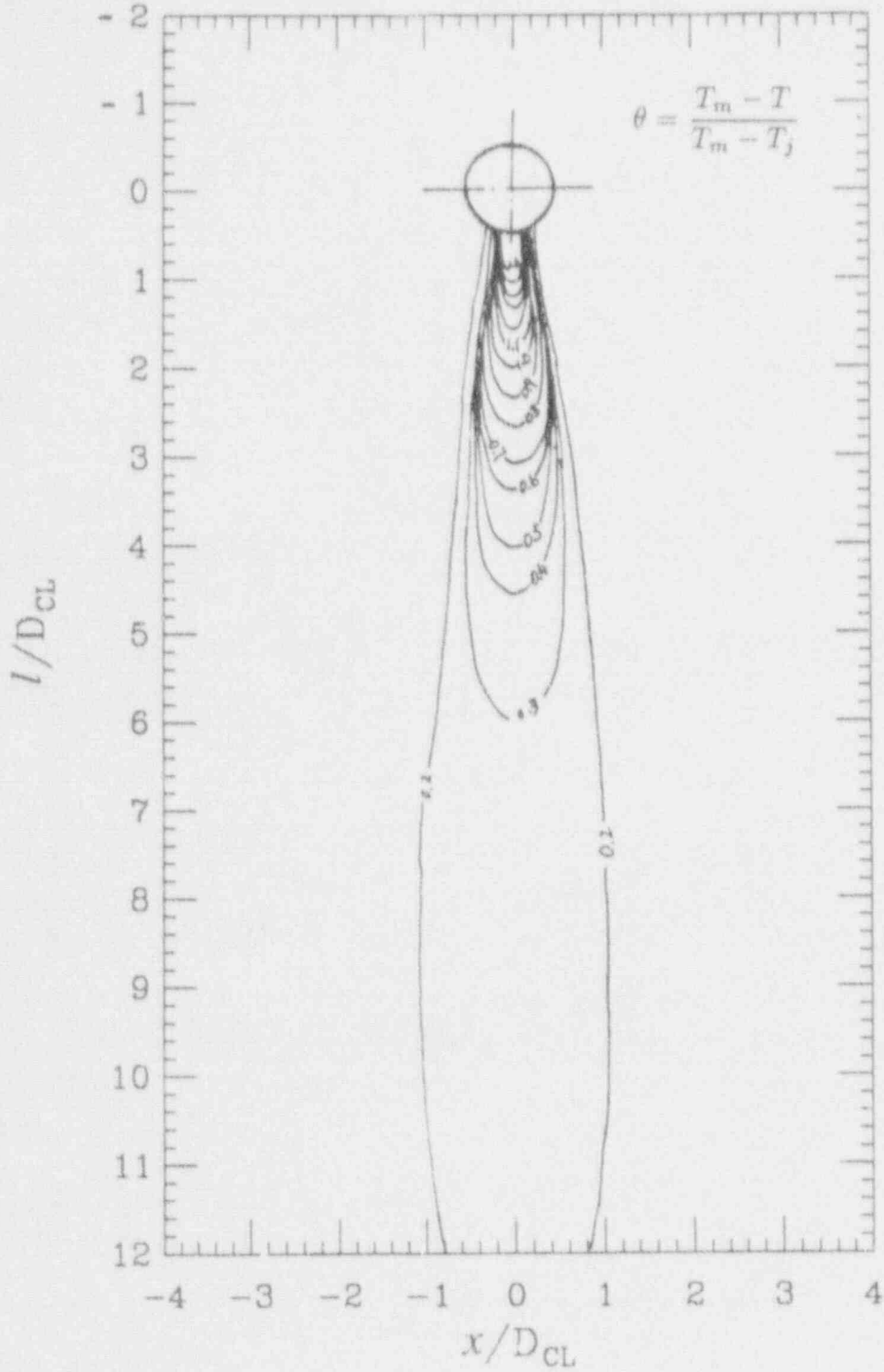


Figure 12. Rough representation of downcomer plume for HDR (test T32.34) data at 420 s.

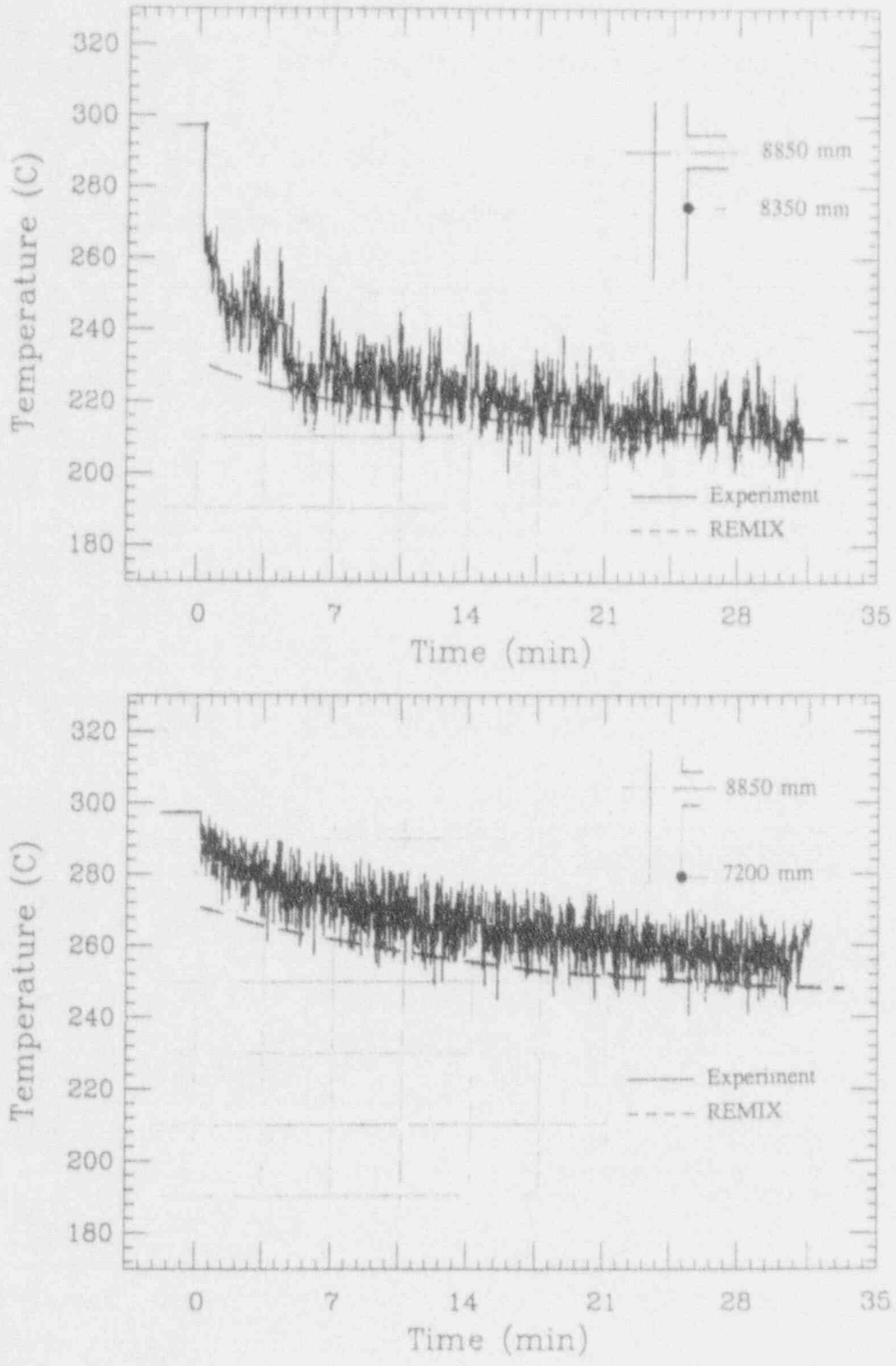


Figure 13. The vessel wall temperature transients measured in HDR (test T32.18) at positions 50 and 165 cm below the cold leg; compared with REMIX predictions.

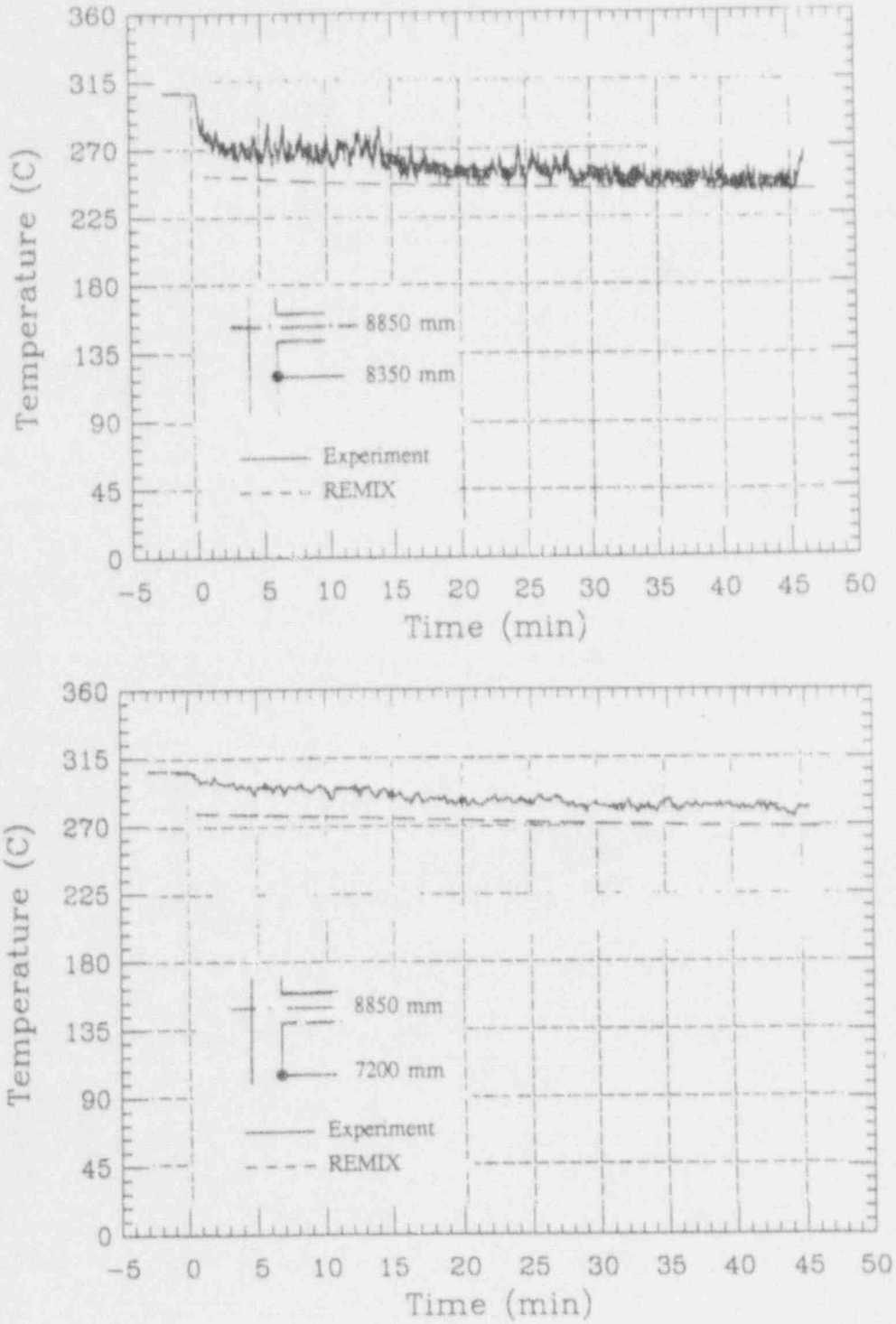


Figure 14. The vessel wall temperature transients measured in HDR (test T32.34) at positions 50 and 165 cm below the cold leg; compared with REMIX predictions.

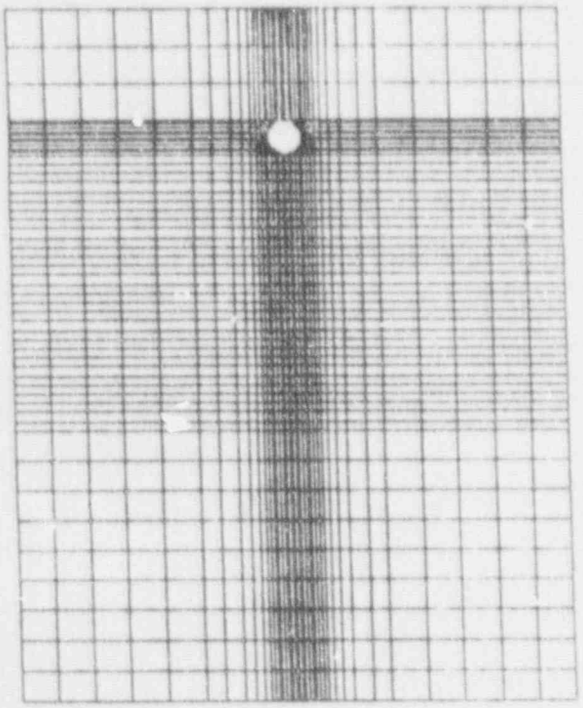

Figure 15. The finite element mesh utilized in the plate (3D) model. There are 7 equal-sized elements along the wall thickness.

The experimental data from T32.18 are shown in Figure 18a, and are found to be in reasonable agreement with the computations. Note that the error in $\sigma_x$ is larger than in $\sigma_y$. This is attributed to the larger uncertainty in the assessed plume widths (in Figure 11) as compared to their lengths. What is clear from Figure 18 is that the area of non-conservative quantification (for brevity we will call it the "area of non-compliance" or ANC), in the 1D approximation depends not only on plume strengths but also on certain additional parameters. We see that due to the increased strength of T32.18 relative to T32.34 the ANC expands from $\sim 4\ell/D$ to $\sim 5.5\ell/D$. On the other hand, for the reactor case it shrinks to $\sim 2.5\ell/D$ even though a plume similar to T32.34 was used. Otherwise, the distributions are similar and strongly non-uniform, giving the impression that the 1D approximation is truly inappropriate, i.e., either strongly conservative (lower part) or strongly non-conservative (upper part). A global view of the stress pattern for the cases of Figure 18 is given in Figure 19.

One of the interesting features of the experimental data (Figures 4 and 5) is that stresses vary only very slowly with time. This indicates that they are primarily the consequence of plumes — only slight cooldown in the time period covered — and a mechanism similar to that discussed in analytical terms in the introduction. This behavior is also borne out by the finite element results. This is illustrated in Figure 20 depicting both calculations and data at 14 minutes into the transient. As another example in the other time direction, Figure 21 depicts the stress fields at 1 minute into the hypothetical HDR-like transient in Calvert Cliffs. It is interesting that although the stress levels for very early times are higher overall, the ANC remains relatively unchanged.

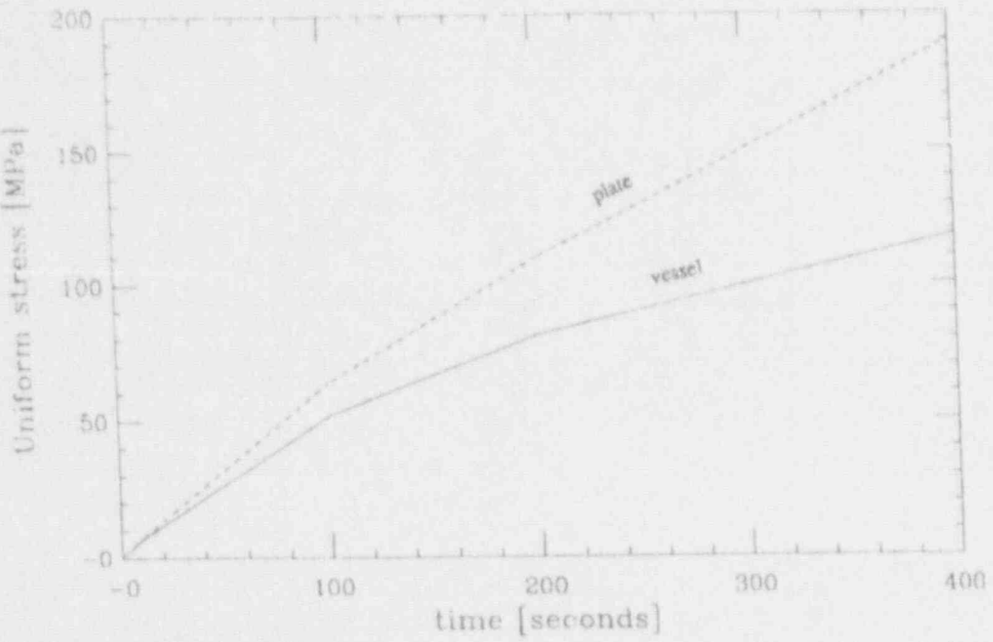


Figure 16. Deviations of the approximate plate model from a cylindrically symmetric full-vessel model as a function of conduction times.

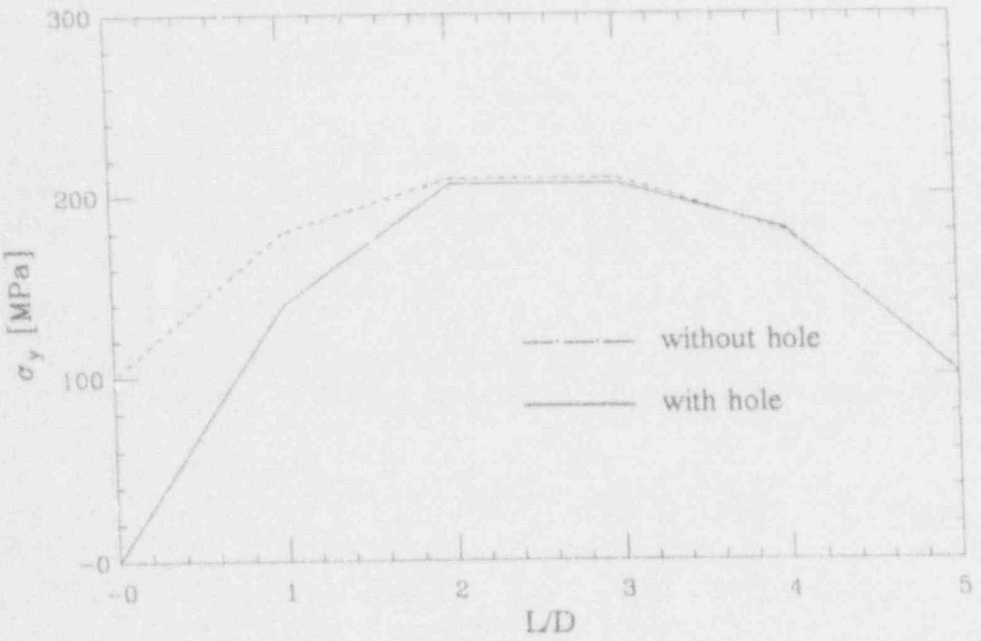


Figure 17. The range of influence of the cold-leg "hole" in the plate model. This sample calculation is for a rectangular plume below the hole of similar size as that in Figure 11, and uniform temperature.

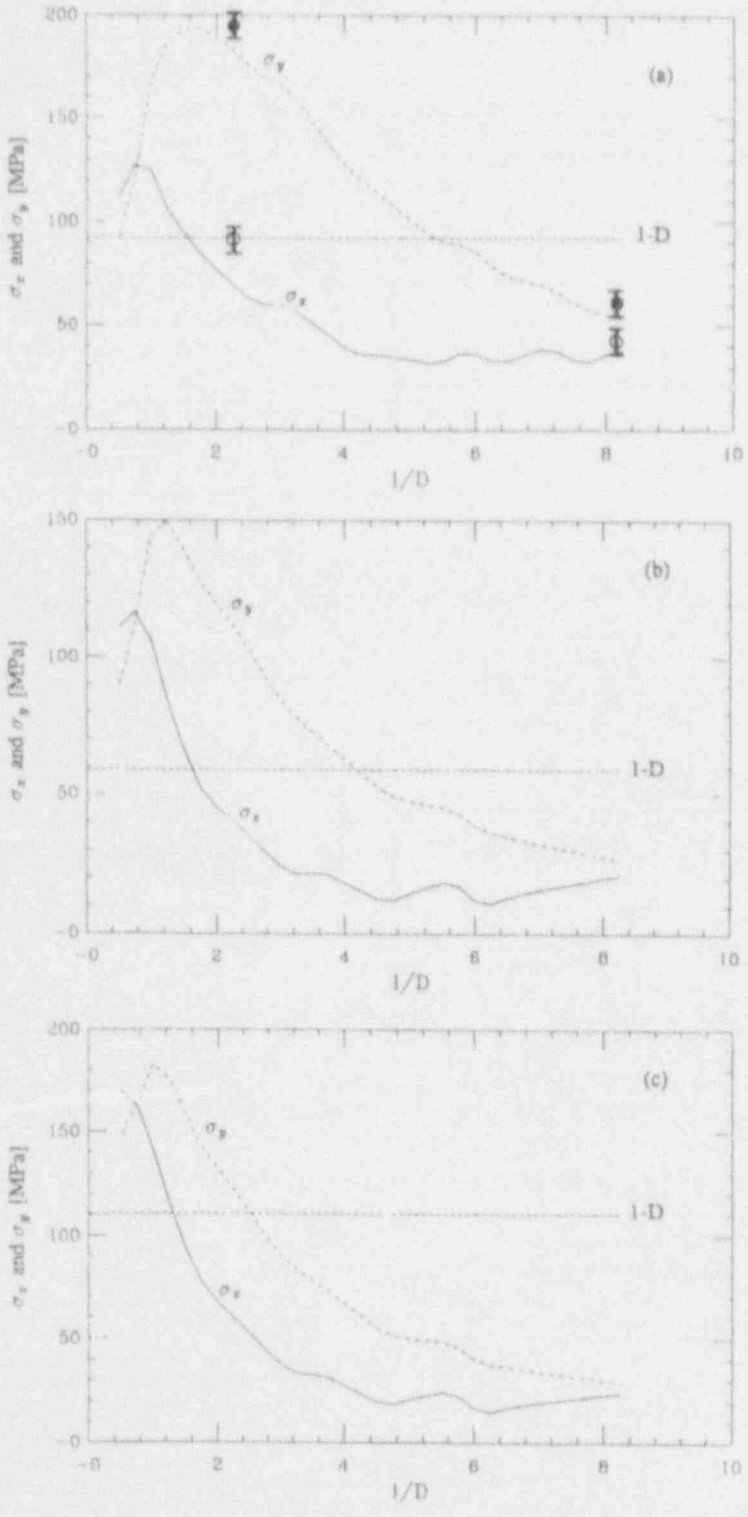


Figure 18. Stress distributions predicted by the plate model compared to the 1D IPTS prescription. (a) HDR test T32.18 at 7 min. (experimental points, $\phi$ $\sigma_y$, $\phi$ $\sigma_x$). (b) HDR test T32.34 at 7 min. (c) Calvert Cliffs geometry with T32.34 conditions (plume, $T_m$, $T_j$) at 7 min.

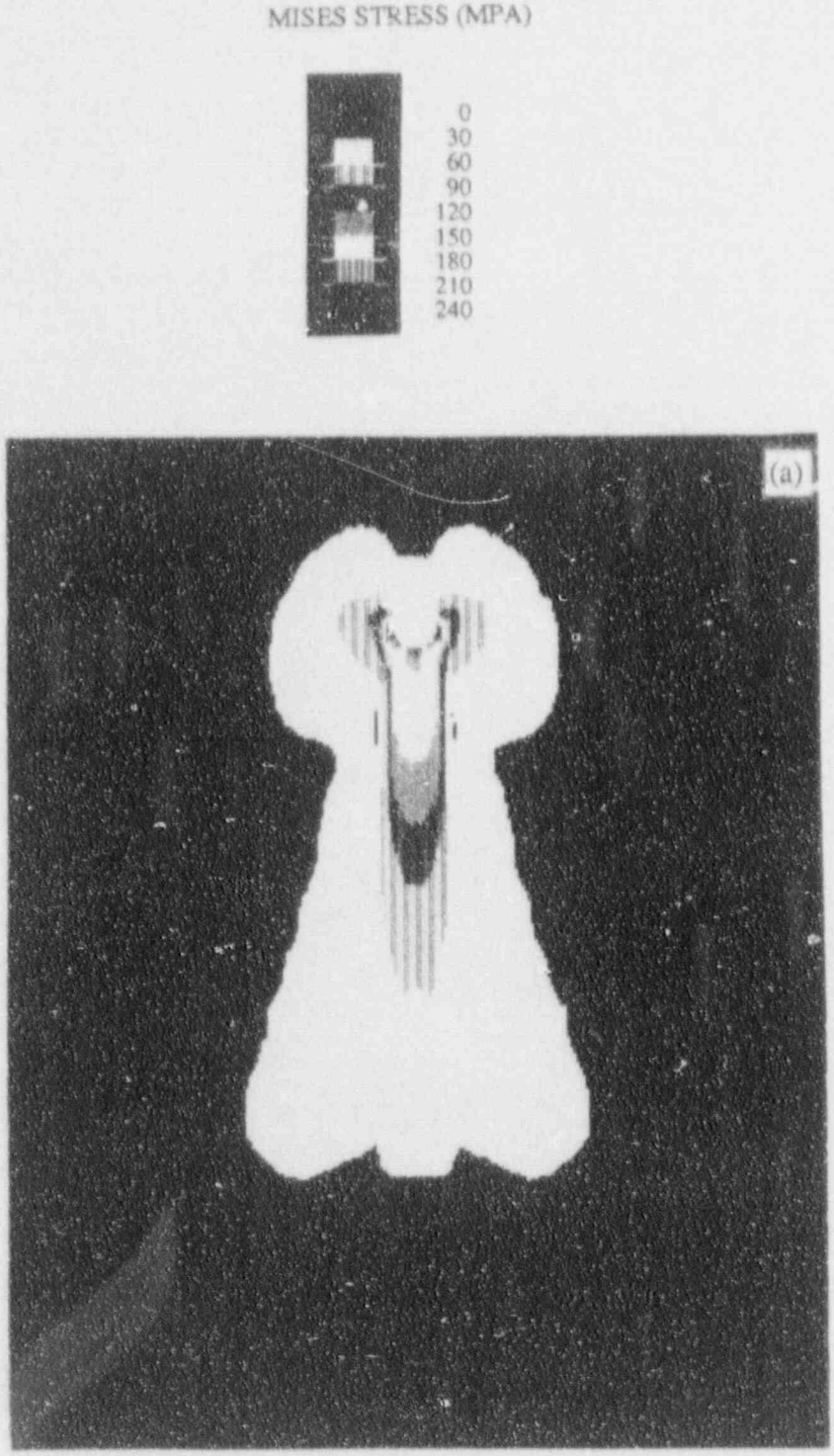


Figure 19. Stress distributions on the inside face of the RPV wall predicted by the plate model cases (a), (b), (c) correspond to those of Figure 18.

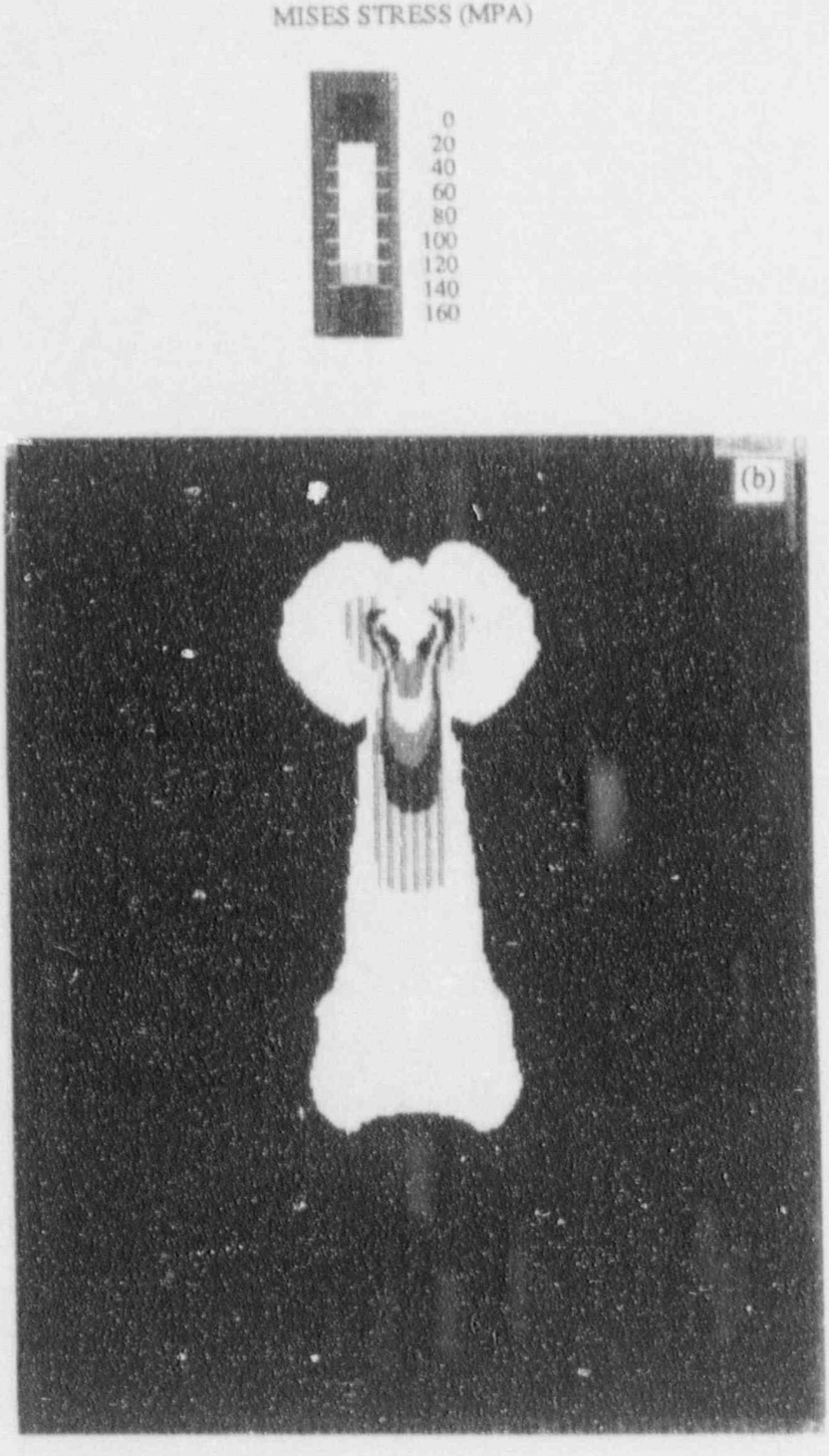


Figure 19. Continued.

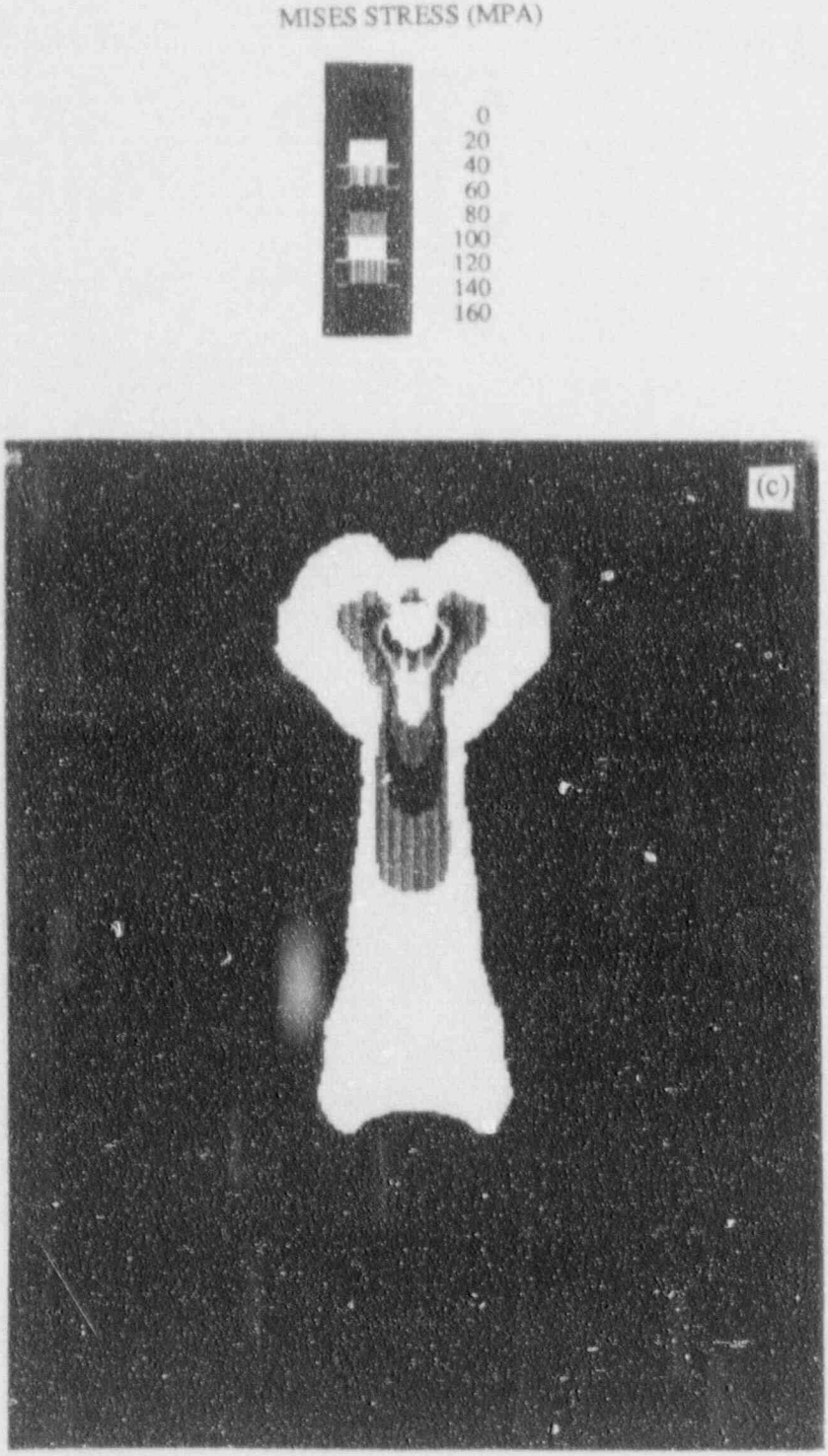


Figure 19. Continued

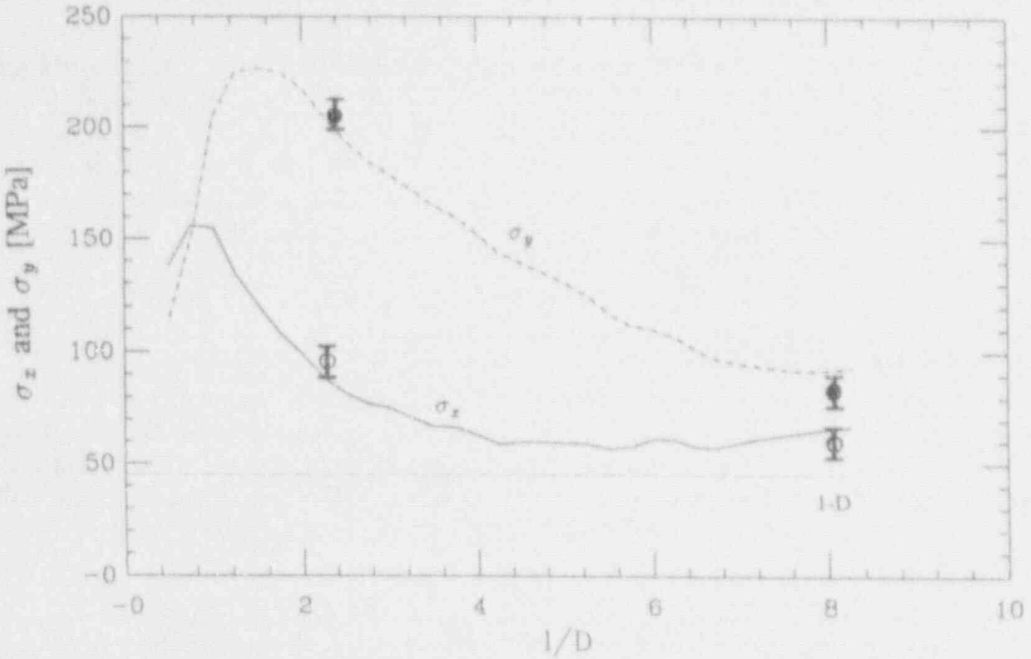


Figure 20. Stress distributions predicted by the plate model compared to the 1D IPTS prescription. HDR test T32.18 at 14 min. (experimental points, $\phi$ $\sigma_y$, $\phi$ $\sigma_z$).

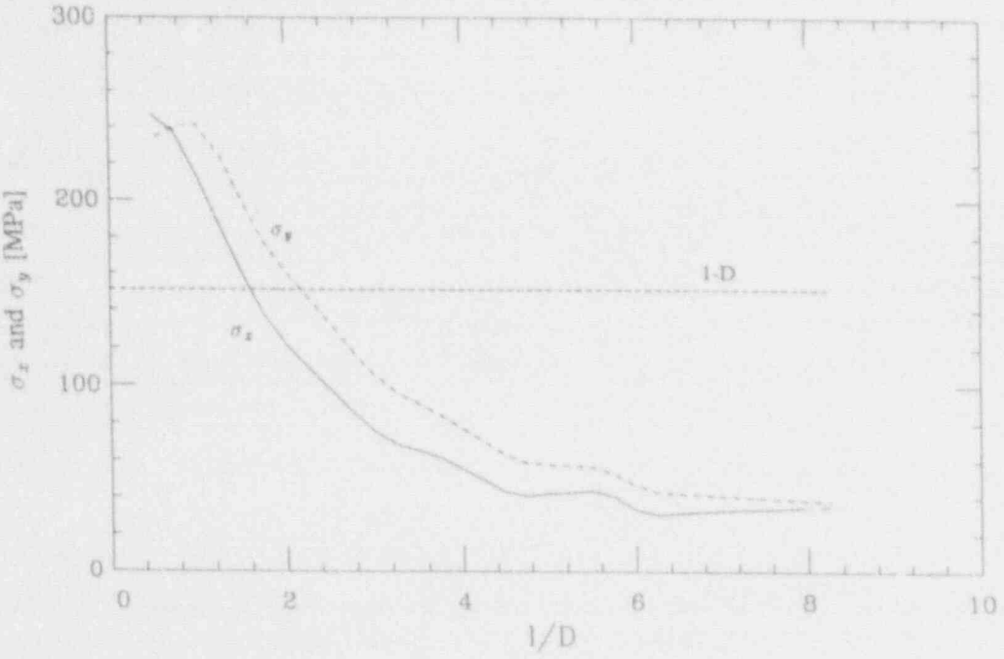


Figure 21. Stress distributions predicted by the plate model compared to the 1D IPTS prescription. Calvert Cliffs geometry with T32.34 conditions (plume, $T_m$, $T_j$) at 1 min.

Finally, to assess the role of global cooldown in combination with the plume stresses a representative reactor case was run, with all four HPI nozzles activated. The cooldown and stratification (from REMIX) are those of Figures 2 and 3. The predicted stress distribution at 60 and 100 seconds are shown in Figures 22 and 23, respectively. Note that the ANC is restricted to less than $\sim 2.5\ell/D$ and the real (3D) stress levels as they rise with time yield an increasingly more uniform distribution approaching, in the region of PTS interest, the 1D result. As the core mid-height is typically at $\sim 5\ell/D$, the region $0 < \ell/D < 2.5$ is comparatively less irradiated and hence of no interest for fracture analysis.

## 4. GENERALIZATION OF RESULTS

The transient conduction/stress problem is characterized by four length scales, the imposed cooldown time and temperature scales, the structural and thermal properties of the wall material, and the time scale for conduction to be limiting (beyond this time the wall surface temperature is essentially equal to the fluid temperature). In the following we discuss each one of these items (in reverse order) for the purpose of deducing the basic scaling criteria for reactor simulations, be they experimental (as in HDR) or analytical (as in those made in this report).

The time scale, $\tau_c$, for the onset of the conduction-limited regime can be estimated from

$$\tau_c \sim 10\frac{k\rho c_p}{h^2} \tag{10}$$

The heat transfer coefficients in the upper and middle plume regions (these are the regions of higher stresses as seen above) are quite high (Iyer & Theofanous 1991a), with typical values around 5000 W/m$^2$ K; thus the $\tau_c$ is of the order of only 70 s. The role of this extremely short, initial portion of the transient is to moderate the thermal stresses in the wall, and this role is strongly interactive with that of the cladding (both in structural material and thermal resistance). Focusing on the main theme of this report, we will ignore this role—this is conservative.

The structural and thermal properties of the wall material in HDR are typical of reactor pressure vessels, and there is no need to be included in this scaling analysis. In the analytical simulations we will take them to be fixed at the nominal values utilized for the HDR test comparisons above.

The imposed temperature scale is defined by the initial system temperature, $T_m(0)$, and the "cold" safety injection temperature, $T_{HPI}$; that is, $T_m(0) - T_{HPI}$. From Equation (9) this overall temperature scale translates to the instantaneous temperature scale, through the system cooldown time constant, $\tau_s$, i.e.,

$$T_m(t) - T_{HPI} = (T_m(0) - T_{HPI})e^{-t/\tau_s} \qquad \tau_s = \frac{V}{Q_{HPI}} \tag{11}$$

or

$$T_m(0) - T_m(t) = (T_m(0) - T_{HPI})(1 - e^{-t/\tau_s}) \tag{12}$$

With reference to Figure 24, this instantaneous temperature scale is seen to control the thermal gradients in the wall material outside the plume. The instantaneous temperature scale within the plume, $T_m(0) - T_j$, can be derived in a similar way from Equation (8),

$$T_m(t) - T_j(t) = \frac{1}{2}\frac{T_m(t) - T_{HPI}}{1 + \tilde{\rho}Q^*} \qquad \tilde{\rho} = \frac{\rho_m}{\rho_{HPI}} \tag{13}$$

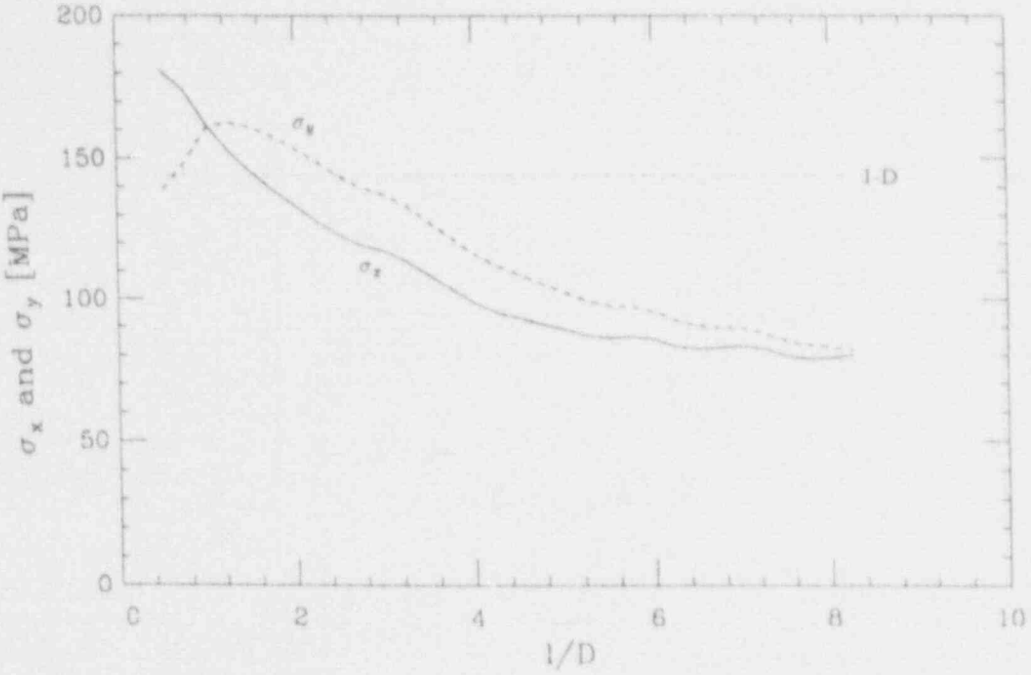


Figure 22. Stress distribution at 60 s for a full (4-nozzle injection) Calvert Cliffs simulation: $Q_{HPI} = 13.5$ kg/s per nozzle, $T_{HPI} = 32$ °C, and $T_m(0) = 277$ °C.

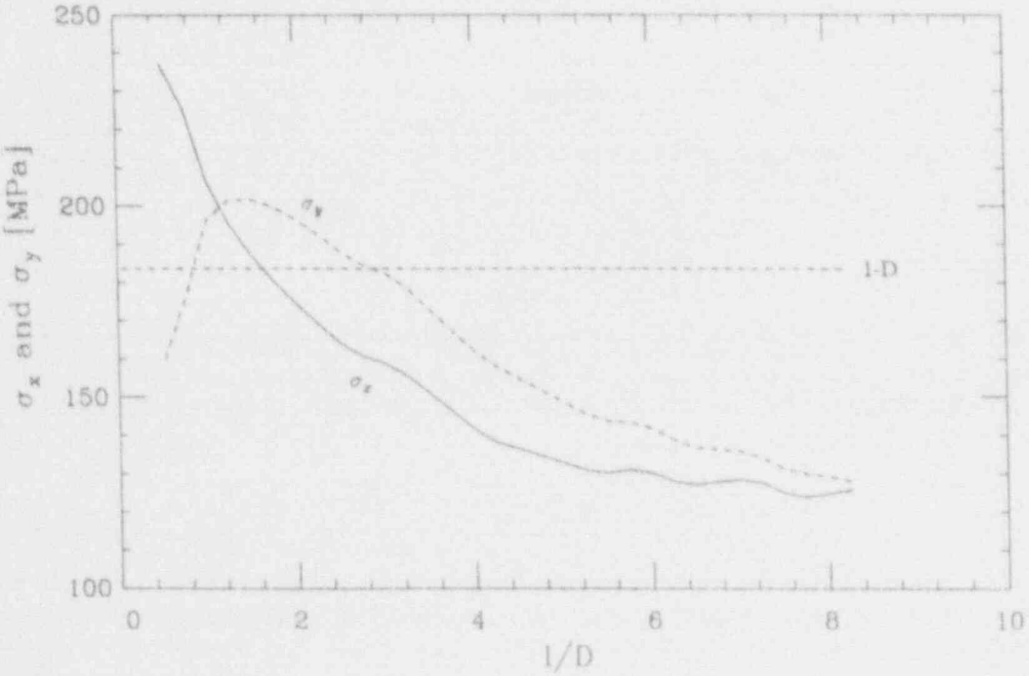


Figure 23. Stress distribution at 100 s for a full (4-nozzle injection) Calvert Cliffs simulation: $Q_{HPI} = 13.5$ kg/s per nozzle, $T_{HPI} = 32$ °C, and $T_m(0) = 277$ °C.

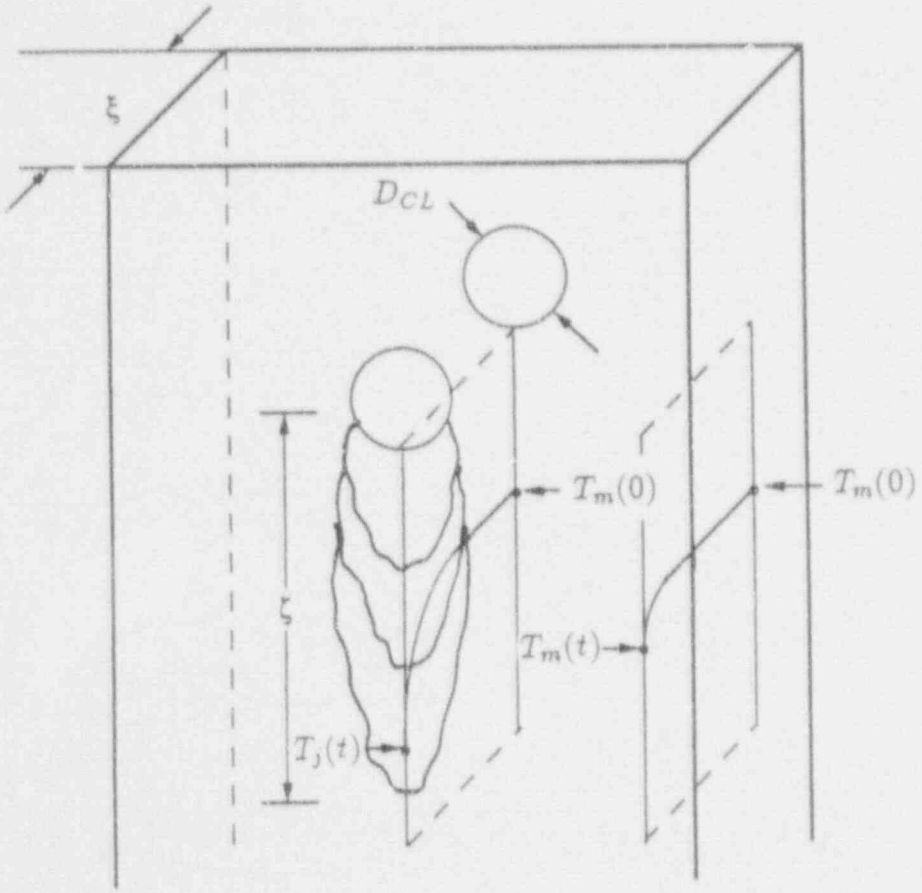


Figure 24. Illustration of thermal gradients and related length scales.

and in combination with Equations (11) and (12) we have

$$T_m(0) - T_j(t) = (T_m(0) - T_{HPI}) \left\{ (1 - e^{-t/\tau_s})^{-1} e^{-t/\tau_s} + 2(1 + \tilde{\rho} Q^*) \right\} \frac{1 - e^{-t/\tau_s}}{2(1 + \tilde{\rho} Q^*)} \quad (14)$$

Again, as seen in Figure 24, this controls the temperature gradients inside the plume region. Now, besides the system time constant, $\tau_s$, we also have the normalized entrainment rate, $Q^*$, and the density ratio, $\tilde{\rho}$. But already we know that $Q^*$ scales with the Froude number and the injection-to-cold-leg diameter ratio, i.e.,

$$Q^* = Q^*(Fr_{HPI,CL}, D^*) \quad (15)$$

while for the same initial and safety injection temperatures the $\tilde{\rho}$ transient will also scale with the system time constant, $\tau_s$. Moreover, as we have seen, the two-dimensional plume structure can be represented by

$$\theta = \frac{T_m(t) - T(t)}{T_m(t) - T_j(t)} = f(x/D_{CL}, \ell/D_{CL}; Q^*) \quad (16)$$

where the $Q^*$ dependency is weak. Thus we conclude that all internal-instantaneous temperature scales (i.e., those that control the stress-generating gradients) are scaled, on the basis of the overall, imposed, temperature scale, $T_m(0) - T_{HPI}$, through the following dimensionless groups

$$t/\tau_s\,, \qquad Fr_{HPI,CL}\,, \qquad D^* \tag{17}$$

the positional mapping, in the downcomer, being simply on the basis of $x/D_{CL}$ and $\ell/D_{CL}$.

Finally, the four length scales (see Figure 24) can be identified as the vessel wall thickness, $\xi$, the cold leg diameter, $D_{CL}$, some characteristic scale for the plume elongation, $\zeta$, and the thermal penetration length scale $\sim\sqrt{\alpha t}$. They yield three dimensionless groups:

$$\xi/D_{CL}, \qquad \zeta/D_{CL} \quad \text{and} \quad \xi/\sqrt{\alpha t} \tag{18}$$

The first of these groups can be considered as fixed, the second is only weakly dependent on the plume strength (i.e., $Fr_{HPI,CL}$ and $D^*$), while the third group plays an essential role in the development of the stress field. It can also be written in terms of the penetration time constant, $\tau_p$, as:

$$\tau_p/t \quad \text{where} \quad \tau_p = \xi^2/\alpha \tag{19}$$

expressing the e: .nt of thermal gradient in the wall at any particular time, $t$, in the cooldown transient.

From the above, for geometric and Froude number similarity, the whole cooldown/stress problem can be scaled with only two parameters; namely, $\tau_p/\tau_s$ and $\tau_p/t$.

Regarding the behavior in relation to the $\tau_p/t$ group, the plate model, valid only for up to $\tau \sim$100 s as already discussed, became rather restrictive. Thus a full-vessel, three-dimensional, finite element model was set up as shown in Figure 25. Benchmarking of this model with the measured stresses in HDR was even better than found for the simpler plate model (Figure 26 vs. Figure 18a). This model was then exercised, in conjunction with REMIX predictions of temperature histories applied as boundary conditions on the inside surface of the vessel, to cover a wide range of the $\tau_p/\tau_s$ and $\tau_p/t$ scaling groups developed above. Starting with the Calvert Cliffs characteristics variations in system volume, and transient time were made to cover the range of potential interest in these scaling groups. A listing of all computational runs made is given in Table 4 and the results are collected in the appendix. All these calculations were run for single plumes as test cases showed that 3 or 4 circumferentially spaced plumes produce essentially the same results.

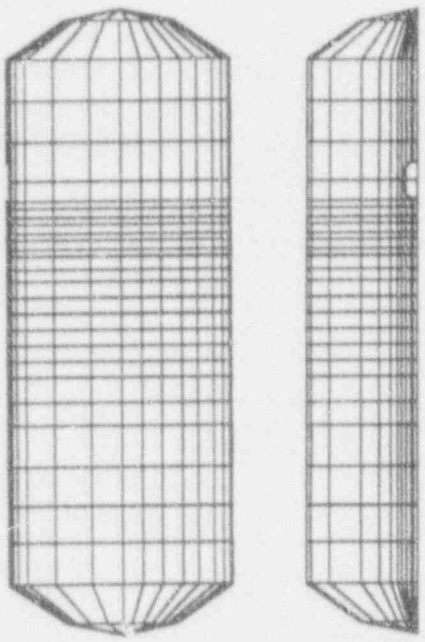

Figure 25. Mesh for full-vessel finite element model.

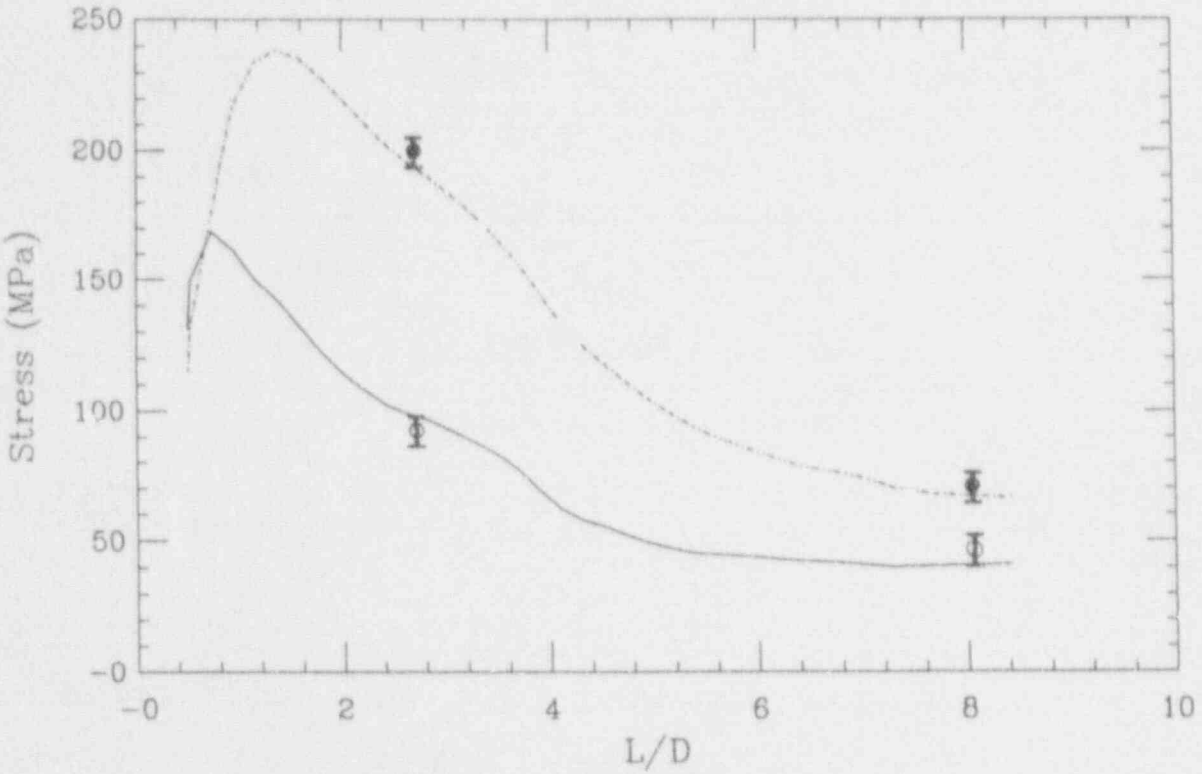


Figure 26. Stress distributions in the HDR wall test T32.18 at t = 7 min. · – · – · – predicted $\sigma_y$, ϕ measured $\sigma_y$, —— predicted $\sigma_z$, ϕ measured $\sigma_z$.

Qualitatively, the results can be distinguished in three classes, as illustrated in Figures 27(a), (b) and (c). Figure 27(a) represents a strongly non-conservative behavior of the 1D approximation. Figure 27(b) shows a strongly conservative one, and Figure 27(c) shows a case where the 3D results are very close to the 1D approximation. Quantitatively, the "figures of merit" in assessing the impact of the 1D approximation can be summarized in terms of four parameters:

(a) ANC: The downcomer length (in $\ell/D$'s) for which the 3D stresses are higher than the 1D

(b) $\Delta_1 = \frac{\sigma_{max} - \sigma_{1D}}{\sigma_{max}} \times 10^2$: A measure of peak discrepancy between the 3D and 1D results

(c) $\Delta_2 = \frac{\sigma_{max} - \sigma(\ell/D=5)}{\sigma_{1D}} \times 10^2$: A measure of the deviation of the 3D result from the flat 1D one, over the upper half of the downcomer

(d) $\Delta_3 = \frac{\sigma_{max} - \sigma(\ell/D=10)}{\sigma_{1D}} \times 10^2$: A measure of the deviation of the 3D results from the flat 1D one, over the whole $10\ell/D$'s of the downcomer

For example, these parameters, for the three comparisons of Figure 26, in the order given above are:

Table 4. List of computational runs

Runs from 2-1 to 2-10 are for Calvert Cliffs reactor.
Others are obtained by varying the system volume only.

| Run # | $\tau_s$ (s) | $\tau_p$ (s) | t (s) | $T_m$ (°C) | $T_j$ (°C) |
|---|---|---|---|---|---|
| 1-1 | 3572 | 5095 | 20 | 275.0 | 220.8 |
| 1-2 | 3572 | 5095 | 60 | 272.4 | 248.0 |
| 1-3 | 3572 | 5095 | 120 | 268.3 | 244.2 |
| 1-4 | 3572 | 5095 | 240 | 260.7 | 237.0 |
| 1-5 | 3572 | 5095 | 420 | 250.0 | 228.0 |
| 1-6 | 3572 | 5095 | 600 | 241.6 | 218.5 |
| 1-7 | 3572 | 5095 | 1200 | 217.5 | 195.0 |
| 1-8 | 3572 | 5095 | 1800 | 199.4 | 177.5 |
| 1-9 | 3572 | 5095 | 2400 | 185.3 | 163.9 |
| 1-10 | 3572 | 5095 | 3000 | 174.0 | 152.6 |
| 2-1 | 1324 | 5095 | 30 | 270.9 | 246.6 |
| 2-2 | 1324 | 5095 | 60 | 265.3 | 241.3 |
| 2-3 | 1324 | 5095 | 120 | 254.9 | 231.2 |
| 2-4 | 1324 | 5095 | 240 | 236.7 | 213.8 |
| 2-5 | 1324 | 5095 | 420 | 214.2 | 191.8 |
| 2-6 | 1324 | 5095 | 600 | 195.7 | 174.0 |
| 2-7 | 1324 | 5095 | 1200 | 152.3 | 131.4 |
| 2-8 | 1324 | 5095 | 1800 | 125.0 | 107.7 |
| 2-9 | 1324 | 5095 | 2400 | 106.7 | 92.5 |
| 2-10 | 1324 | 5095 | 3000 | 94.2 | 81.9 |
| 3-1 | 637 | 5095 | 30 | 265.0 | 241.0 |
| 3-2 | 637 | 5095 | 60 | 255.0 | 231.3 |
| 3-3 | 637 | 5095 | 120 | 238.5 | 215.6 |
| 3-4 | 637 | 5095 | 240 | 213.9 | 191.5 |
| 3-5 | 637 | 5095 | 420 | 188.6 | 167.1 |
| 3-6 | 637 | 5095 | 600 | 171.4 | 150.1 |
| 3-7 | 637 | 5095 | 1200 | 140.2 | 120.4 |
| 3-8 | 637 | 5095 | 1800 | 126.2 | 108.7 |
| 3-9 | 637 | 5095 | 2400 | 119.0 | 102.7 |
| 3-10 | 637 | 5095 | 3000 | 114.9 | 99.3 |
| 4-1 | 12016 | 5095 | 30 | 276.2 | 251.6 |
| 4-2 | 12016 | 5095 | 60 | 275.5 | 215.0 |
| 4-3 | 12016 | 5095 | 120 | 274.2 | 249.7 |
| 4-4 | 12016 | 5095 | 240 | 271.8 | 247.4 |
| 4-5 | 12016 | 5095 | 420 | 268.3 | 244.2 |
| 4-6 | 12016 | 5095 | 600 | 265.0 | 241.1 |
| 4-7 | 12016 | 5095 | 1200 | 255.3 | 231.6 |
| 4-8 | 12016 | 5095 | 1800 | 246.8 | 223.5 |
| 4-9 | 12016 | 5095 | 2400 | 239.3 | 216.3 |
| 4-10 | 12016 | 5095 | 3000 | 232.5 | 209.8 |

For example, these parameters, for the three comparisons of Figure 26, in the order given above are:

Figure 27(a): $\Delta_1 = 50$, $\Delta_2 = 45$, and $\Delta_3 = 57$

Figure 27(b): $\Delta_1 = 15$, $\Delta_2 = 60$, and $\Delta_3 = 79$

Figure 27(c): $\Delta_1 = 4$, $\Delta_2 = 10$, and $\Delta_3 = 13$

The results from all computational runs are summarized in Figures 28, 29, 30 and 31.* From the following explanation of the trends and meaning of these maps, it should become evident how they are to be used for particular applications. Note that for such applications in addition to figuring out the pertinent $\tau_p$ and $\tau_s$ values one will need to decide the duration of the transient of interest ($t$) and also the extent of the downcomer area of non-interest (ANI), because of lack of welds, or embrittlement, expressed as $\ell/D$'s from the cold-leg centerline.

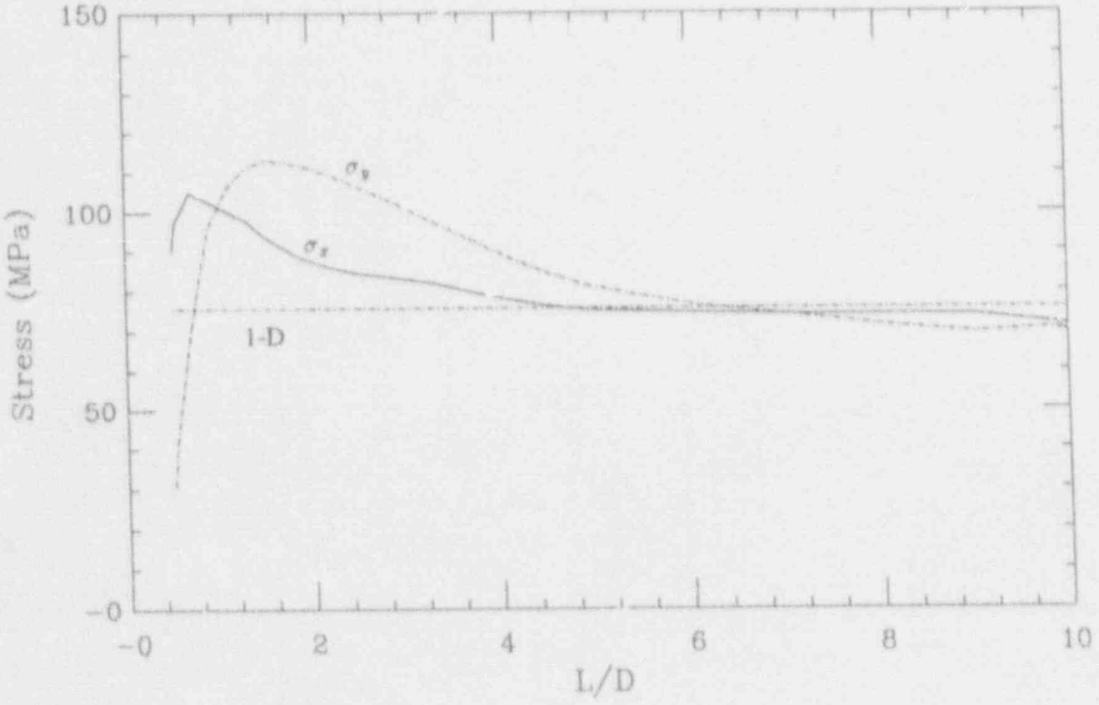


Figure 27(a). Stress distributions predicted by the vessel model compared to the 1D IPTS prescription. $\tau_s = 12016$ s, $\tau_p = 5095$ s and $t = 3000$ s.

* These figures also contain the HDR benchmark of Figure 26. Note that $\ell/D_{CL}$ for HDR is 0.63 as compared to a value of 0.29 for calvert cliffs, so strictly speaking the HDR results do not belong (they do not satisfy geometric simmilarity). However, the two time ratios dominate in any case, and the comparison shown is still appropriate.

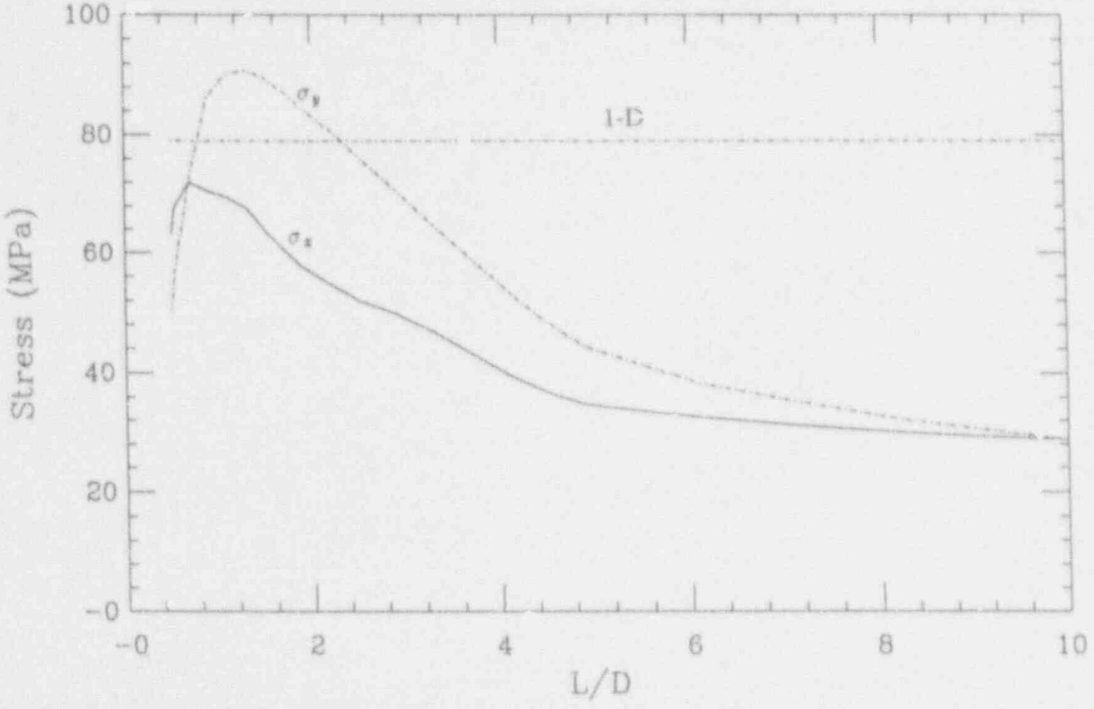


Figure 27(b). Stress distributions predicted by the vessel model compared to the 1D IPTS prescription. $\tau_s = 12016$ s, $\tau_p = 5095$ s and $t = 240$ s.

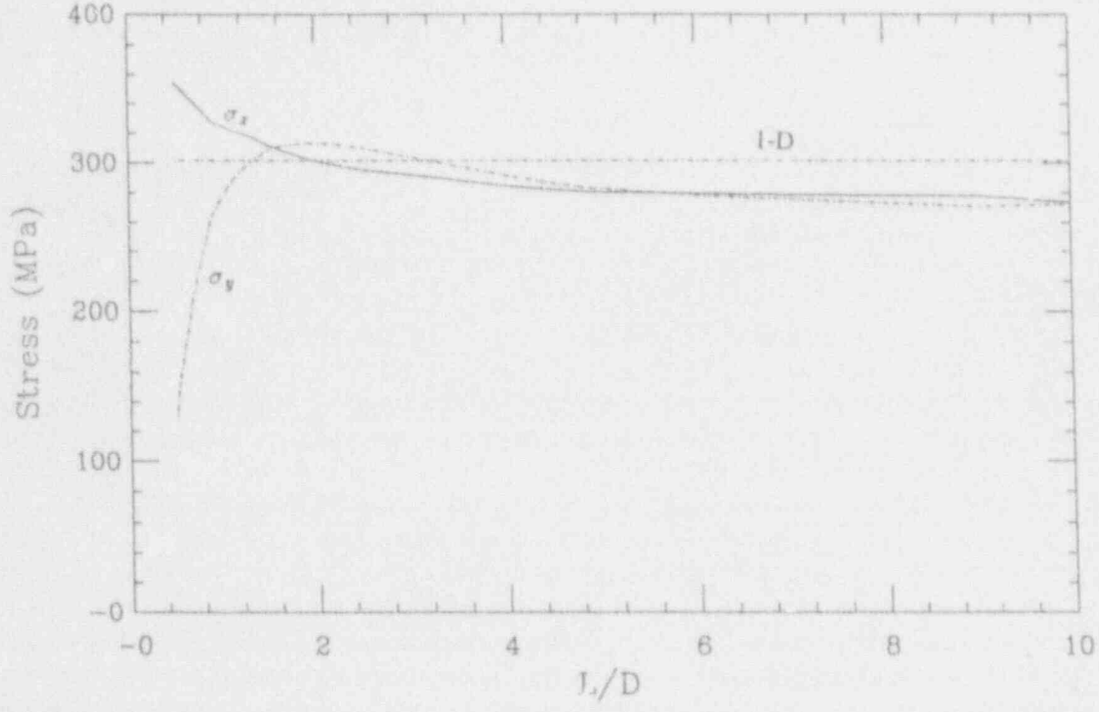


Figure 27(c). Stress distributions predicted by the vessel model compared to the 1D IPTS prescription. $\tau_s = 637$ s, $\tau_p = 5095$ s and $t = 600$ s.

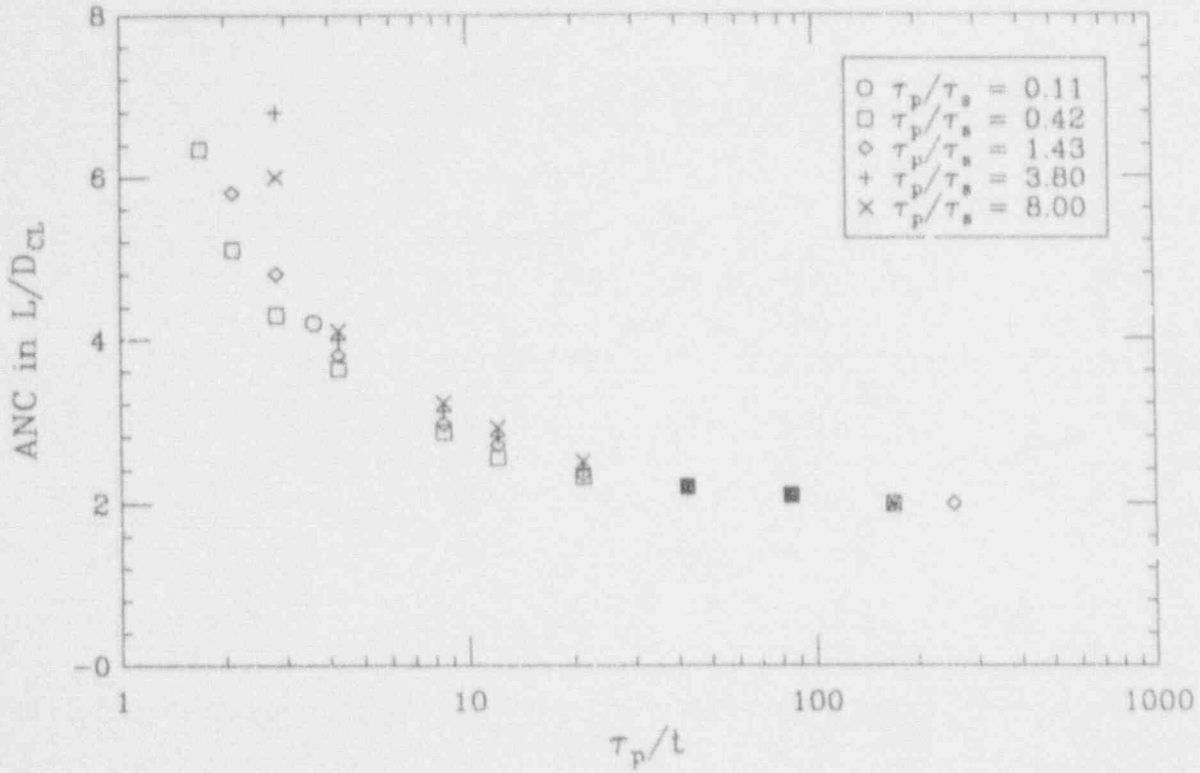


Figure 28. The downcomer length in L/D for which the prediction of the vessel model is higher than the 1D IPTS.

Turning now to Figure 29, we note that $\Delta_1$ is strongly dependent on $\tau_p/\tau_s$; as $\tau_p/\tau_s$ increases $\Delta_1$ decreases, approaching zero for $\tau_p/\tau_s \rightarrow 10$. We also see that the $\tau_p/t$ dependence has a minimum, going back up again as the $\tau_p/t$ decreases below a value of ~10. Typical values for reactors are $\tau_p/\tau_s = 4$. For the HDR test T32.18, $\tau_p/\tau_s = 0.1$; thus the strongly non-conservative trend in Figure 4 can be attributed to the atypically low value of $\tau_p/\tau_s$ in the HDR. For $\tau_p/\tau_s < 1$, the bahavior expresses a very slow cooldown in relation to conduction across the vessel wall, and as may be expected, the 1D approximation fails completely. In fact, at this limit the behavior is very much like the analytical ellipse results given in the introduction, i.e., high anisotropic stress levels (within the plume) which are much higher than those computed in the 1D approximation. At the other extreme, $\tau_p/\tau_s >> 1$, anisotrophy is strongly disfavored as the rapid (in relation to conduction) global cooldown drags $T_j$ down with it as the transient continues; thus the 1D stress field follows closely that developed in the plume region. To get into the $\tau_p/\tau_s$ range of lower than 2 for a reactor, the cooldown time constant must be over 2,000 s, i.e., the injection rate must be so slow that there would hardly be any plumes! Thus the region of "difficulty" cannot be approached under any circumstances with all HPI nozzles injecting. These trends are exactly analogous for the $\Delta_2$ and $\Delta_3$ indices, as shown in Figures 30 and 31. In a combined use of these figures we note that a large value of $\Delta_2$ or $\Delta_3$ in combination with a small value of $\Delta_1$ means that the 1D approximation is highly conservative for most of the area of the downcomer, while when all $\Delta_1$, $\Delta_2$, $\Delta_3$ are small the actual behavior is very much like 1D (as in Figure 27(c)).

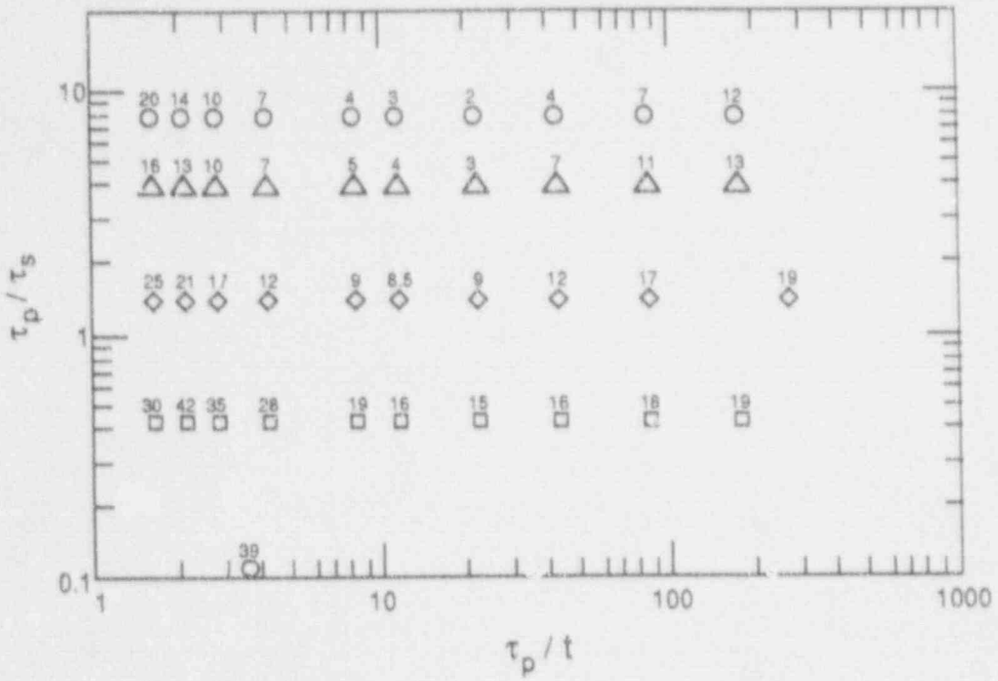


Figure 29. Map showing the extent of peak discrepancy between the 3D and 1D IPTS results.

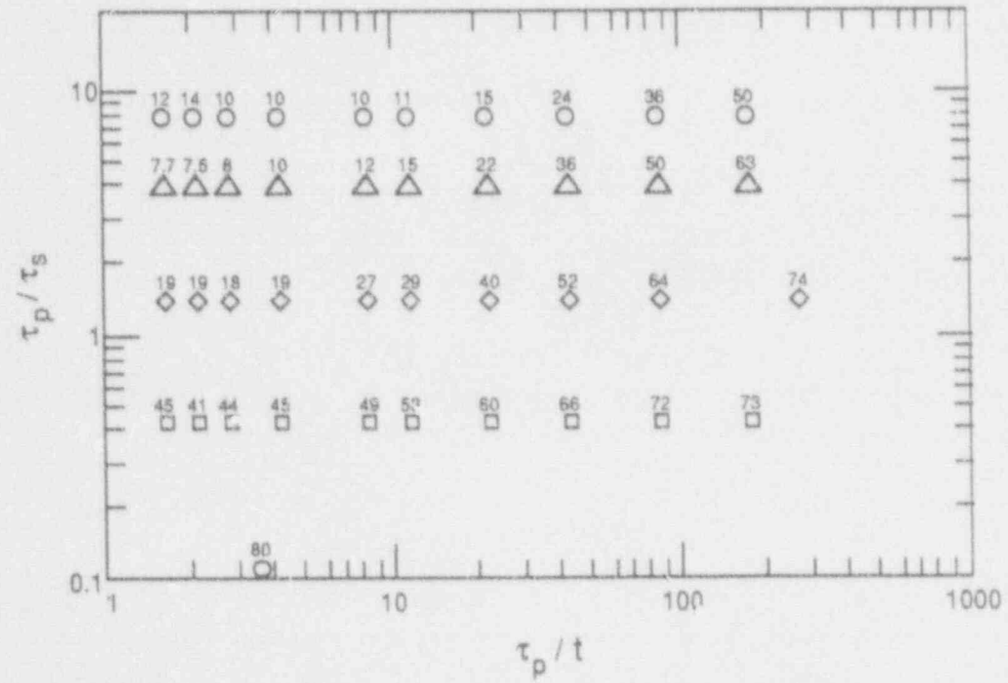


Figure 30. Map showing the deviation of the 3D results from the 1D IPTS one, over the upper half of the downcomer.

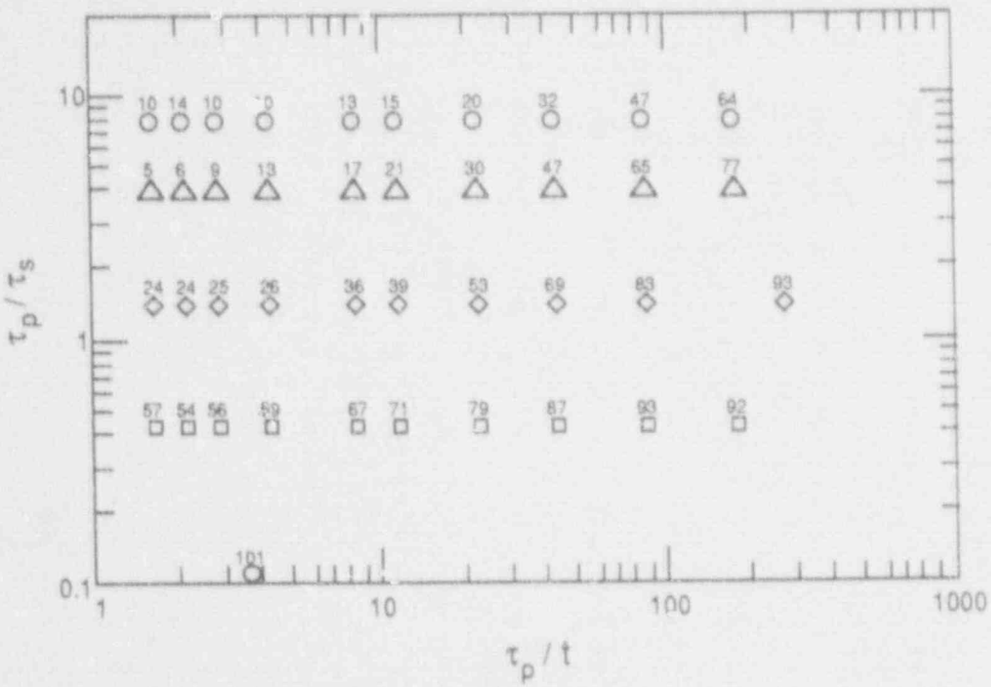


Figure 31. Map showing the deviation of the 3D results from the 1D IPTS one, over the whole 10ℓ/Ds of downcomer.

## 5. CONCLUSIONS

The applicability of the HDR tests to RPV wall stress behavior is shown to be remote in a subtle way. The primary reason for it is the 1-nozzle injection employed in these tests, but also the higher, than appropriate, injection rates contribute. The generalized regime maps together with the universal stratification solutions presented allow an *a priori* assessment of the possible area of difficulty in the 1D IPTS prescription. Also, these maps can be used to predict the general behavior of the 3D stress level on the basis of 1D stress results.

## REFERENCES


1. Cheverton, R.D. & D.G. Ball 1984. "OCA-P, A Deterministic and Probabilistic Fracture-Mechanics Code for Application to Pressure Vessels," NUREG/CR-3618, ORNL-5991, Oak Ridge National Lab.

2. Geiß, M. 1987. "Verification of OCA-P and VISA-II on Behalf of Strains and Stresses Induced During HDR-TEMB Thermal Mixing Tests," *Proc. 9th SMIRT Conf.*, Lausanne, August 1987, A.A. Balkema, Rotterdam.

3. Iyer, K. & T.G. Theofanous 1985. "Decay of Buoyancy Driven Stratified Layers with Applications to PTS: Reactor Predictions," *ANS Proceedings 1985 National Heat Transfer Conference*, Denver, CO, August 4–7, 1985, Vol. 1, p. 358, American Nuclear Society (1985). *Nuclear Science & Engineering* **108** 184–197 (1991).

4. Iyer, K., & T.G. Theofanous 1991a. "Decay of Buoyancy Driven Stratified Layers with Applications to Pressurized Thermal Shock: Reactor Predictions," *Nuclear Science & Engineering* **108** 184–197.

5. Iyer, K. & T.G. Theofanous 1991b. "Flooding-Limited Thermal Mixing: The Case of High Froude Injection," *Nuclear Science & Engineering* **108**, 198–207.

6. Neubrech, G.E., G. Katzenmeier & L. Wolf 1988. "Crack Initiation and Crack Growth during Thermal Shock Tests in the Reactor Pressure Vessel of the HDR under Corrosive Medium Conditions," *Int. J. Pres. Ves. & Piping*, **34**, 187-205.

7. Selby, D.L. et al. 1985a. "Pressurized Thermal Shock Evaluation of the Calvert Cliffs, Unit 1 Nuclear Power Plant," NUREG/CR-4022, ORNL/TM-9408, Oak Ridge National Lab.

8. Selby, D.L. et al. 1985b. "Pressurized Thermal Shock Evaluation of the H.B. Robinson Unit 2 Nuclear Power Plant," NUREG/CR-4183, ORNL/TM-956, Oak Ridge National Lab.

9. Theofanous, T.G. & K. Iyer 1987. "Mixing Phenomena of Interest to SBLOCAs," *Nuc. Eng. Des.*, **102**, 91–103.

10. Theofanous, T.G., J.L. La Chance & K.A. Williams 1989. "The Thermal Hydraulics of Small-Break Loss-of-Coolant Accidents Relative to Pressurized Thermal Shock," *Nuclear Science & Engineering* **102**, 74–100.

11. Theofanous, T.G. & H.P. Nourbakhsh 1982. "PWR Downcomer Fluid Temperature Transients Due to High Pressure Injection at Stagnated Loop Flow," *Proc. Joint NRC/ANS Meeting on Basic Thermal Hydraulic Mechanisms in LWR Analysis*, Bethesda, Maryland, Sept. 14–15, 1982, NUREG/CP-0043, 583–613.

12. Theofanous, T.G. & H. Yan 1991. "Interpretation of Thermal Mixing Experiments from One-Fifth to Full Scale," NUREG/CR-5677, U.S. Nuclear Regulatory Commission.

13. Turner, J.S. 1973. **Buoyancy Effects in Fluids**, Cambridge University Press, New York.

# APPENDIX

## DETAILED STRESS DISTRIBUTIONS FOR ALL COMPUTATIONAL RUNS

The figures in this appendix, —— $\sigma_z$, — · — $\sigma_y$, and the horizontal — · —, are keyed by means of the computational run number and the table below to respective conditions.

Table A.1. List of computational runs

Runs from 2-1 to 2-10 are for Calvert Cliffs reactor.
Others are obtained by varying the system volume only.

| Run # | $\tau_s$ (s) | $\tau_p$ (s) | t (s) | $T_m$ (°C) | $T_j$ (°C) |
|---|---|---|---|---|---|
| 1-1 | 3572 | 5095 | 20 | 275.0 | 220.8 |
| 1-2 | 3572 | 5095 | 60 | 272.4 | 248.0 |
| 1-3 | 3572 | 5095 | 120 | 268.3 | 244.2 |
| 1-4 | 3572 | 5095 | 240 | 260.7 | 237.0 |
| 1-5 | 3572 | 5095 | 420 | 250.0 | 228.0 |
| 1-6 | 3572 | 5095 | 600 | 241.6 | 218.5 |
| 1-7 | 3572 | 5095 | 1200 | 217.5 | 195.0 |
| 1-8 | 3572 | 5095 | 1800 | 199.4 | 177.5 |
| 1-9 | 3572 | 5095 | 2400 | 185.3 | 163.9 |
| 1-10 | 3572 | 5095 | 3000 | 174.0 | 152.6 |
| 2-1 | 1324 | 5095 | 30 | 270.9 | 246.6 |
| 2-2 | 1324 | 5095 | 60 | 265.3 | 241.3 |
| 2-3 | 1324 | 5095 | 120 | 254.9 | 231.2 |
| 2-4 | 1324 | 5095 | 240 | 236.7 | 213.8 |
| 2-5 | 1324 | 5095 | 420 | 214.2 | 191.8 |
| 2-6 | 1324 | 5095 | 600 | 195.7 | 174.0 |
| 2-7 | 1324 | 5095 | 1200 | 152.3 | 131.4 |
| 2-8 | 1324 | 5095 | 1800 | 125.0 | 107.7 |
| 2-9 | 1324 | 5095 | 2400 | 106.7 | 92.5 |
| 2-10 | 1324 | 5095 | 3000 | 94.2 | 81.9 |
| 3-1 | 637 | 5095 | 30 | 265.0 | 241.0 |
| 3-2 | 637 | 5095 | 60 | 255.0 | 231.3 |
| 3-3 | 637 | 5095 | 120 | 238.5 | 215.6 |
| 3-4 | 637 | 5095 | 240 | 213.9 | 191.5 |
| 3-5 | 637 | 5095 | 420 | 188.6 | 167.1 |
| 3-6 | 637 | 5095 | 600 | 171.4 | 150.1 |
| 3-7 | 637 | 5095 | 1200 | 140.2 | 120.4 |
| 3-8 | 637 | 5095 | 1800 | 126.2 | 108.7 |
| 3-9 | 637 | 5095 | 2400 | 119.0 | 102.7 |
| 3-10 | 637 | 5095 | 3000 | 114.9 | 99.3 |
| 4-1 | 12016 | 5095 | 30 | 276.2 | 251.6 |
| 4-2 | 12016 | 5095 | 60 | 275.5 | 215.0 |
| 4-3 | 12016 | 5095 | 120 | 274.2 | 249.7 |
| 4-4 | 12016 | 5095 | 240 | 271.8 | 247.4 |
| 4-5 | 12016 | 5095 | 420 | 268.3 | 244.2 |
| 4-6 | 12016 | 5095 | 600 | 265.0 | 241.1 |
| 4-7 | 12016 | 5095 | 1200 | 255.3 | 231.6 |
| 4-8 | 12016 | 5095 | 1800 | 246.8 | 223.5 |
| 4-9 | 12016 | 5095 | 2400 | 239.3 | 216.3 |
| 4-10 | 12016 | 5095 | 3000 | 232.5 | 209.8 |

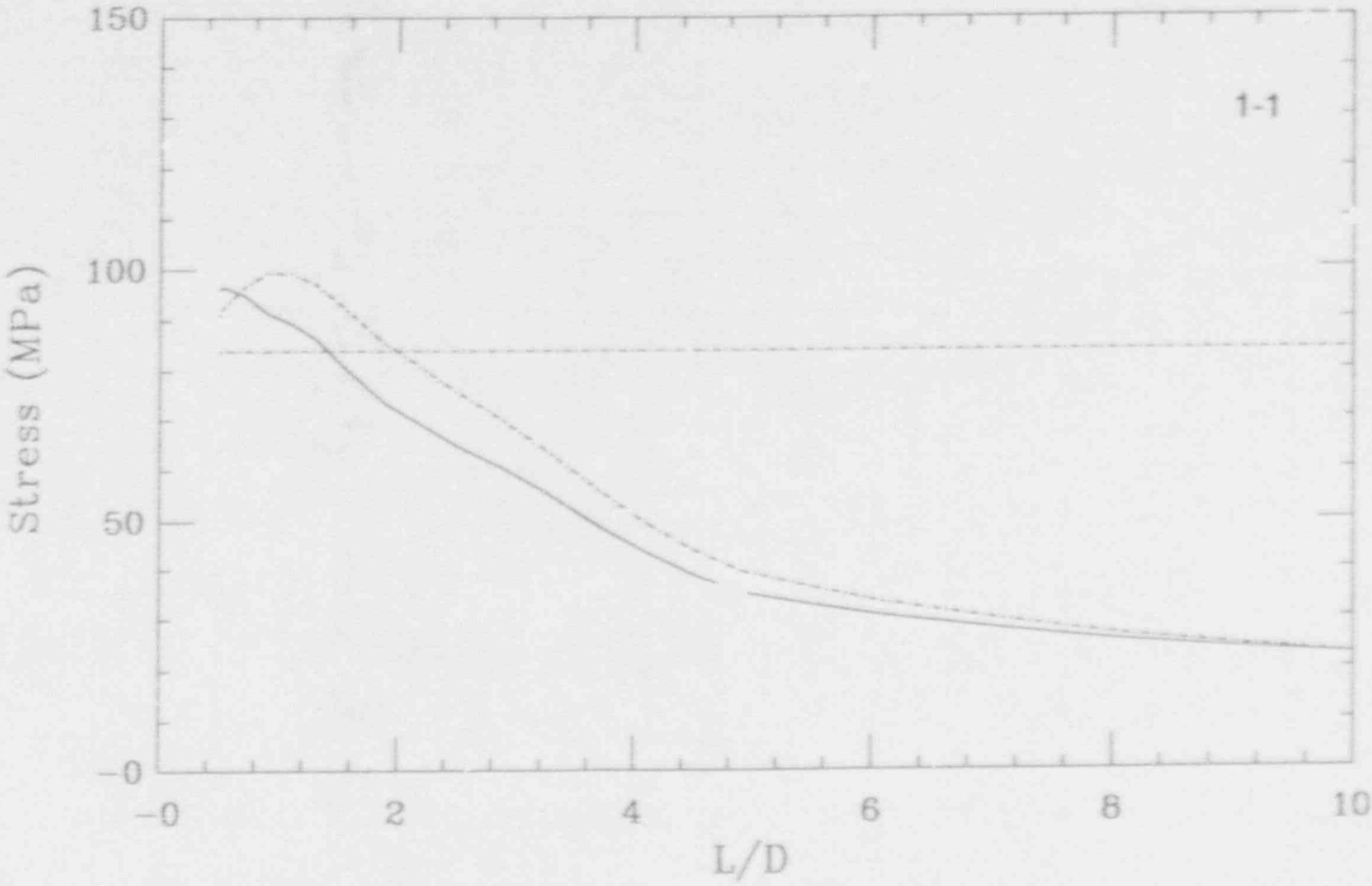
150
100
50
0
Stress (MPa)
1-1
0
2
4
6
8
10
L/D

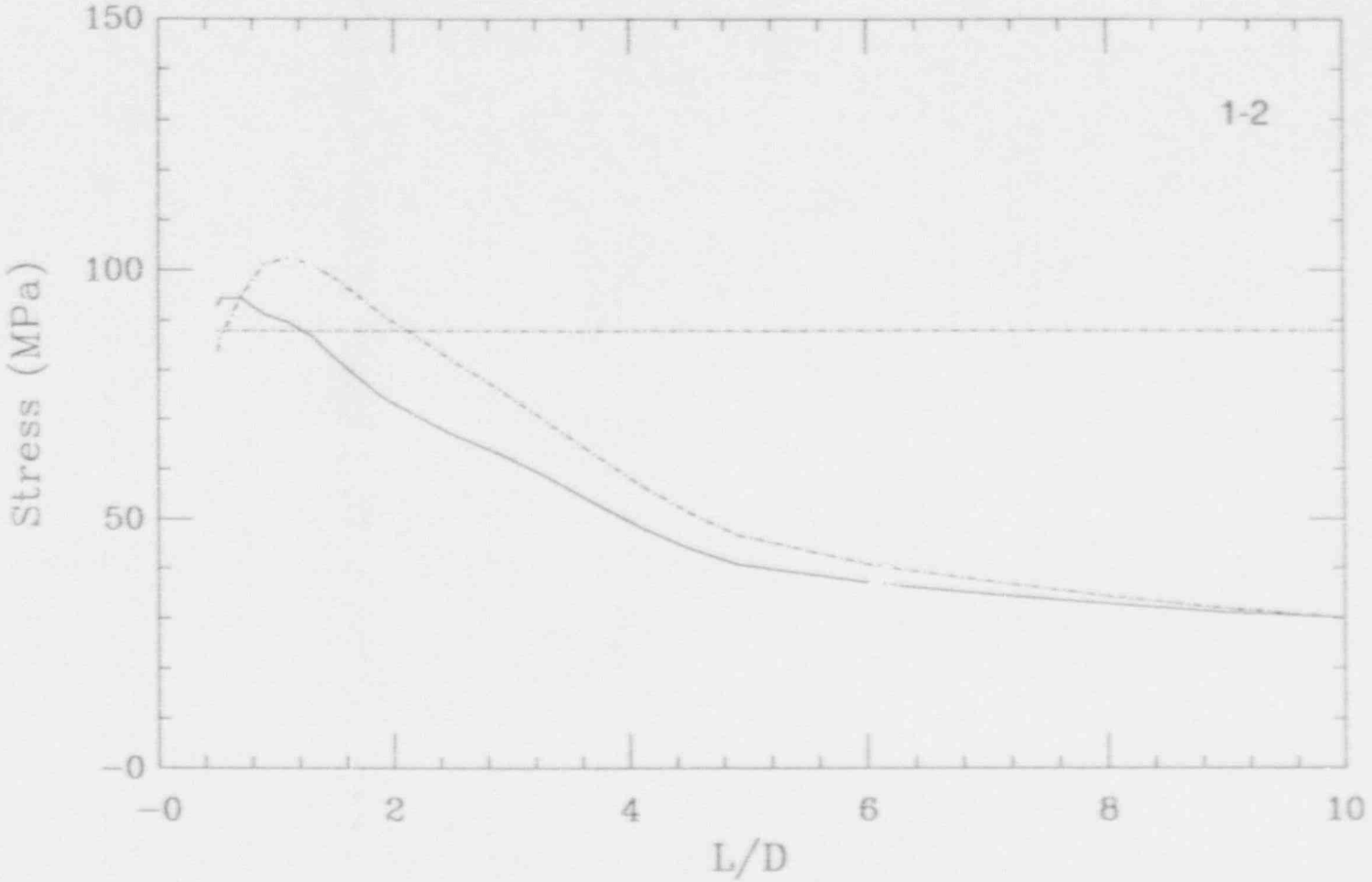
150
100
50
-0
Stress (MPa)
1-2
-0
2
4
6
8
10
L/D

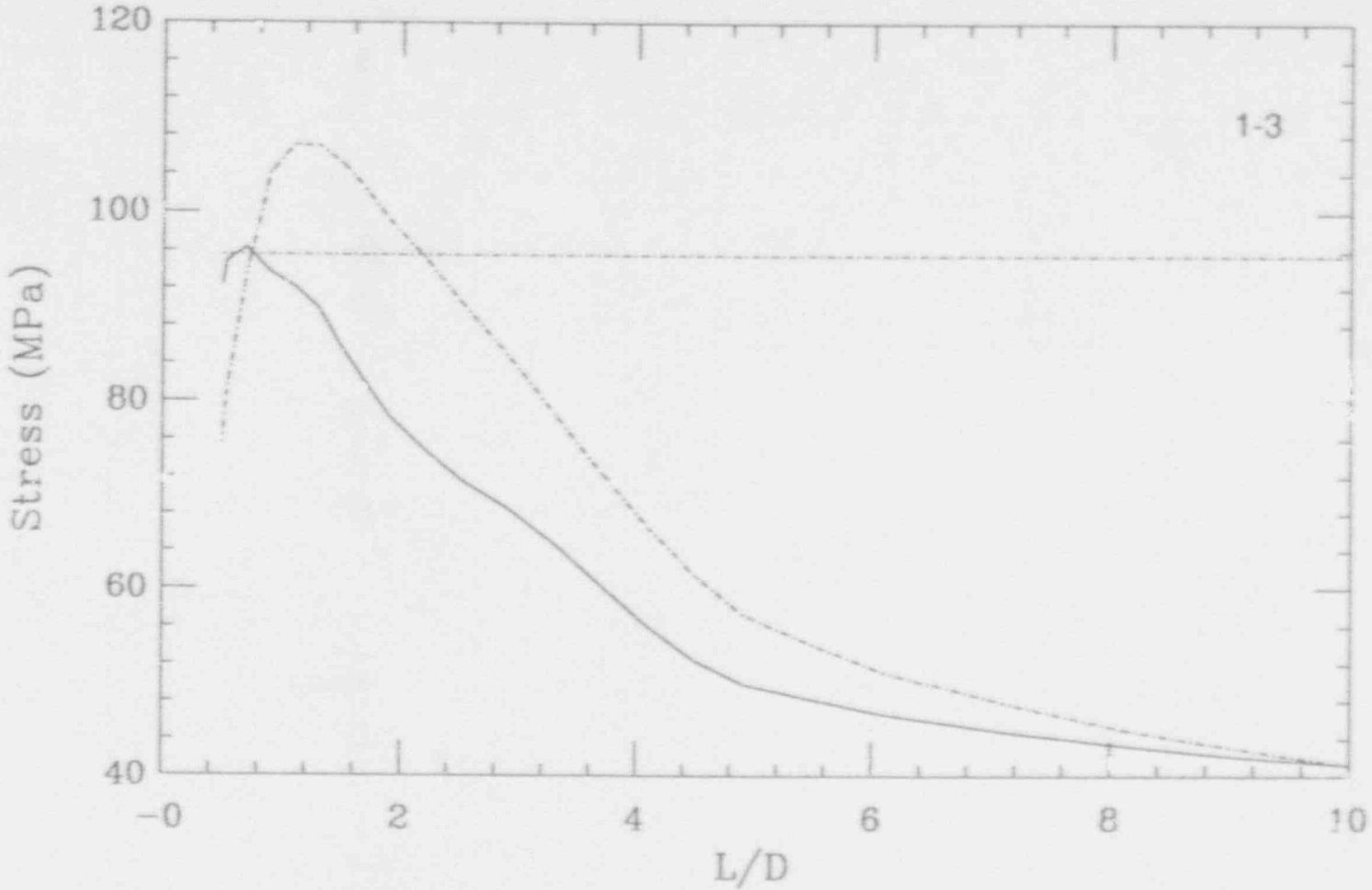
120
100
80
60
40
Stress (MPa)
1-3
−0
2
4
6
8
10
L/D

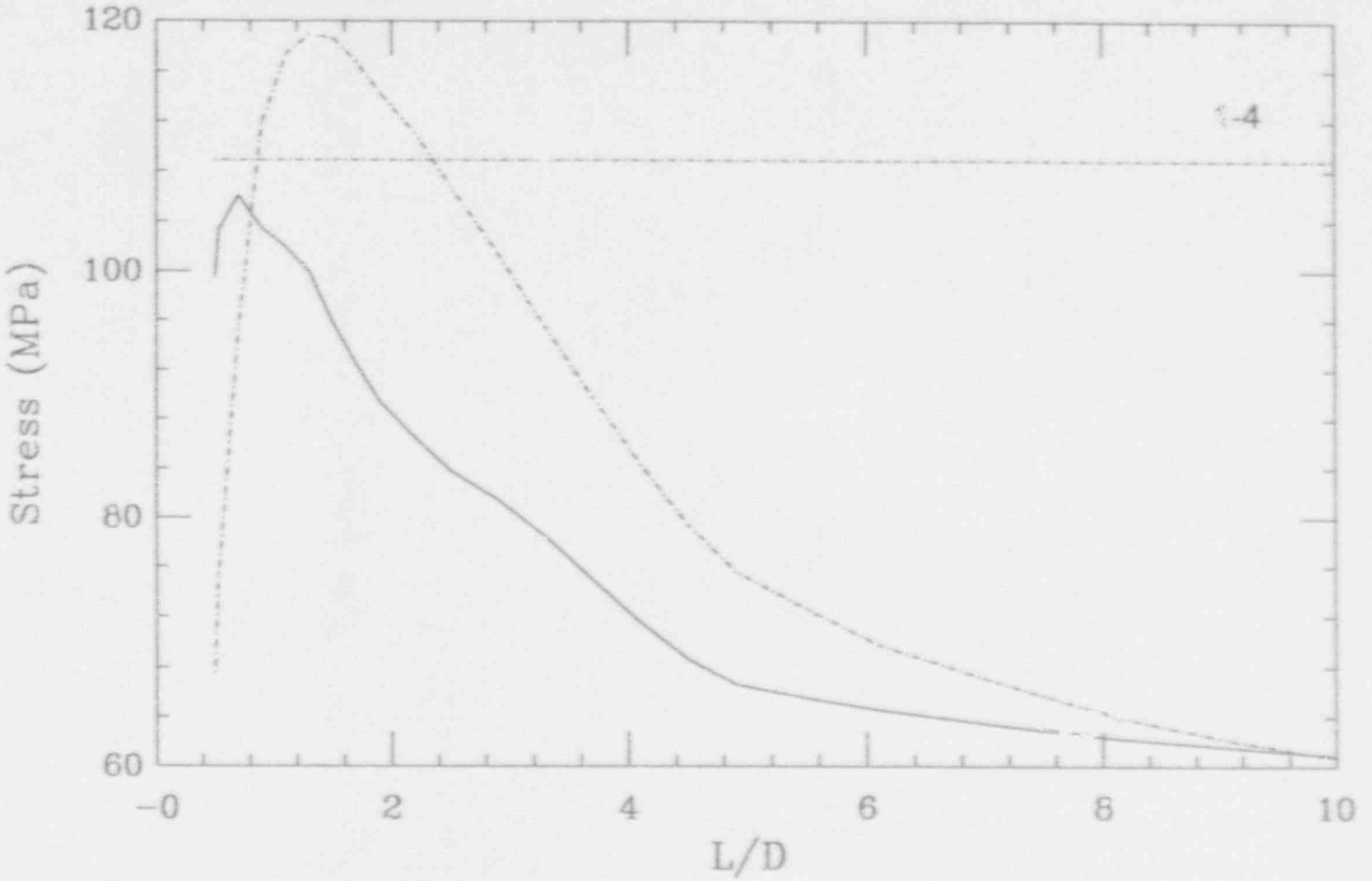
120
100
80
60
Stress (MPa)
1-4
-0
2
4
6
8
10
L/D

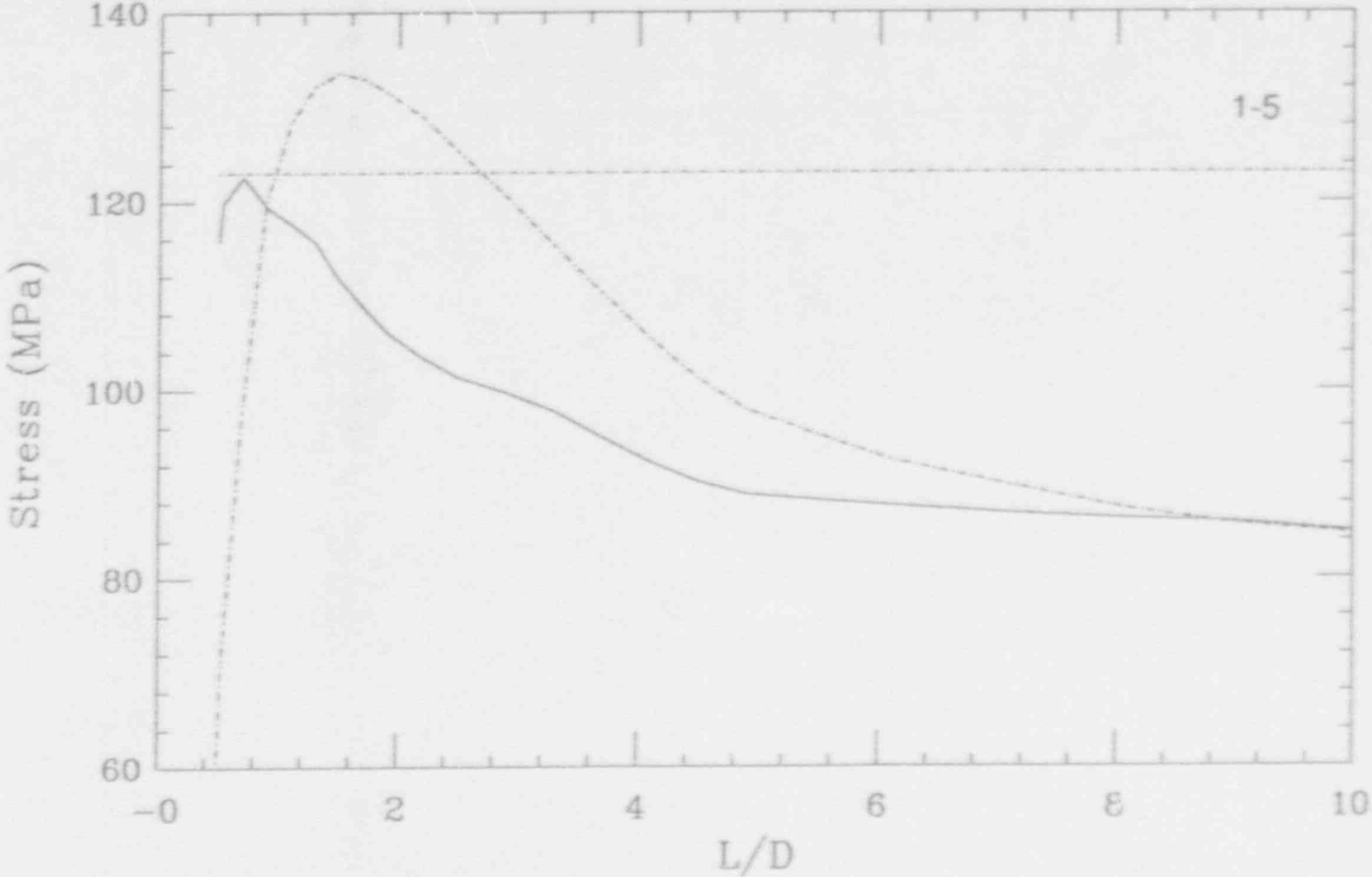
140
120
100
80
60
Stress (MPa)
1-5
−0
2
4
6
8
10
L/D

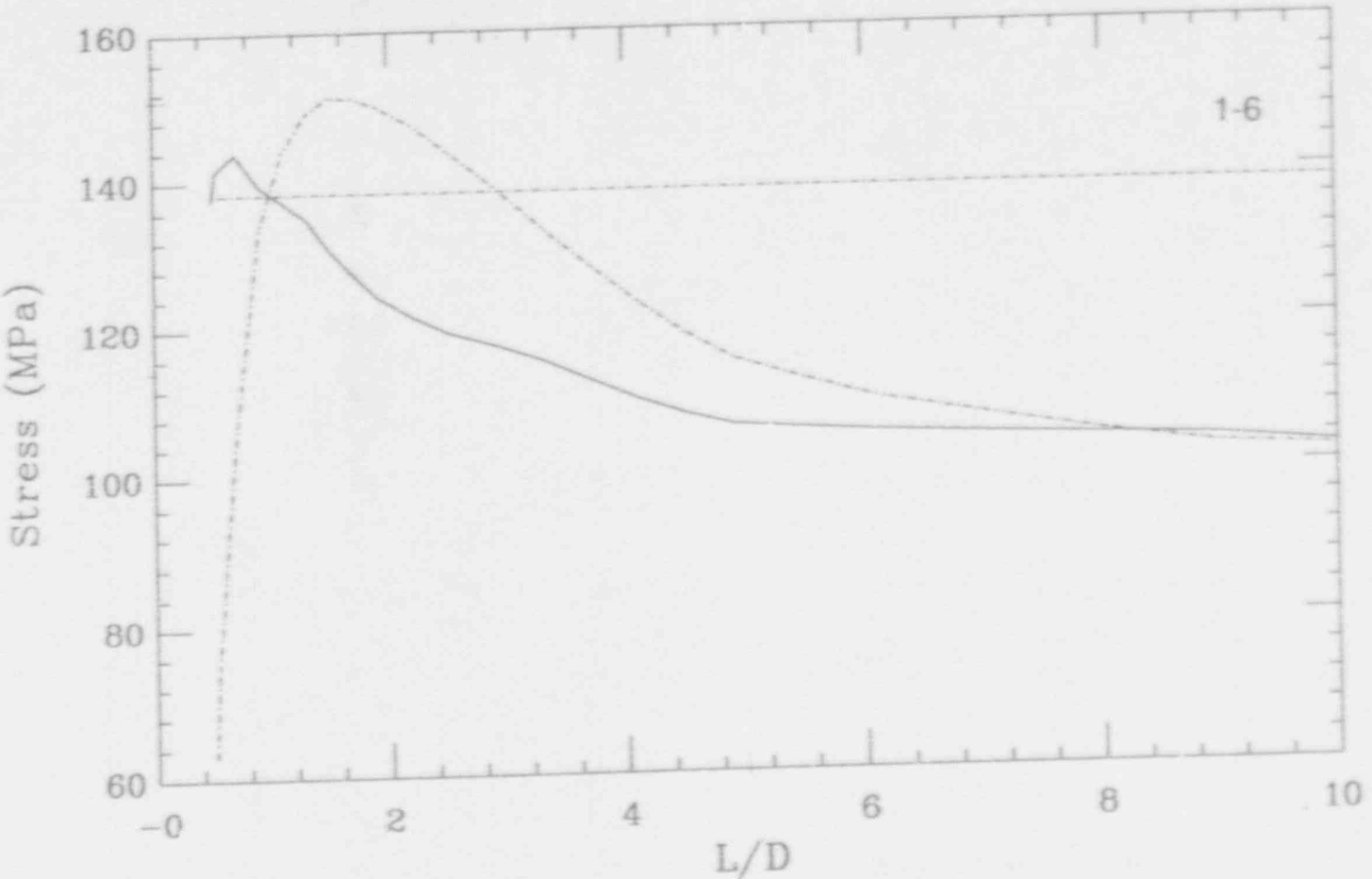
160
140
120
100
80
60
Stress (MPa)
1-6
-0
2
4
6
8
10
L/D

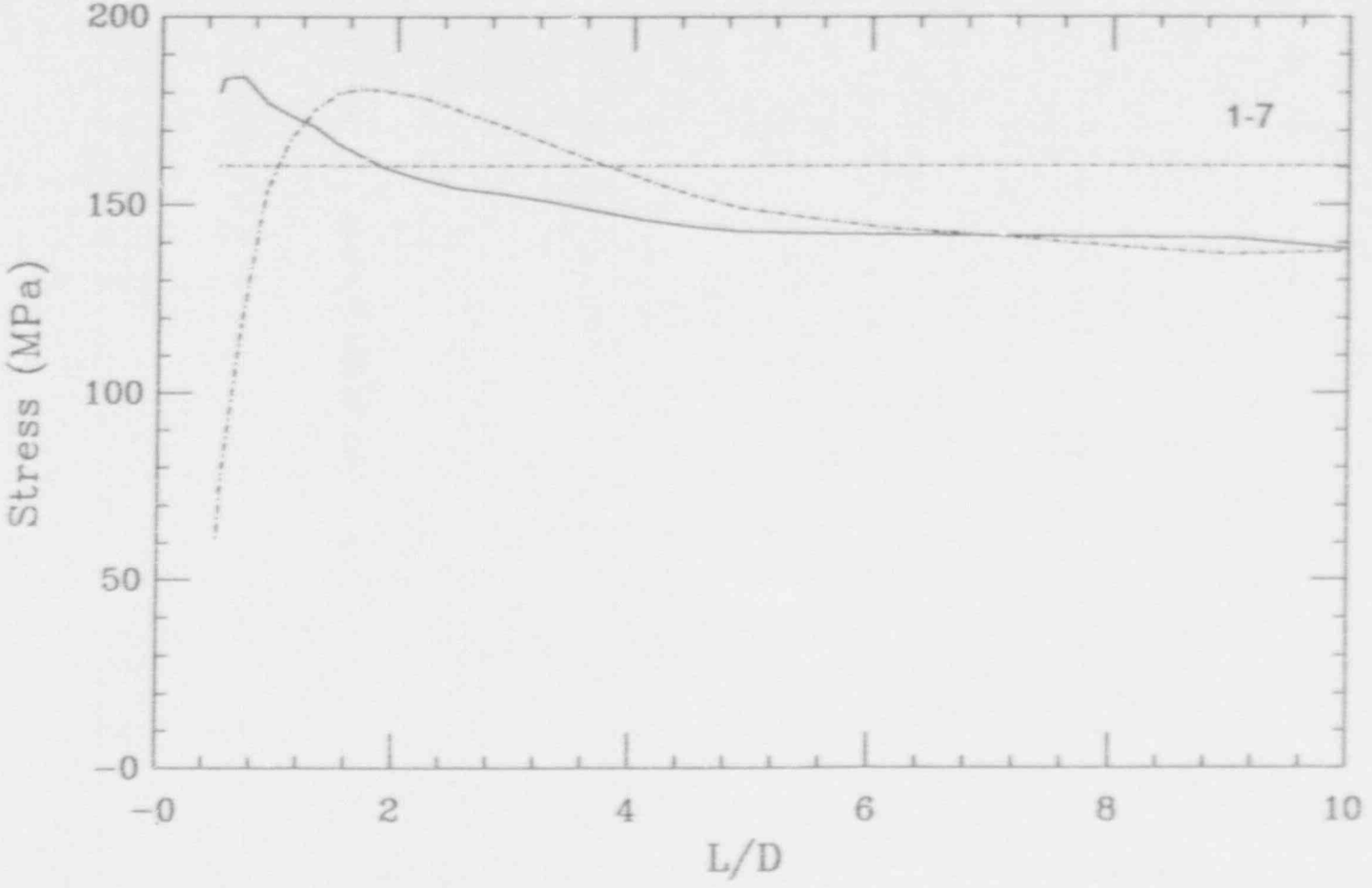
200
150
100
50
-0
Stress (MPa)
1-7
-0
2
4
6
8
10
L/D

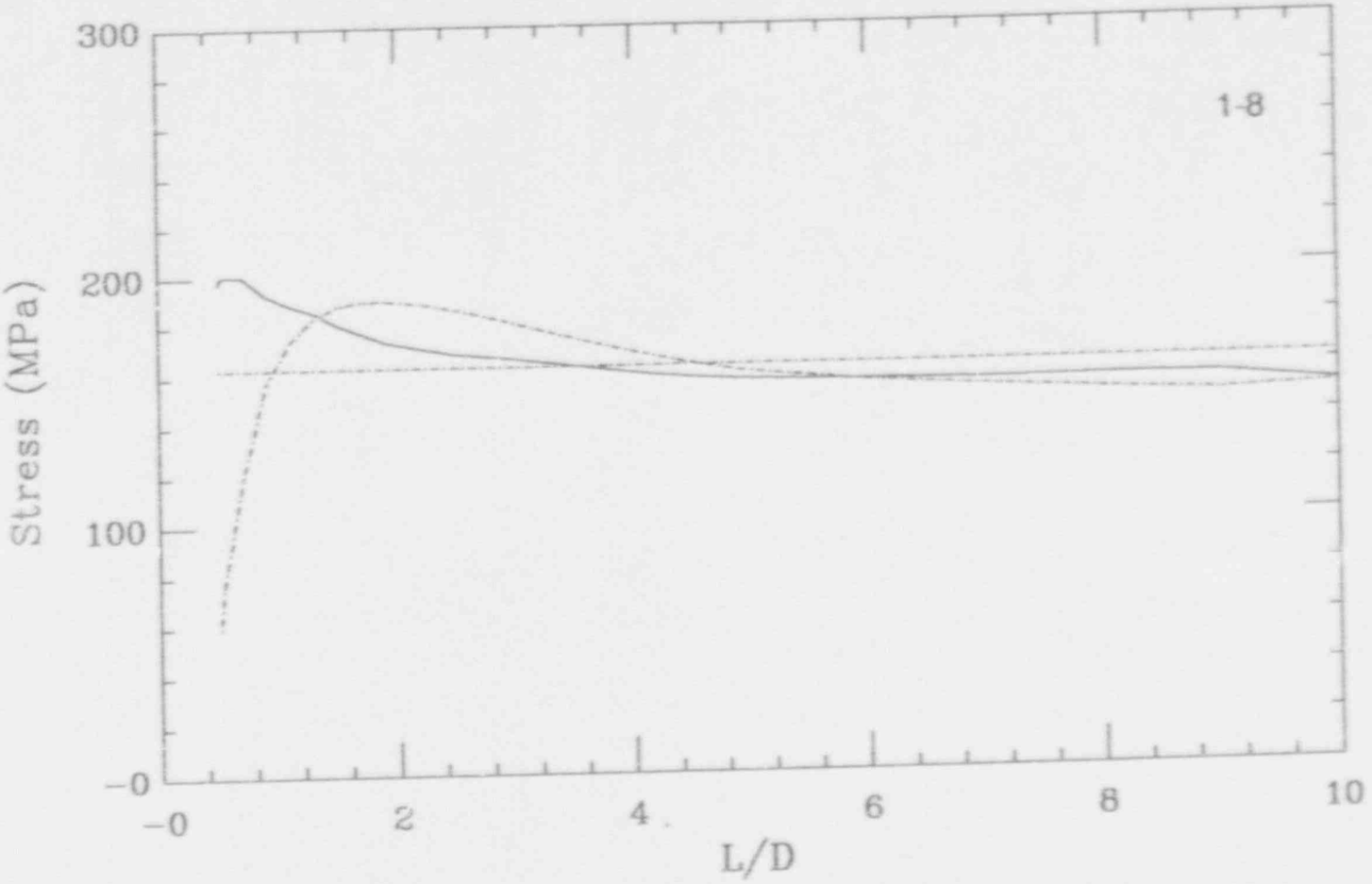
300
200
100
-0
Stress (MPa)
1-8
-0
2
4
6
8
10
L/D

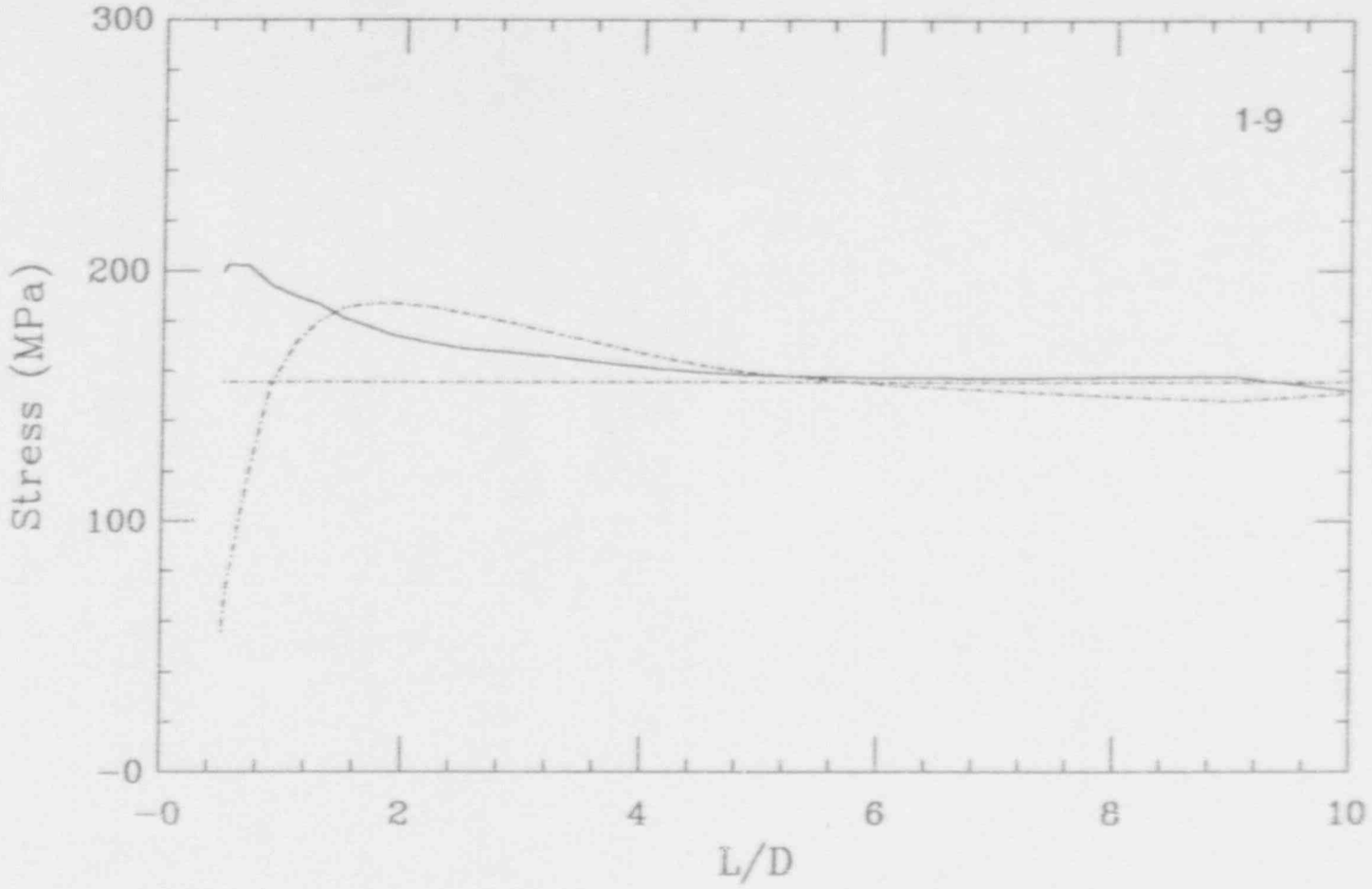
300
200
100
-0
Stress (MPa)
1-9
-0
2
4
6
8
10
L/D

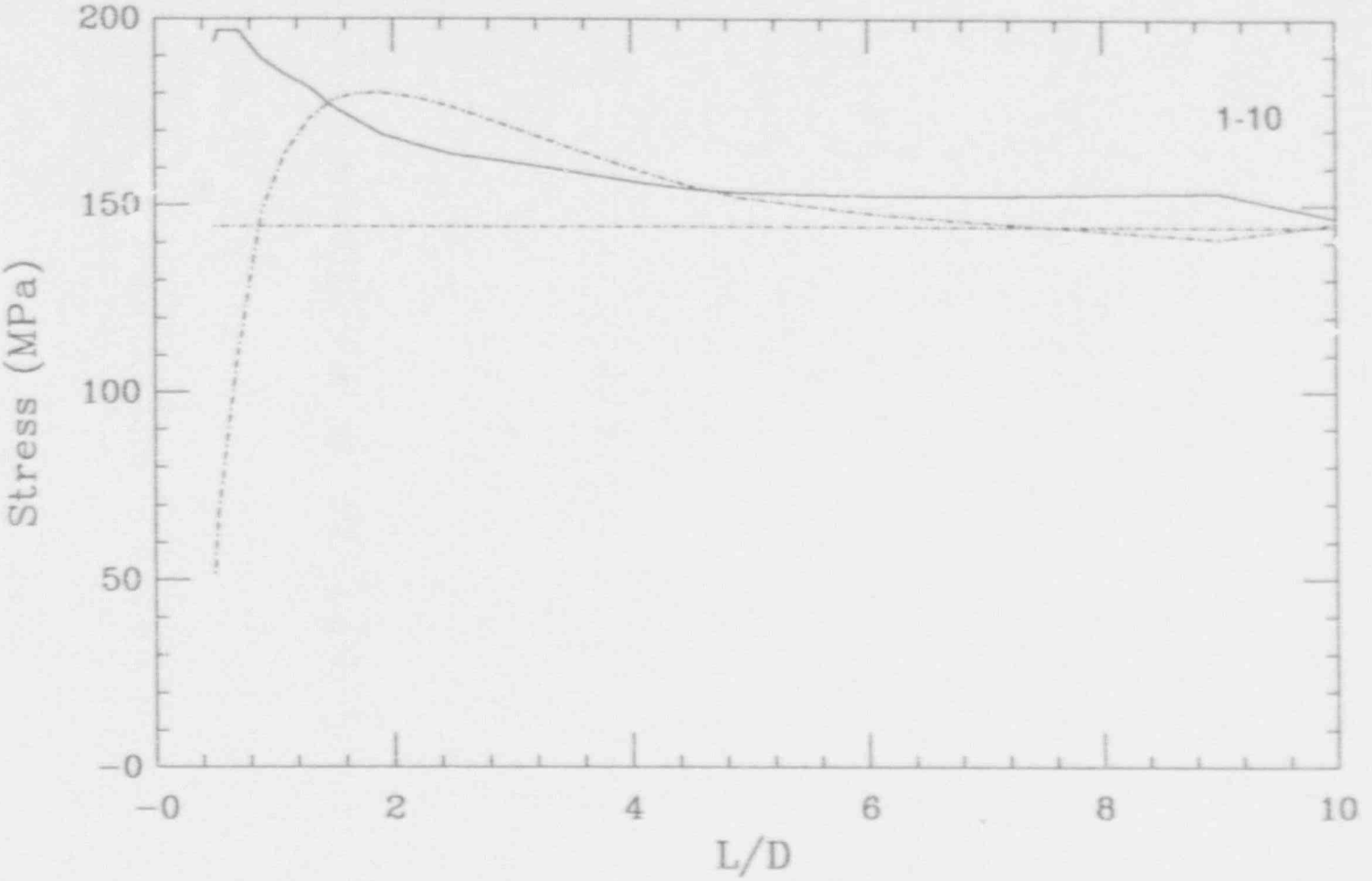
200
150
100
50
-0
Stress (MPa)
1-10
-0
2
4
6
8
10
L/D

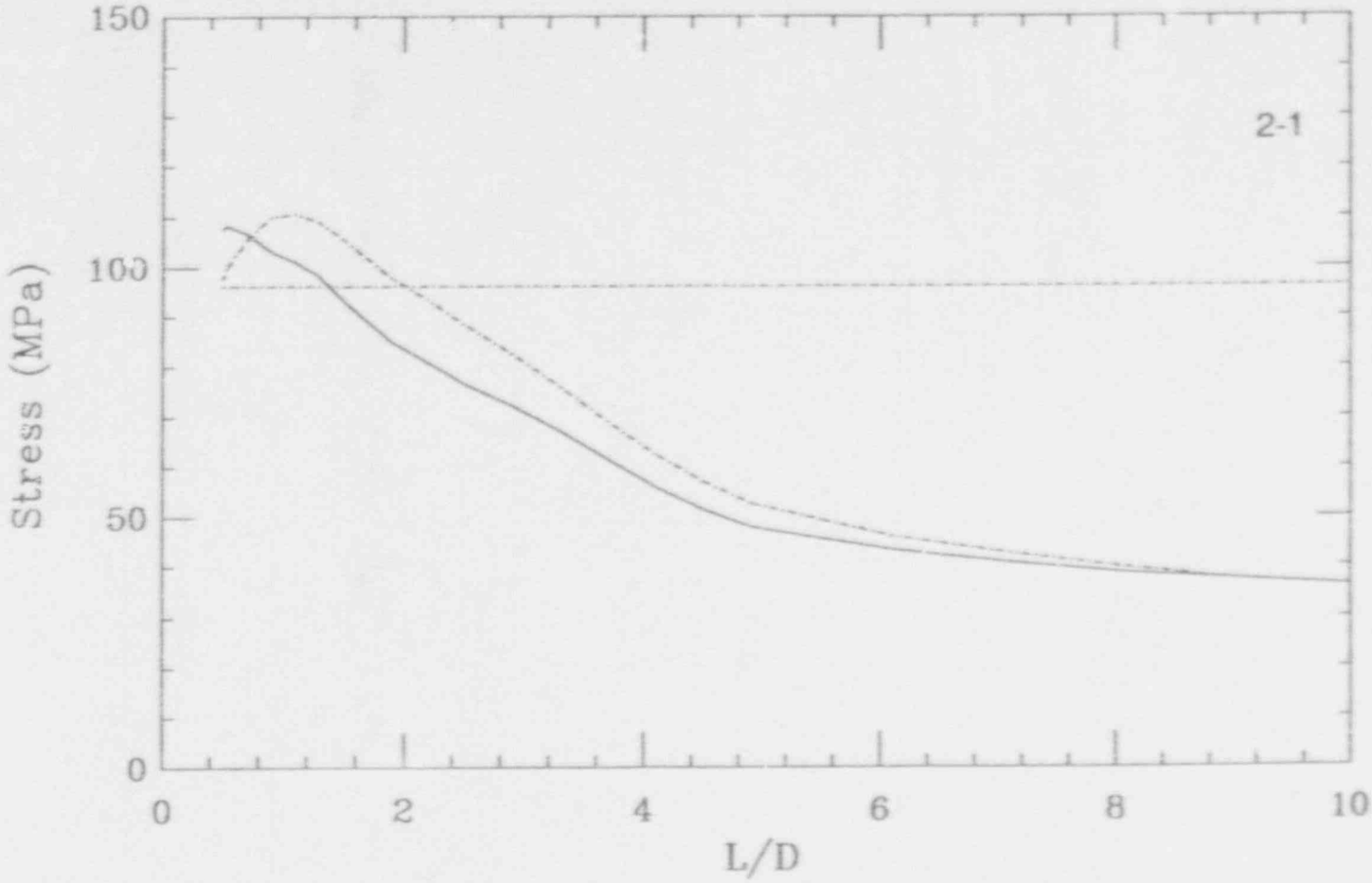
150
100
50
0
Stress (MPa)
2-1
0
2
4
6
8
10
L/D

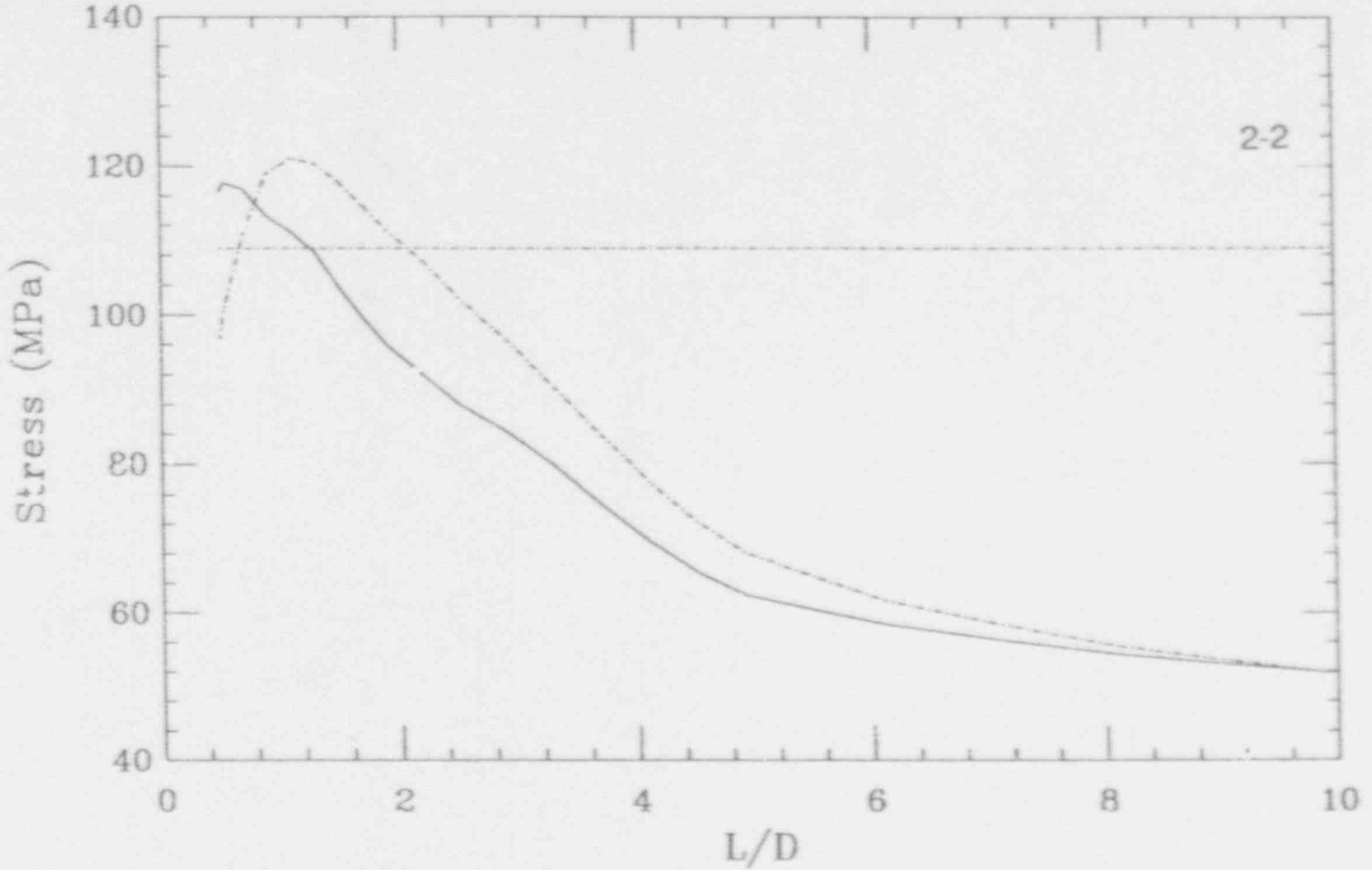
140
120
100
80
60
40
Stress (MPa)
0
2
4
6
8
10
L/D
2-2

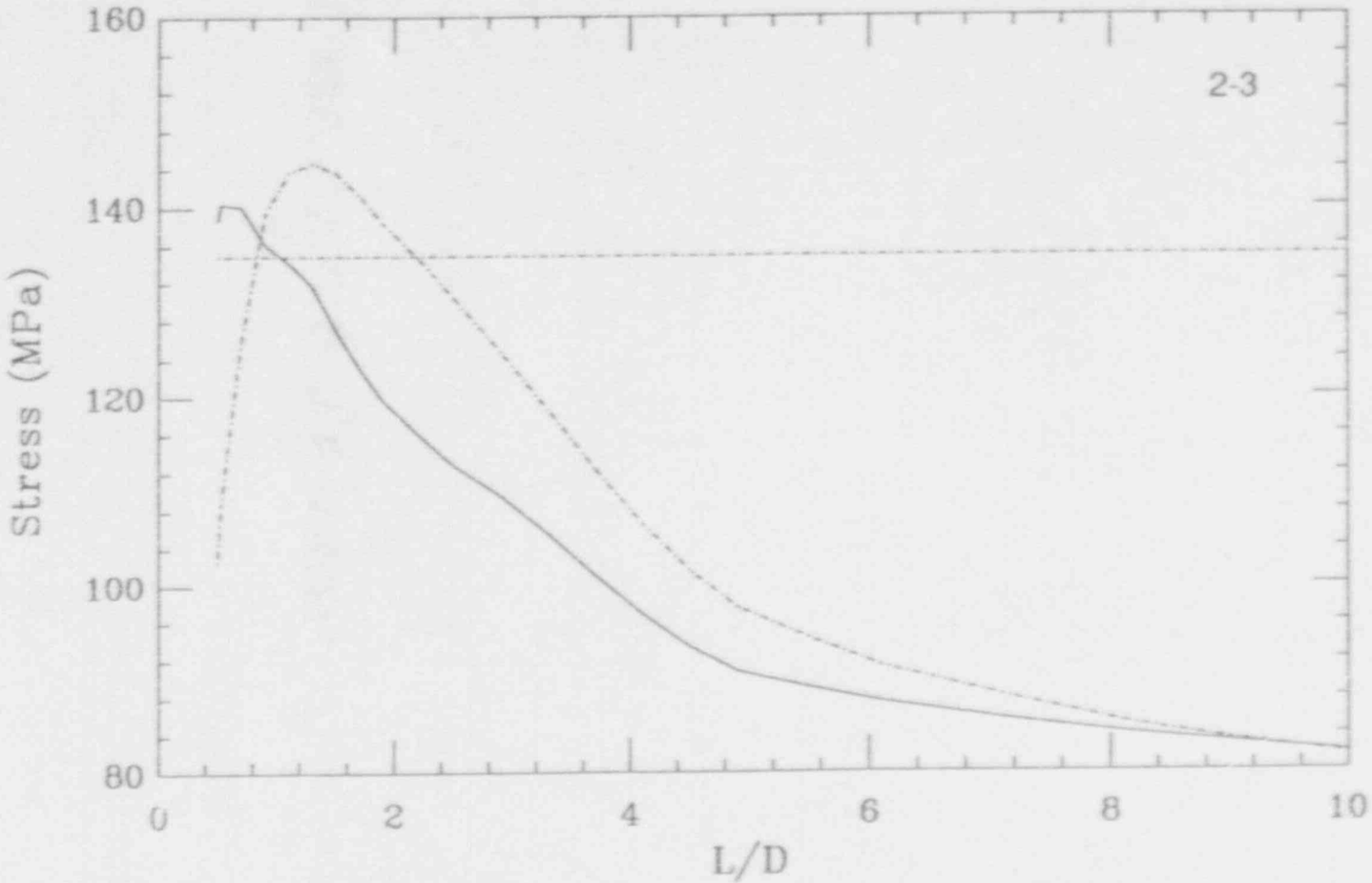
2-3
160
140
120
100
80
Stress (MPa)
0
2
4
6
8
10
L/D

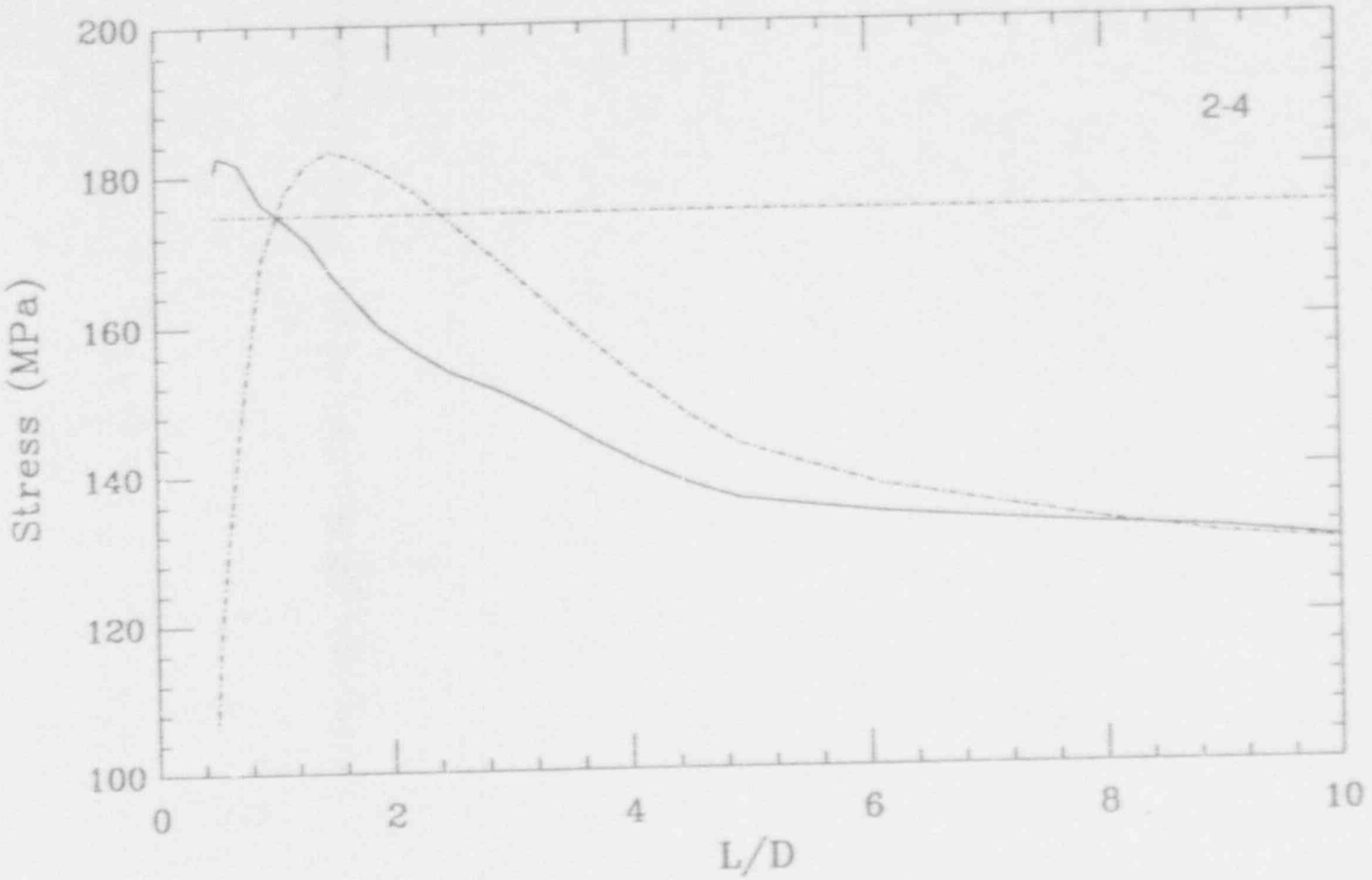
2-4
200
180
160
140
120
100
Stress (MPa)
0
2
4
6
8
10
L/D

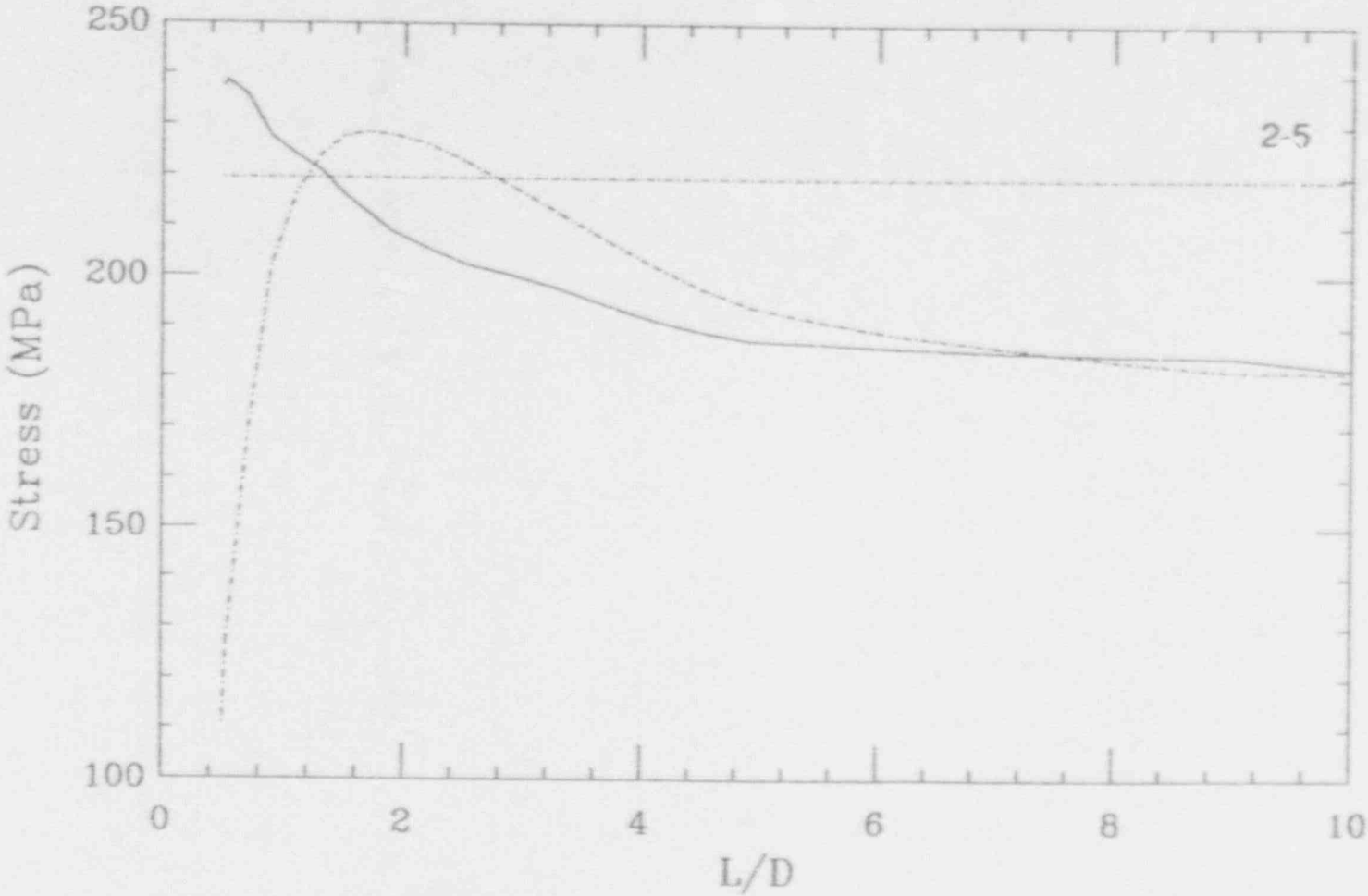
250
200
150
100
0
2
4
6
8
10
Stress (MPa)
L/D
2-5

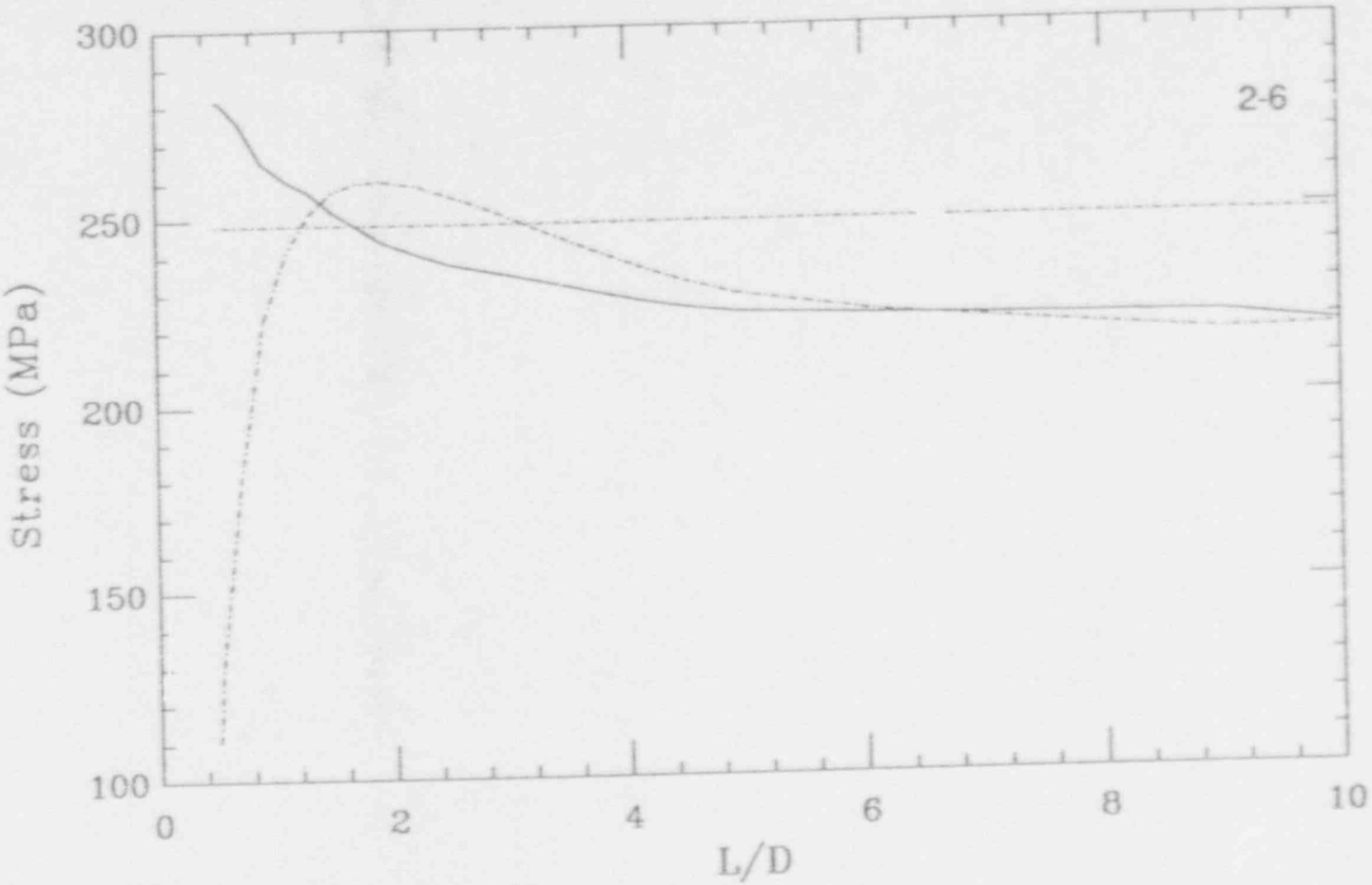
2-6
300
250
200
150
100
Stress (MPa)
0
2
4
6
8
10
L/D

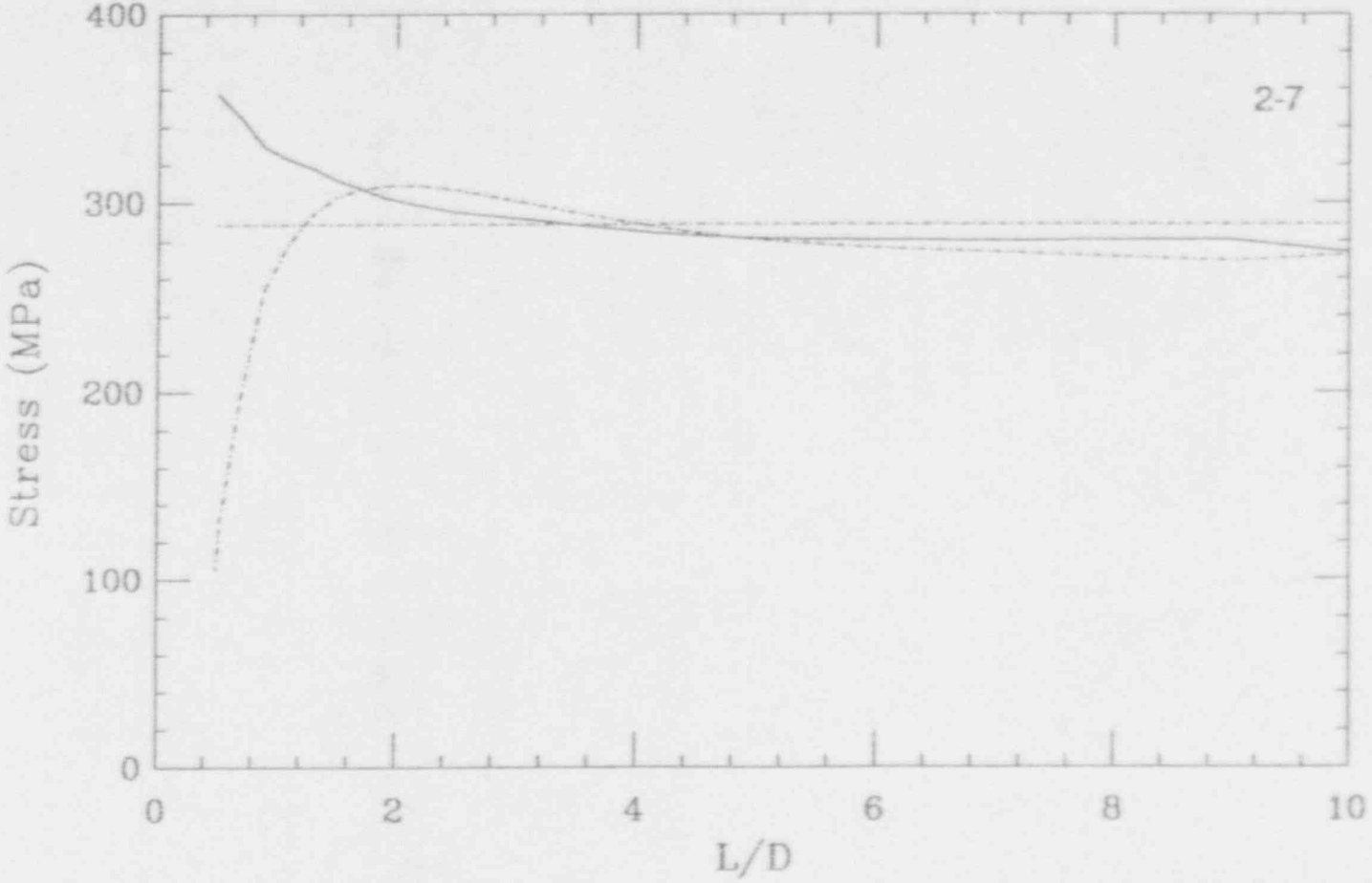
2-7
400
300
200
100
0
Stress (MPa)
0
2
4
6
8
10
L/D

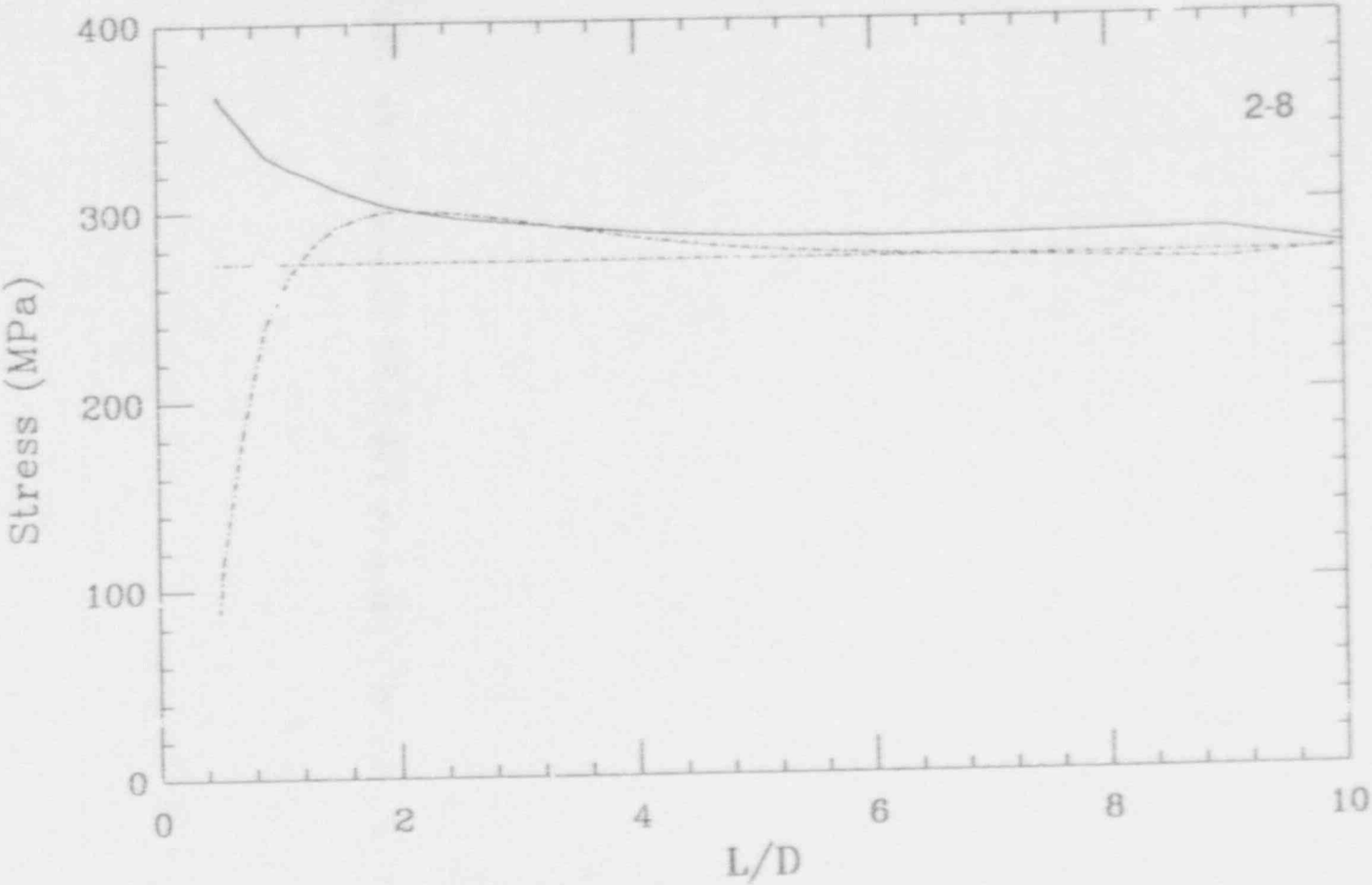
400
300
200
100
0
Stress (MPa)
2-8
0
2
4
6
8
10
L/D

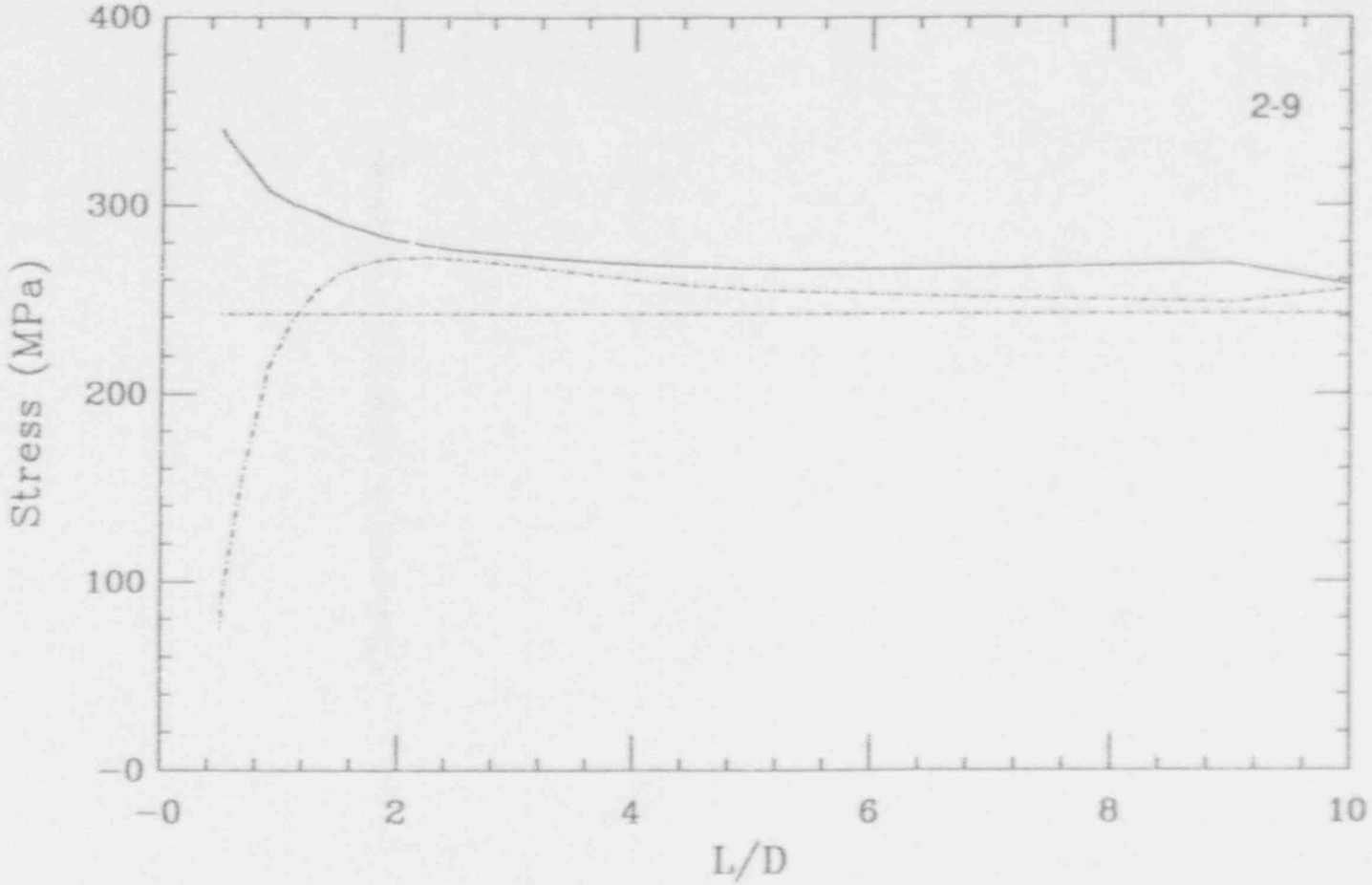
2-9
400
300
200
100
-0
Stress (MPa)
-0
2
4
6
8
10
L/D

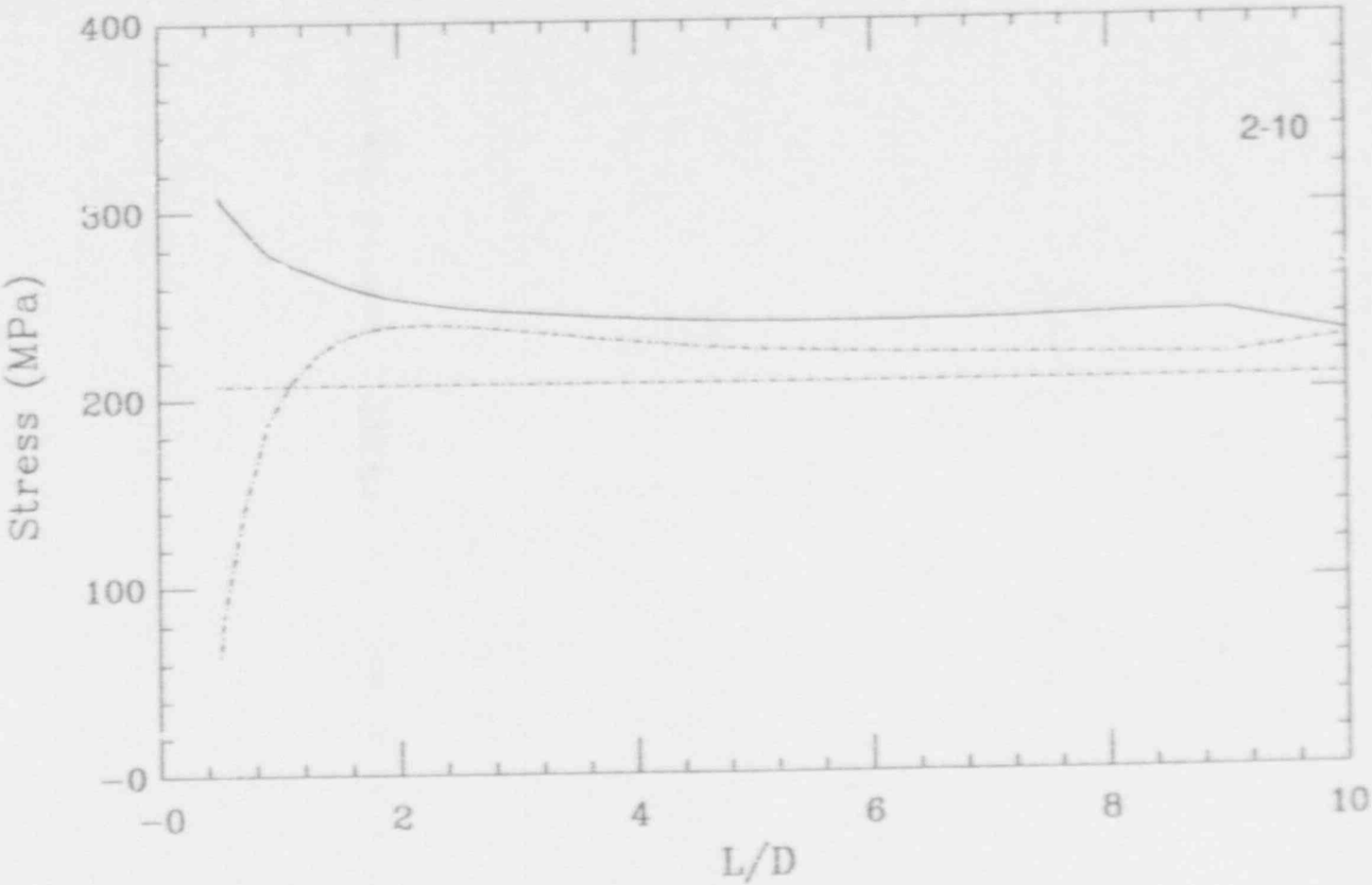
400
300
200
100
-0
Stress (MPa)
2-10
-0
2
4
6
8
10
L/D

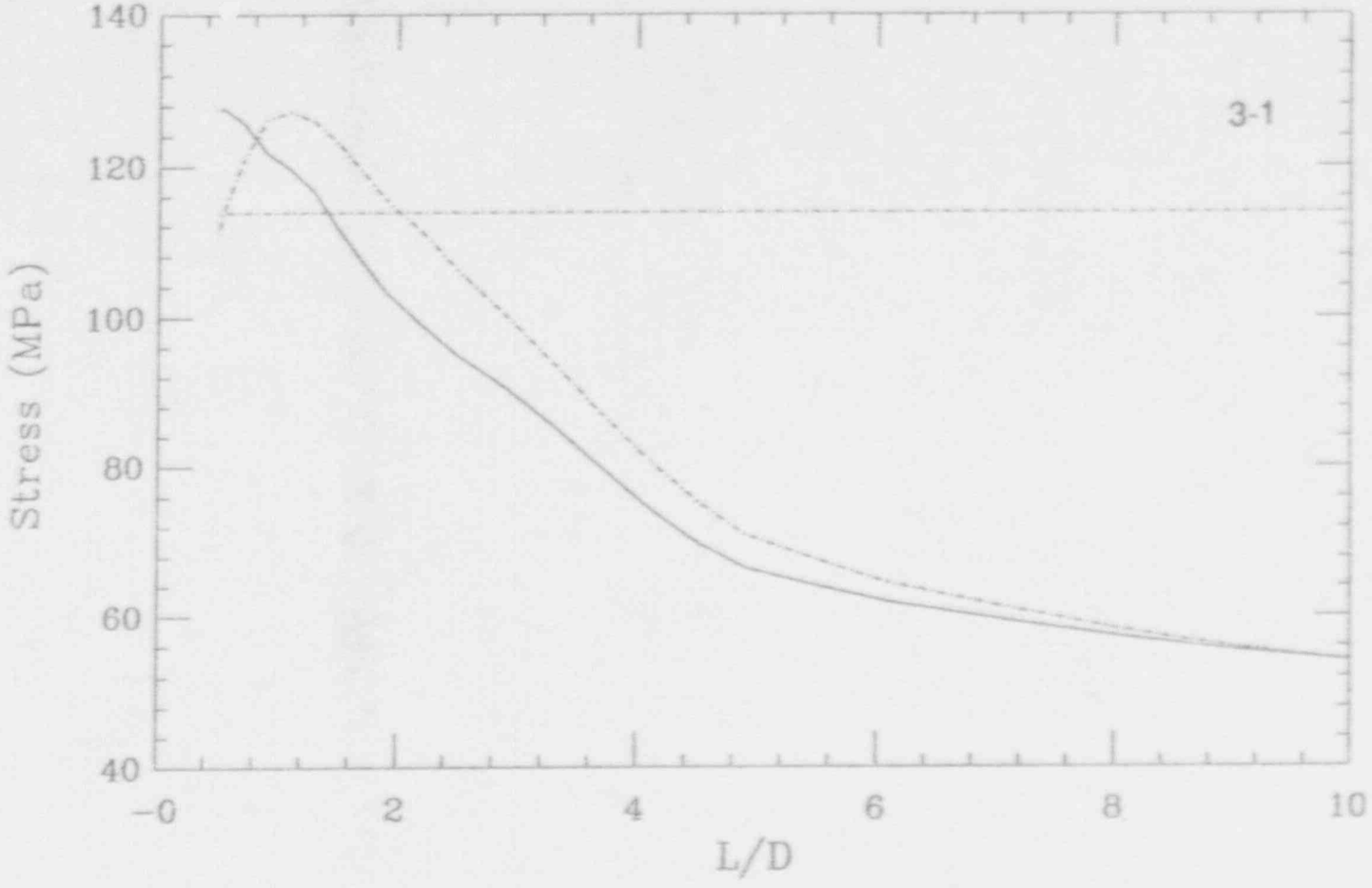
3-1
140
120
100
80
60
40
Stress (MPa)
-0
2
4
6
8
10
L/D

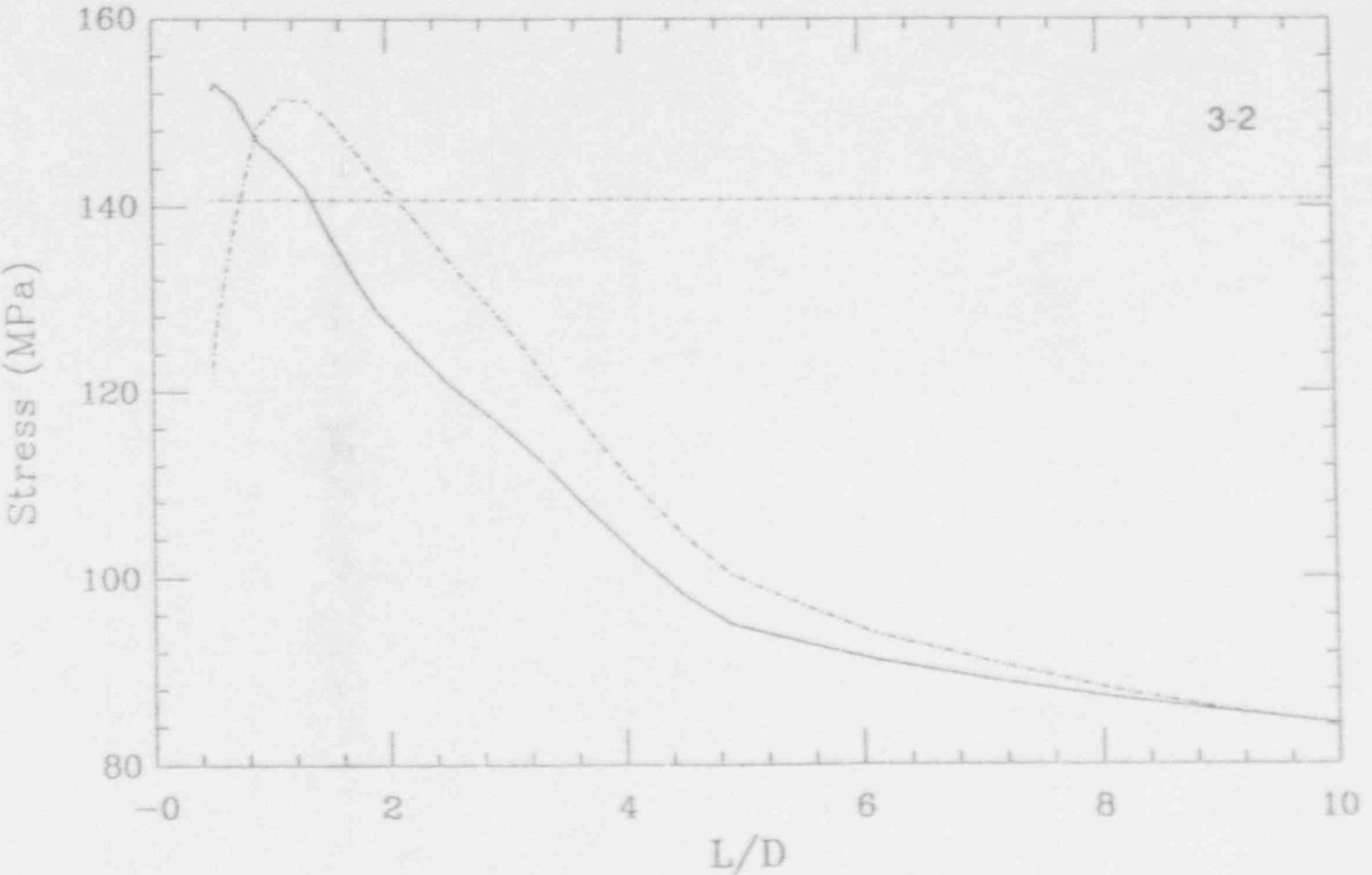
160
140
120
100
80
Stress (MPa)
3-2
-0
2
4
6
8
10
L/D

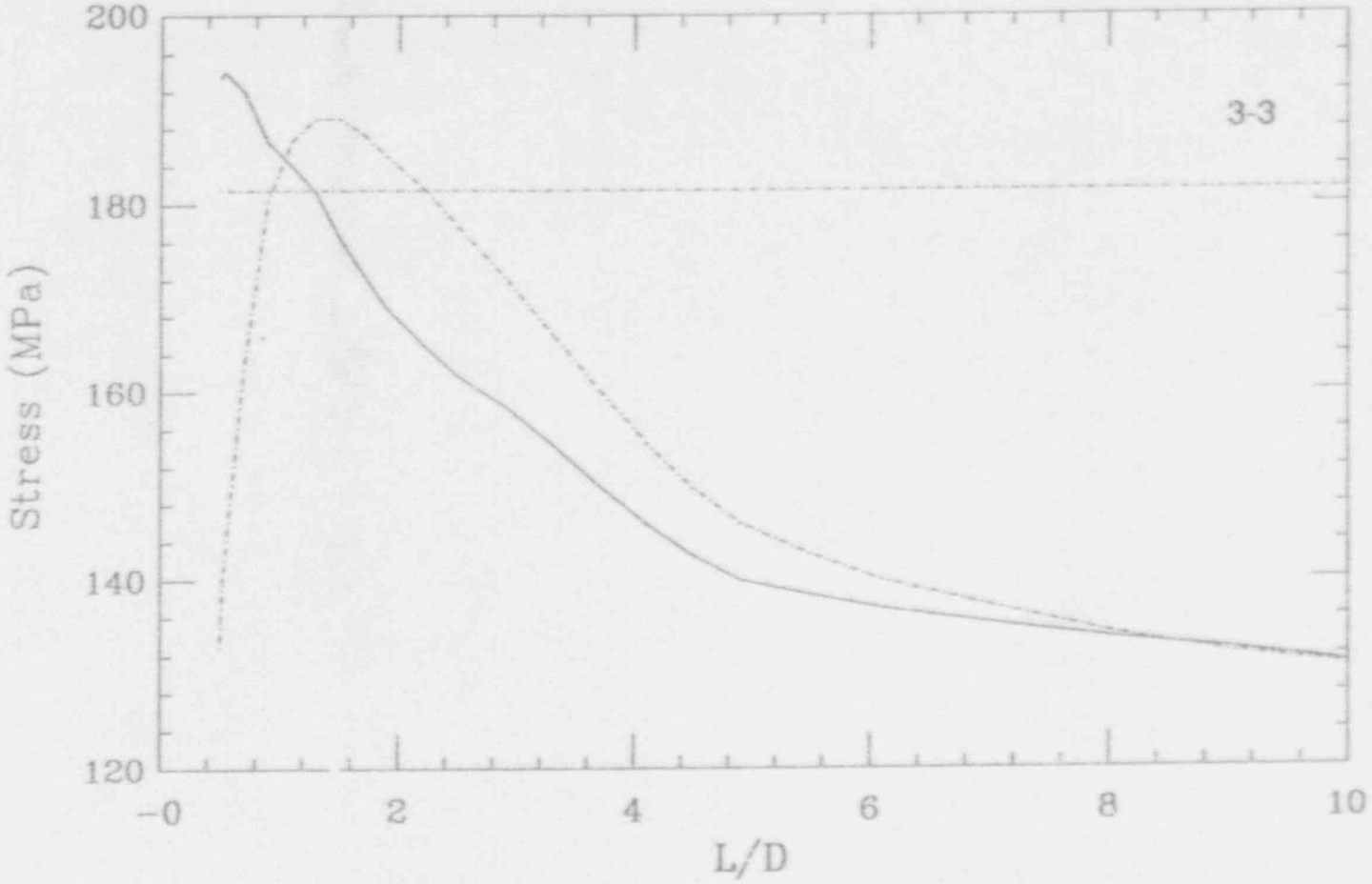
200
180
160
140
120
Stress (MPa)
3-3
0
2
4
6
8
10
L/D

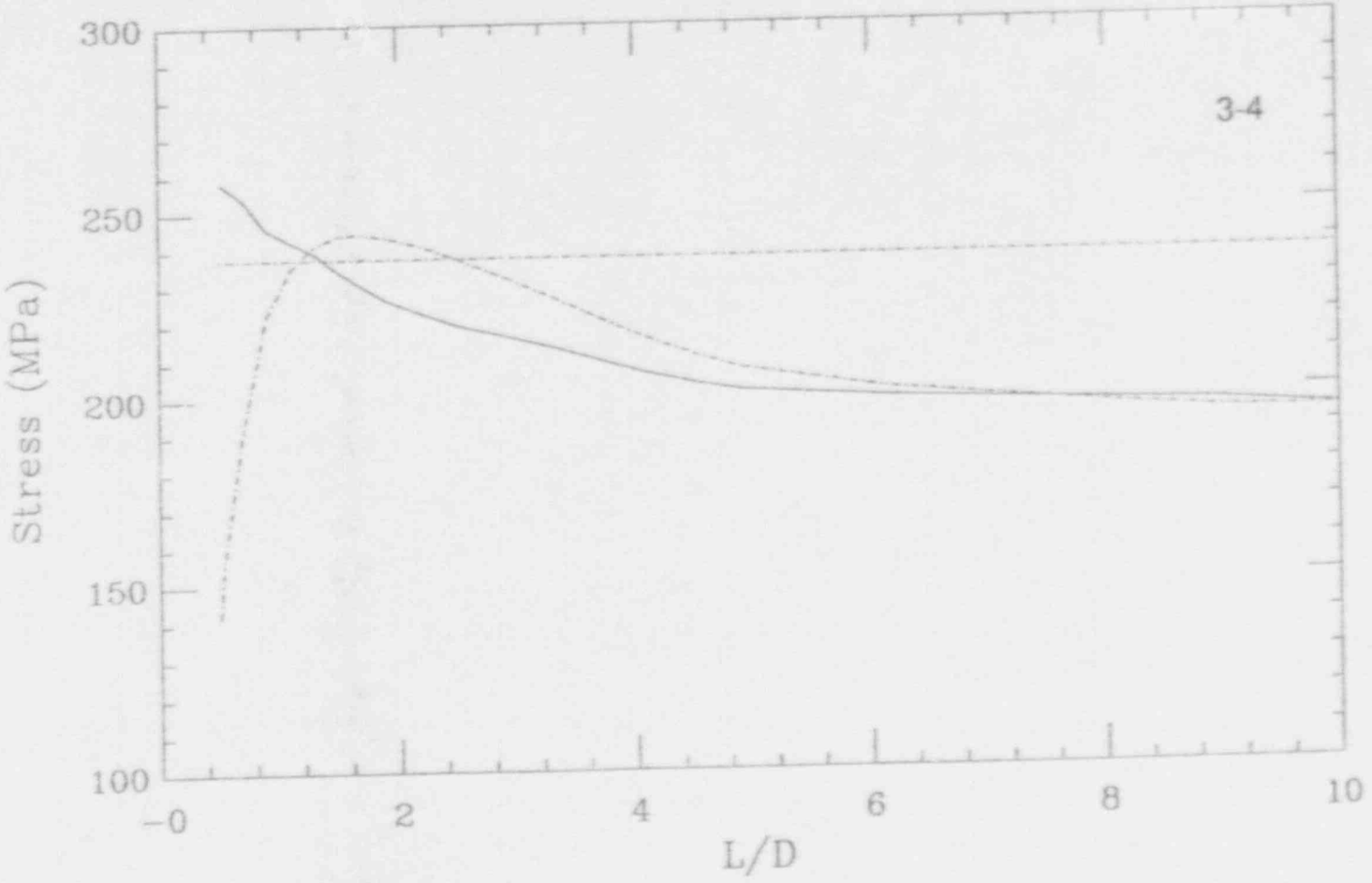
3-4
300
250
200
150
100
Stress (MPa)
-0
2
4
6
8
10
L/D

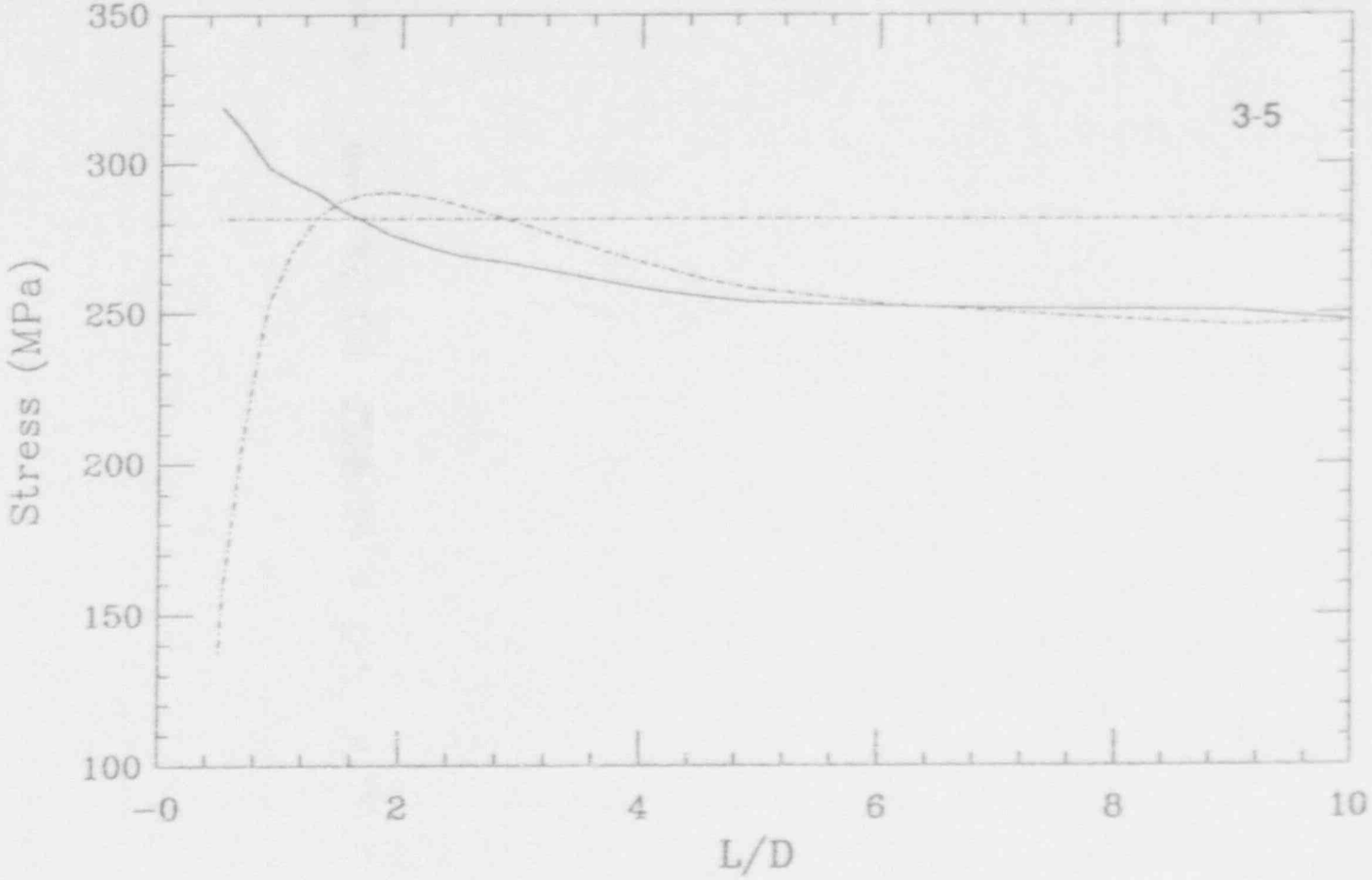
3-5
350
300
250
200
150
100
Stress (MPa)
0
2
4
6
8
10
L/D

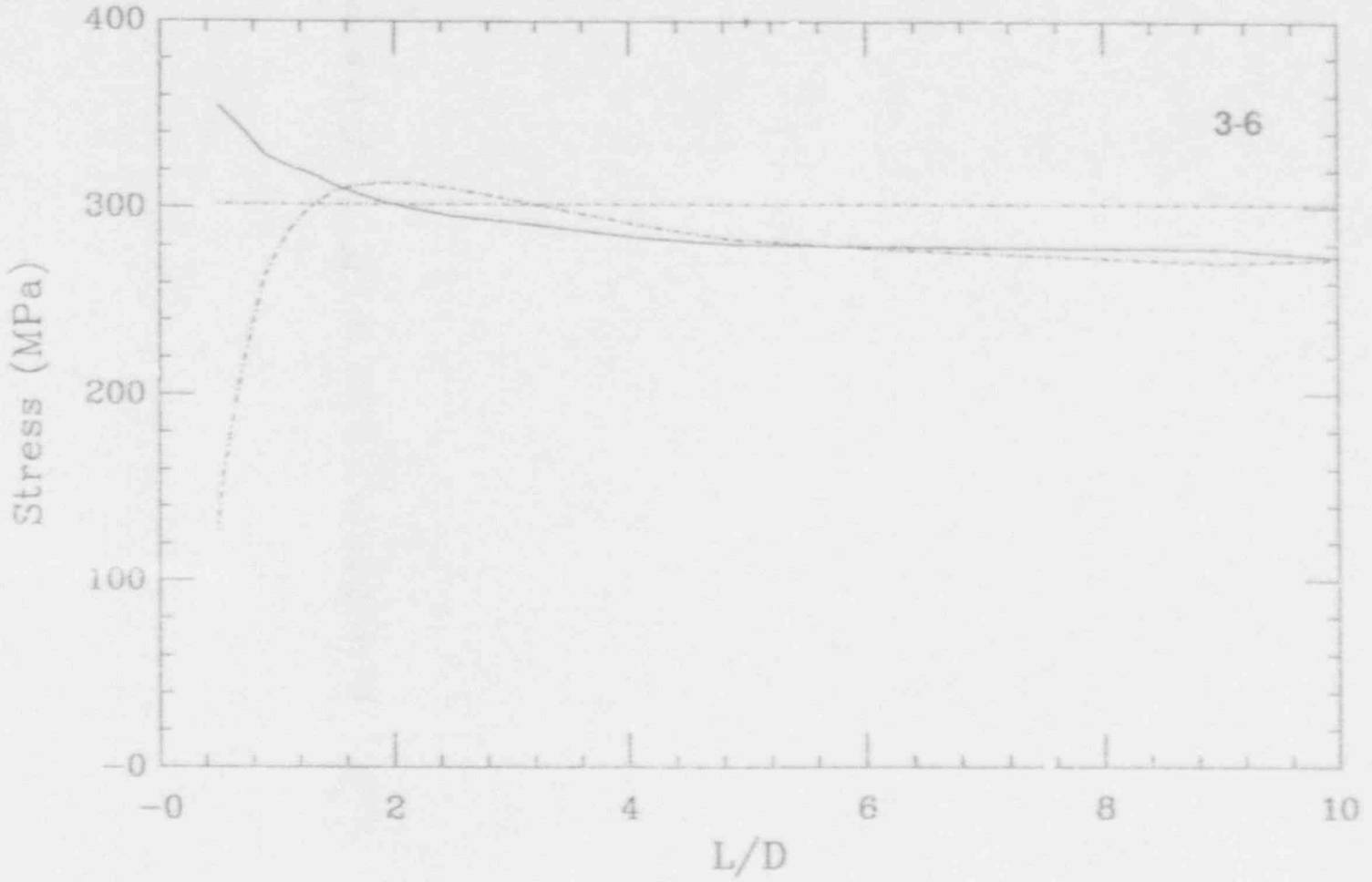
400
300
200
100
-0
Stress (MPa)
3-6
-0
2
4
6
8
10
L/D

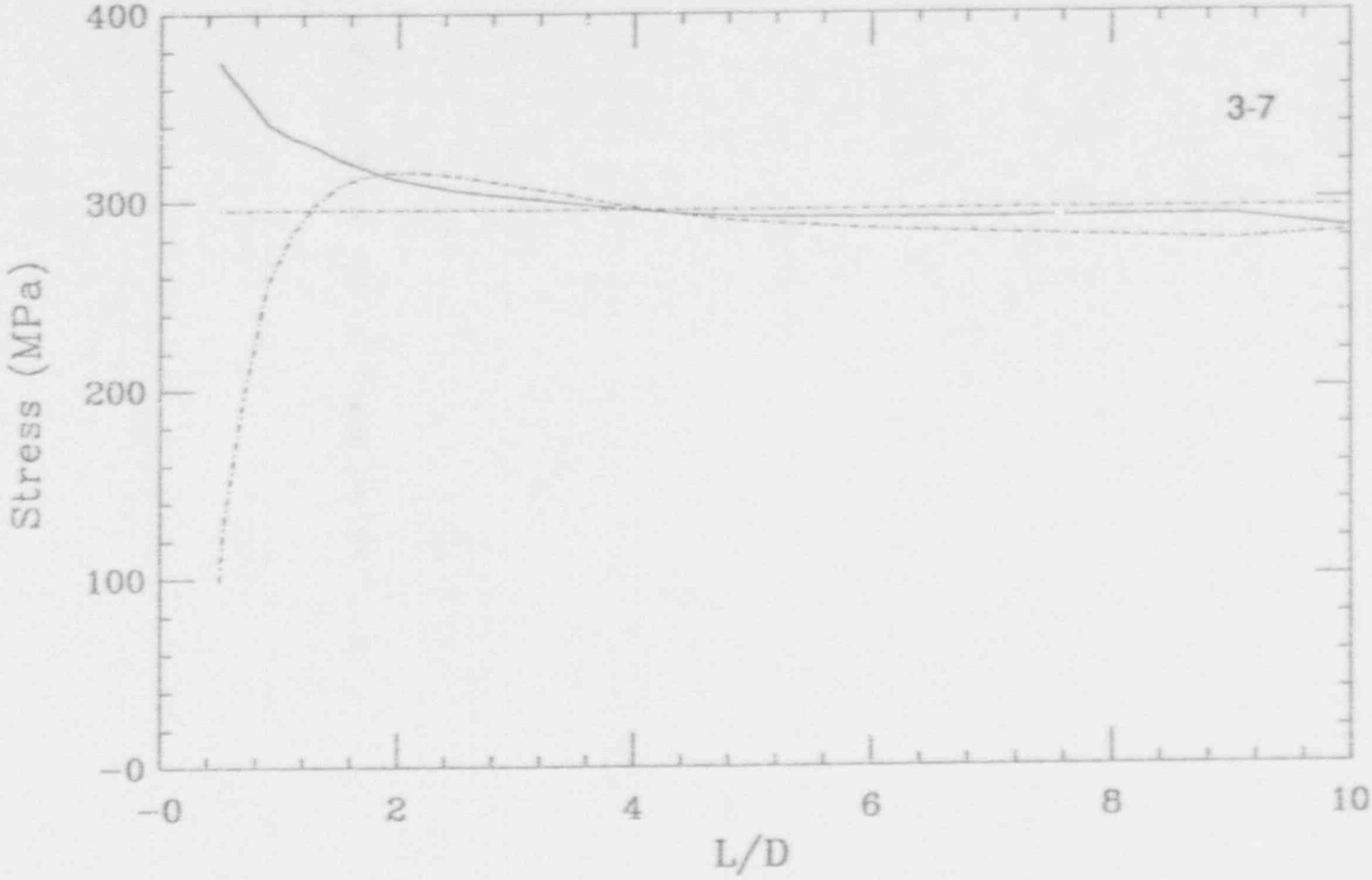
400
300
200
100
-0
Stress (MPa)
3-7
-0
2
4
6
8
10
L/D

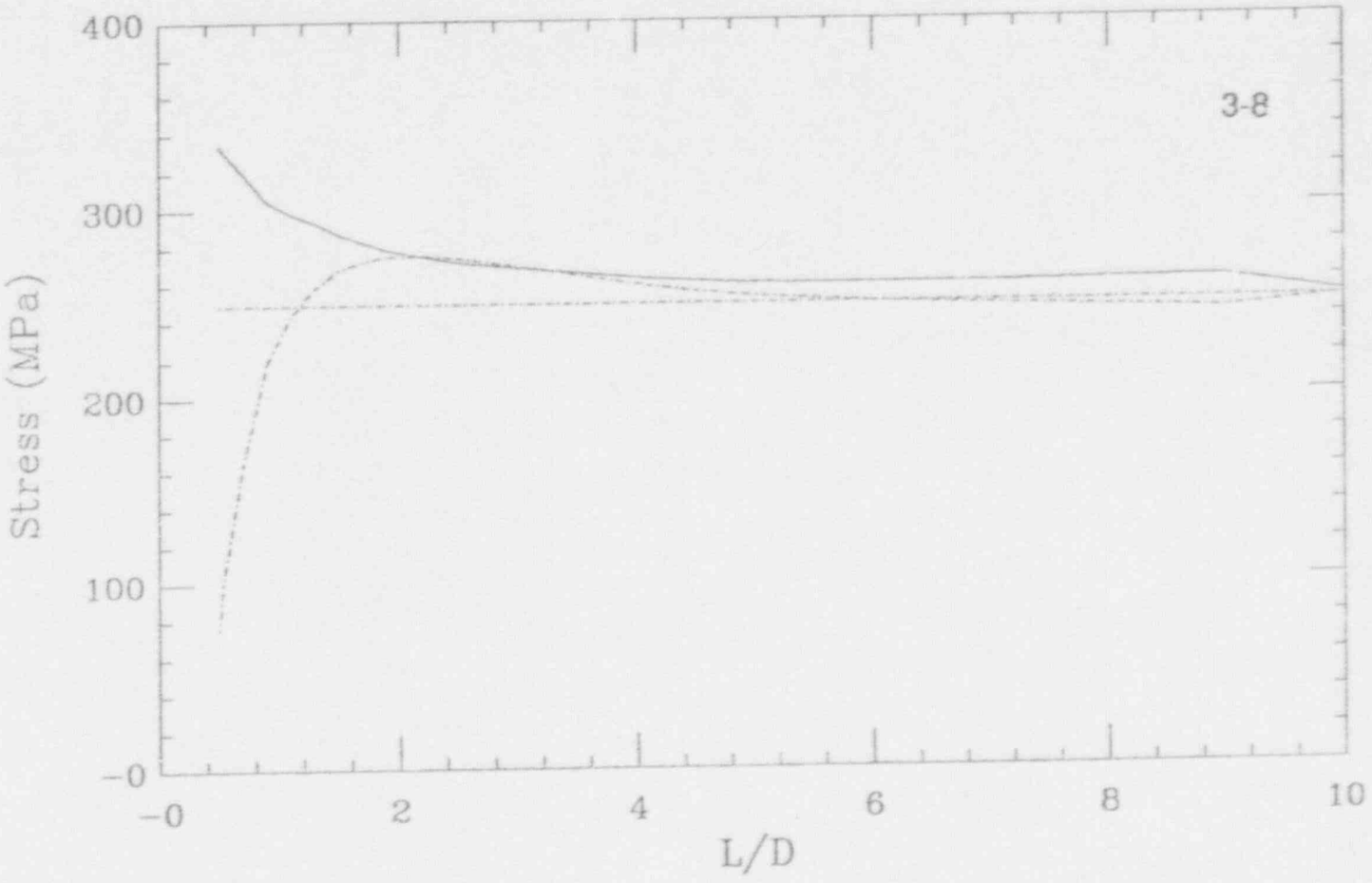
3-8
400
300
200
100
-0
Stress (MPa)
-0
2
4
6
8
10
L/D

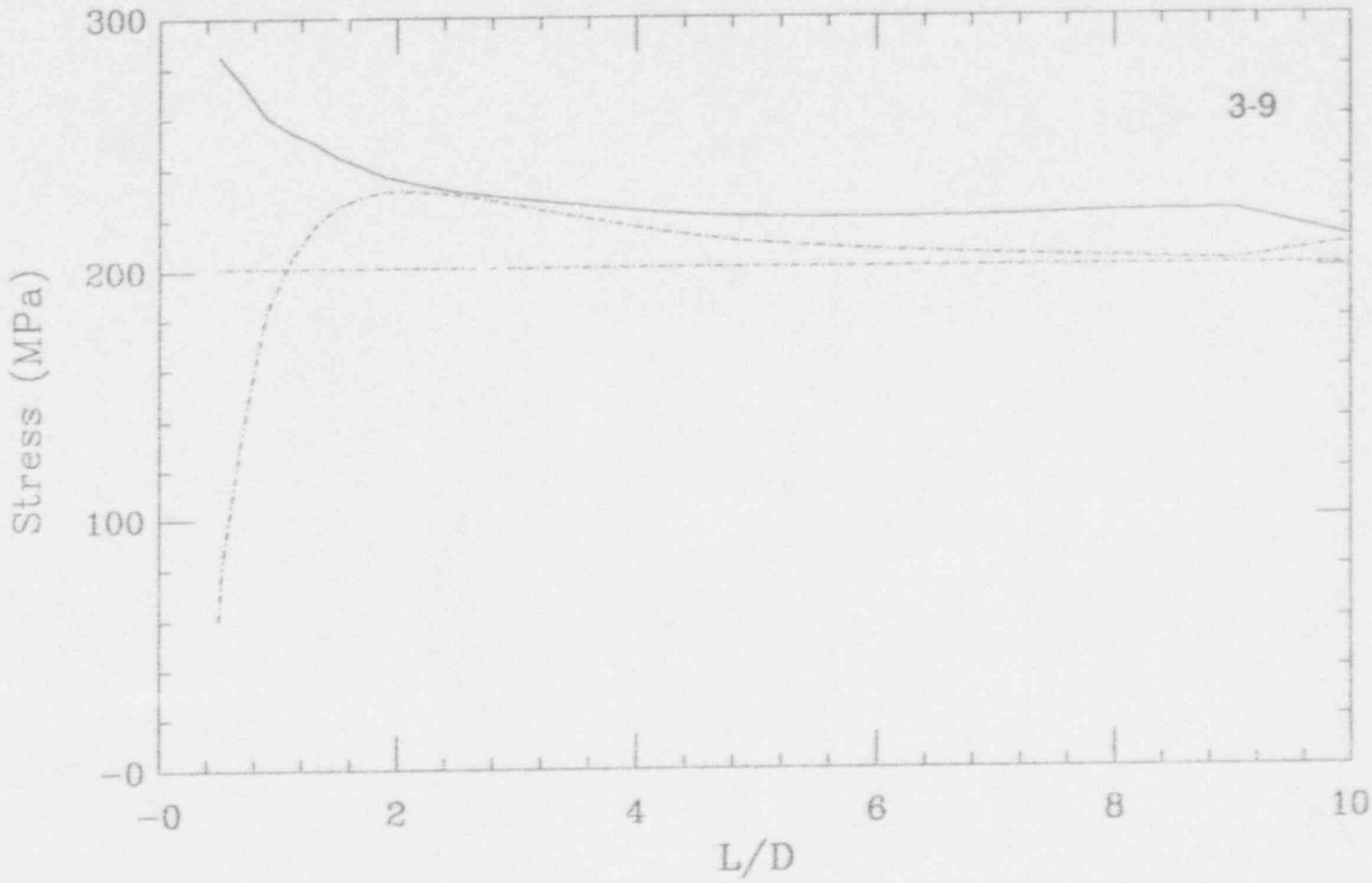
300
200
100
-0
Stress (MPa)
3-9
-0
2
4
6
8
10
L/D

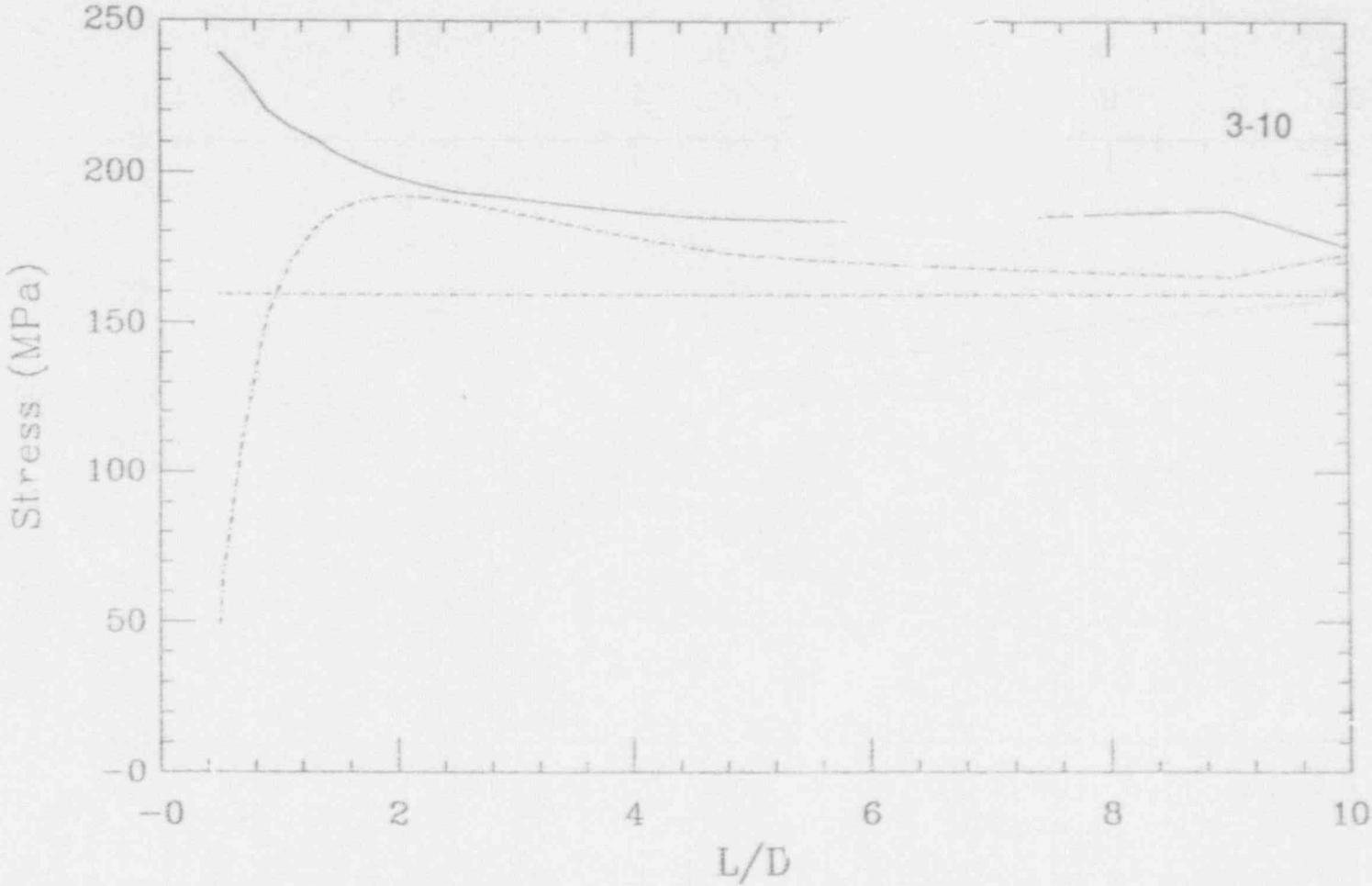
250
200
150
100
50
-0
Stress (MPa)
-0
2
4
6
8
10
L/D
3-10

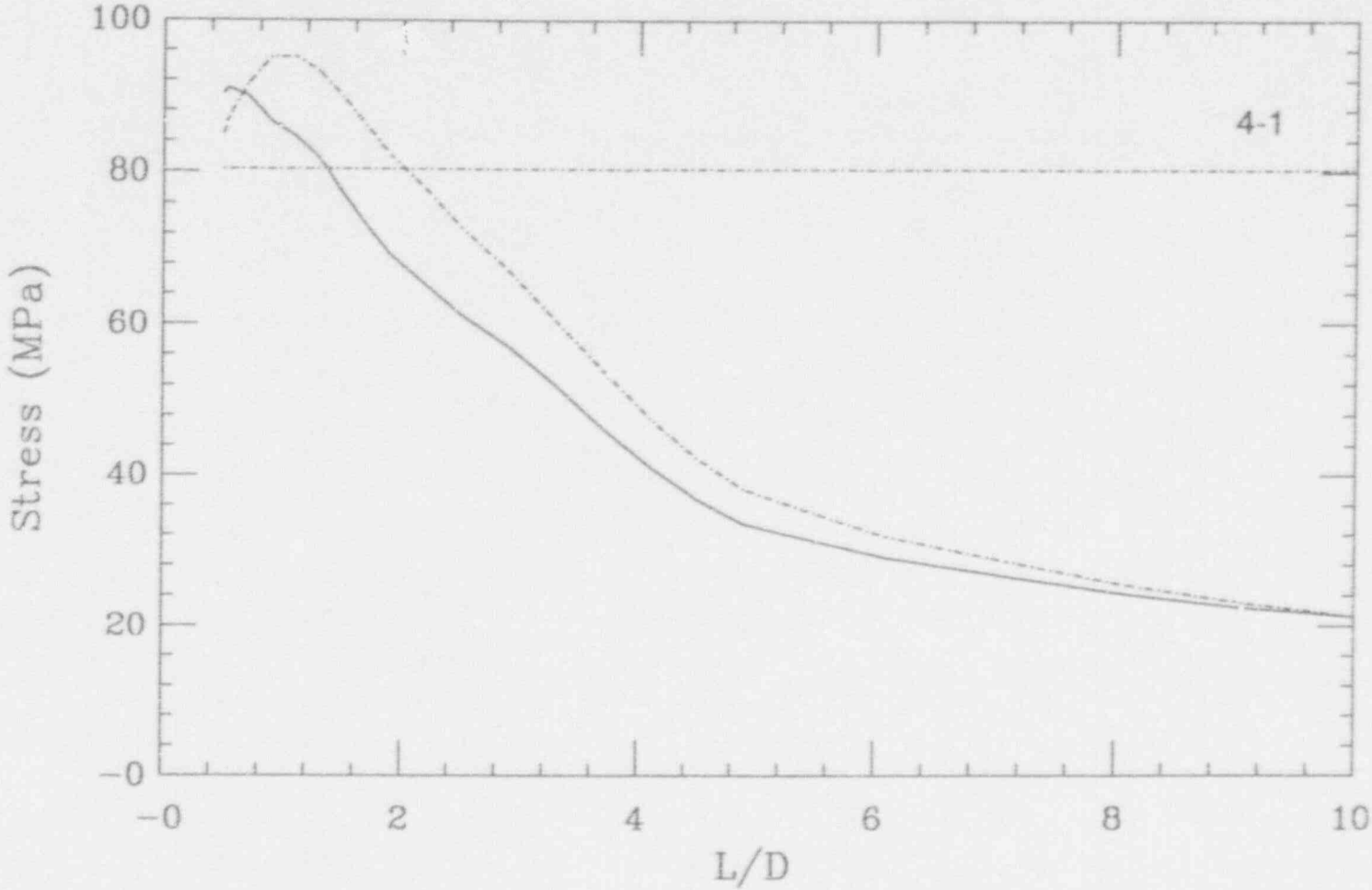
100
80
60
40
20
-0
Stress (MPa)
-0
2
4
6
8
10
L/D
4-1

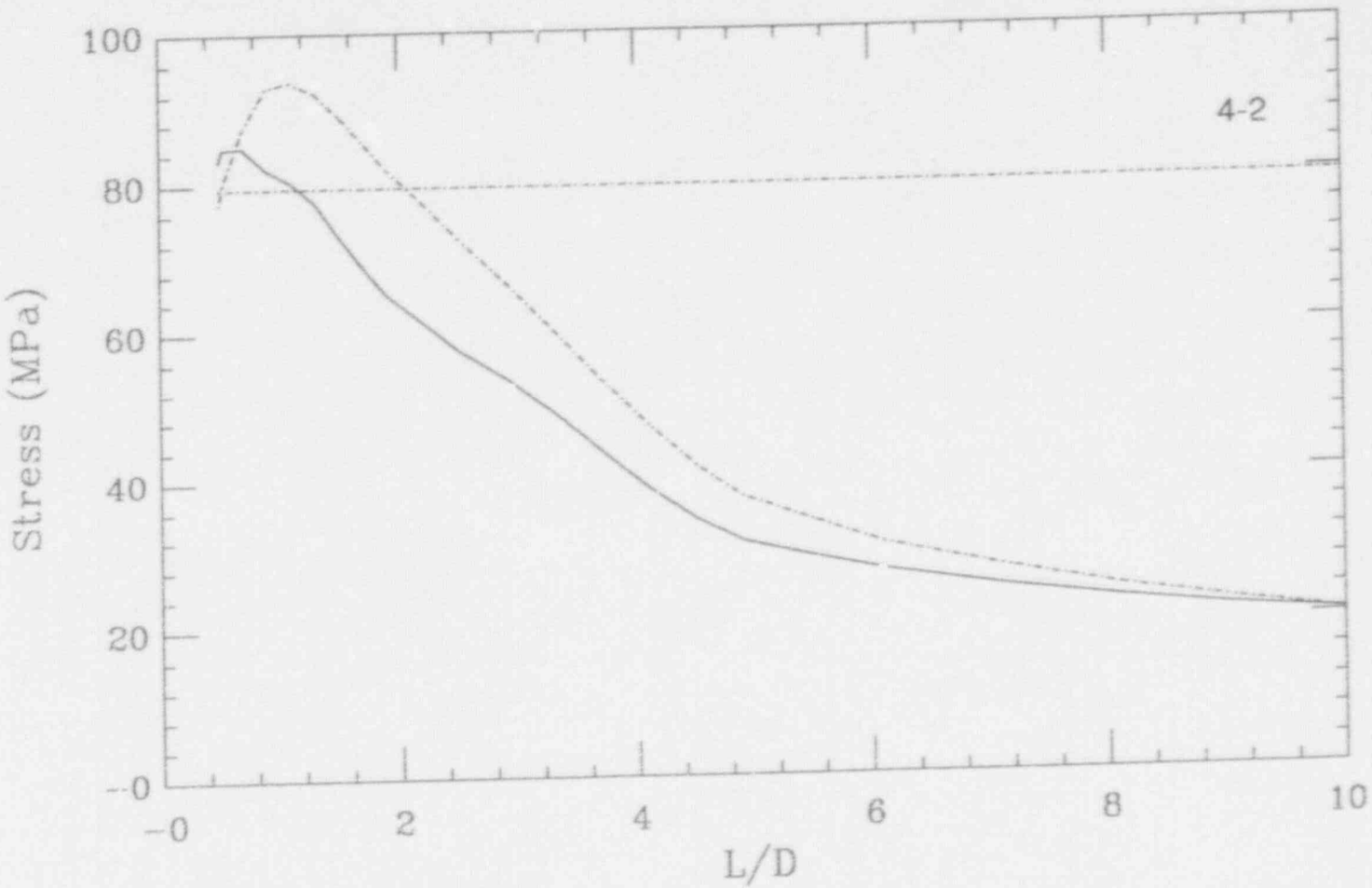
100
80
60
40
20
-0
Stress (MPa)
4-2
-0
2
4
6
8
10
L/D

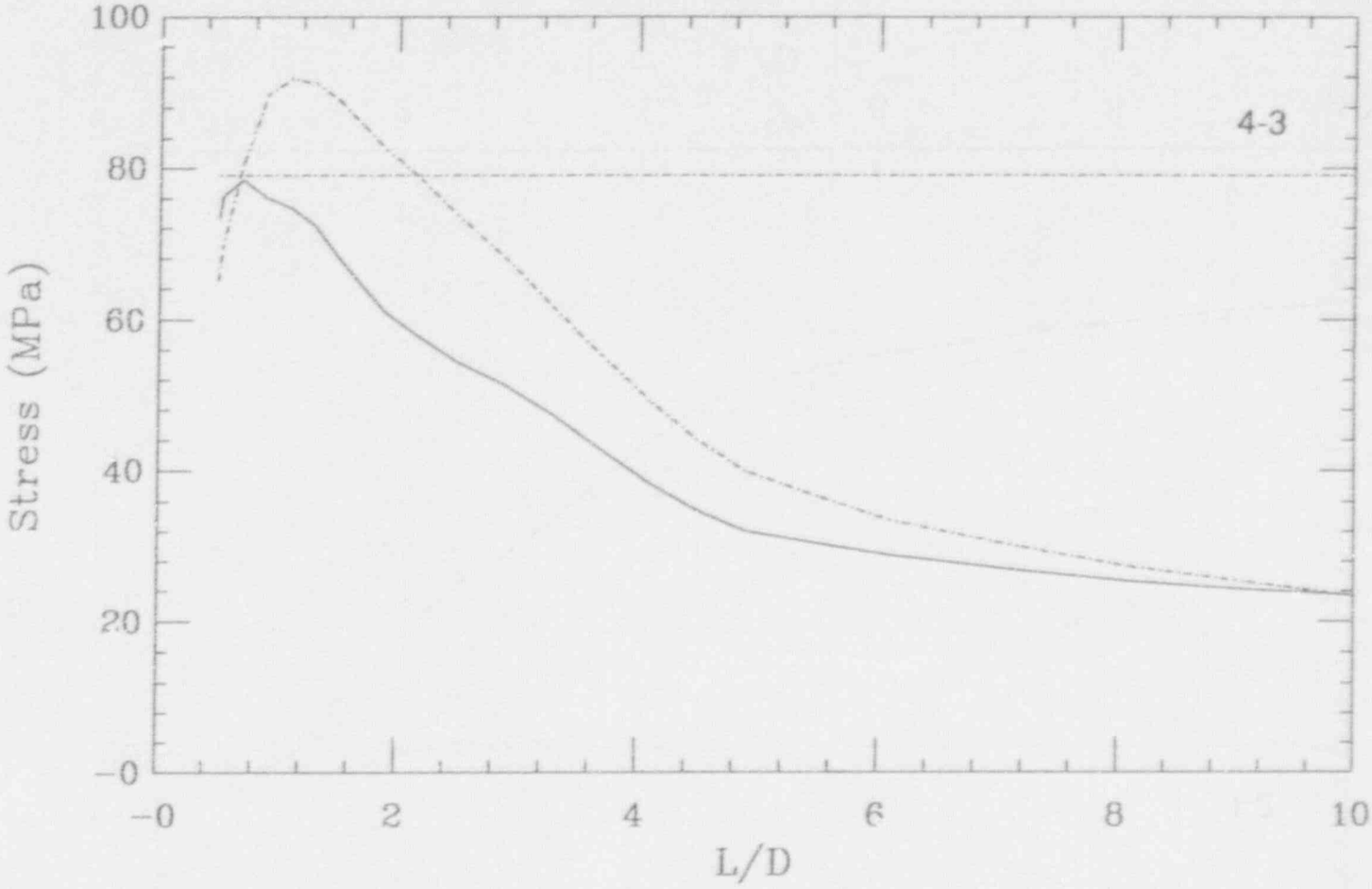
4-3
100
80
60
40
20
-0
Stress (MPa)
-0
2
4
6
8
10
L/D

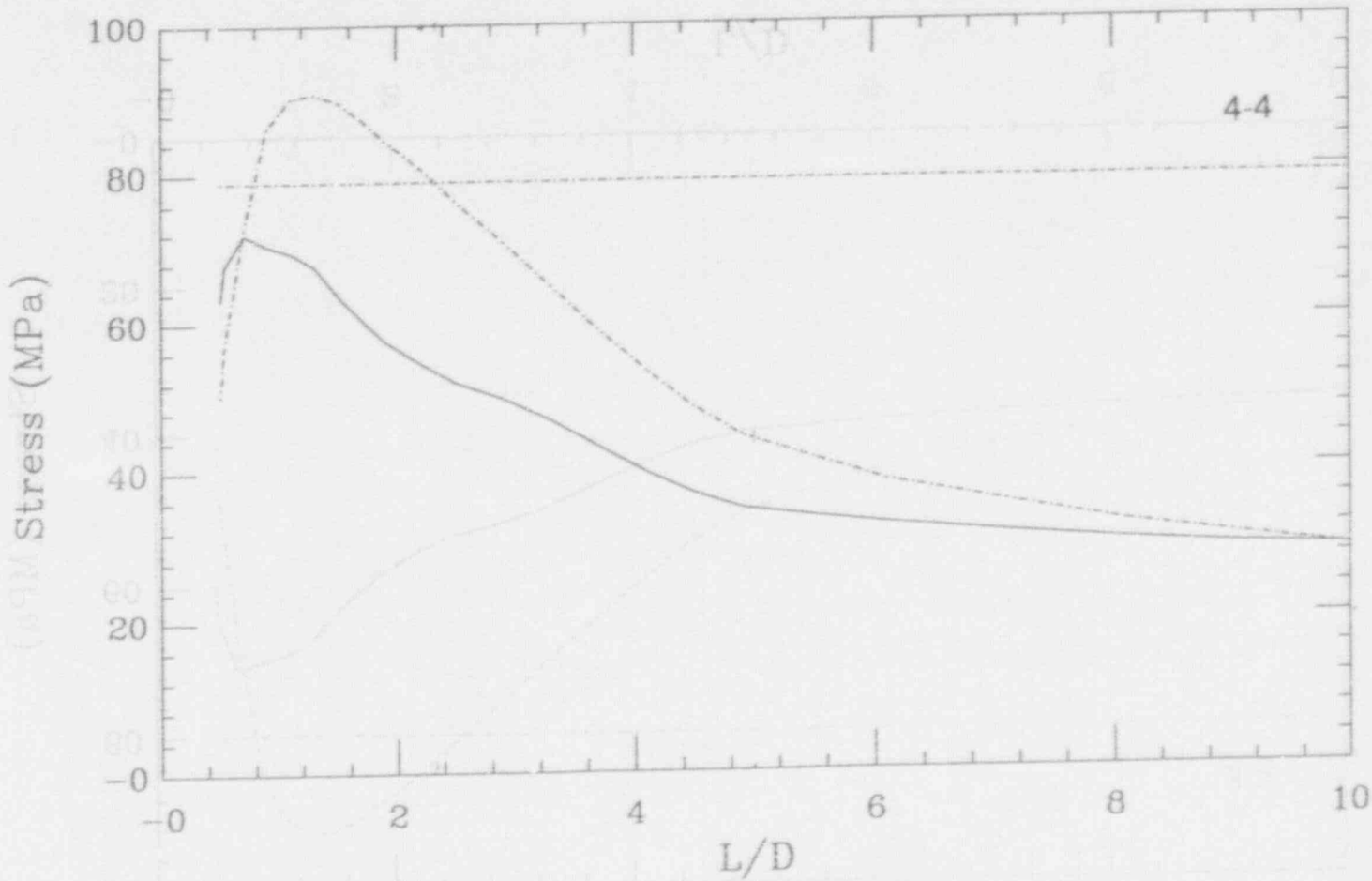
4-4
100
80
60
40
20
0
Stress (MPa)
0
2
4
6
8
10
L/D

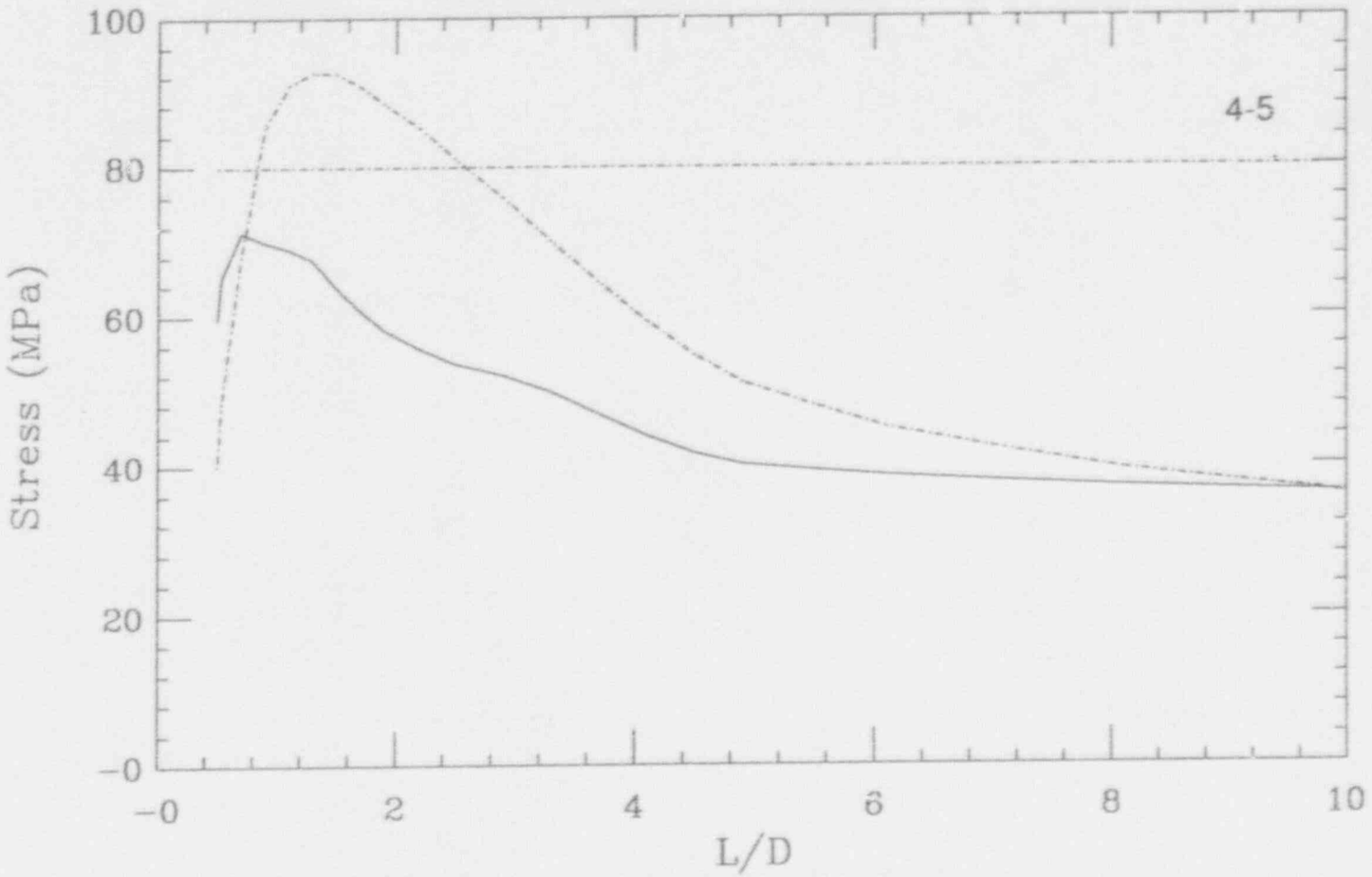
4-5
100
80
60
40
20
-0
Stress (MPa)
-0
2
4
6
8
10
L/D

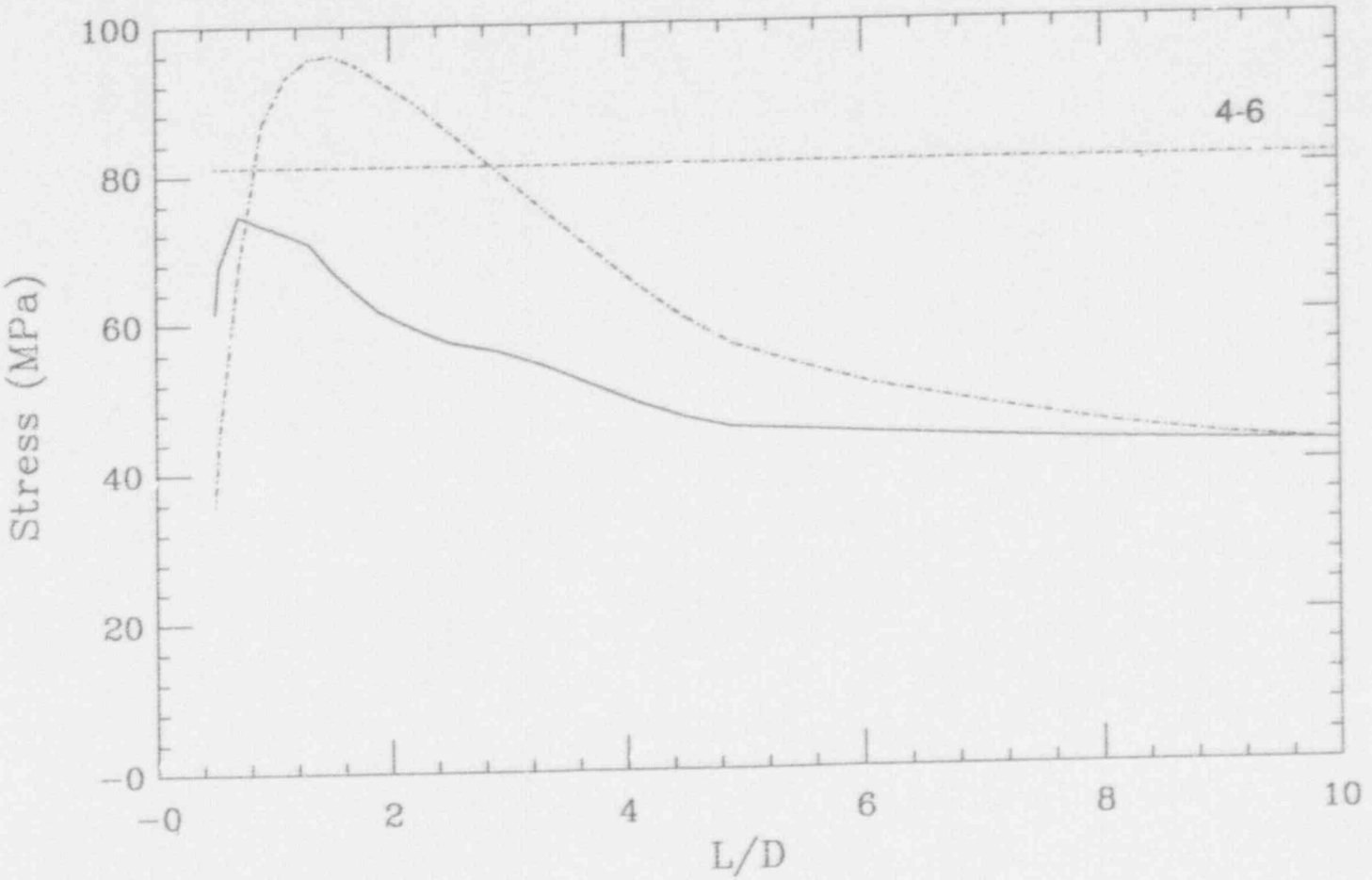
4-6
100
80
60
40
20
-0
Stress (MPa)
-0
2
4
6
8
10
L/D

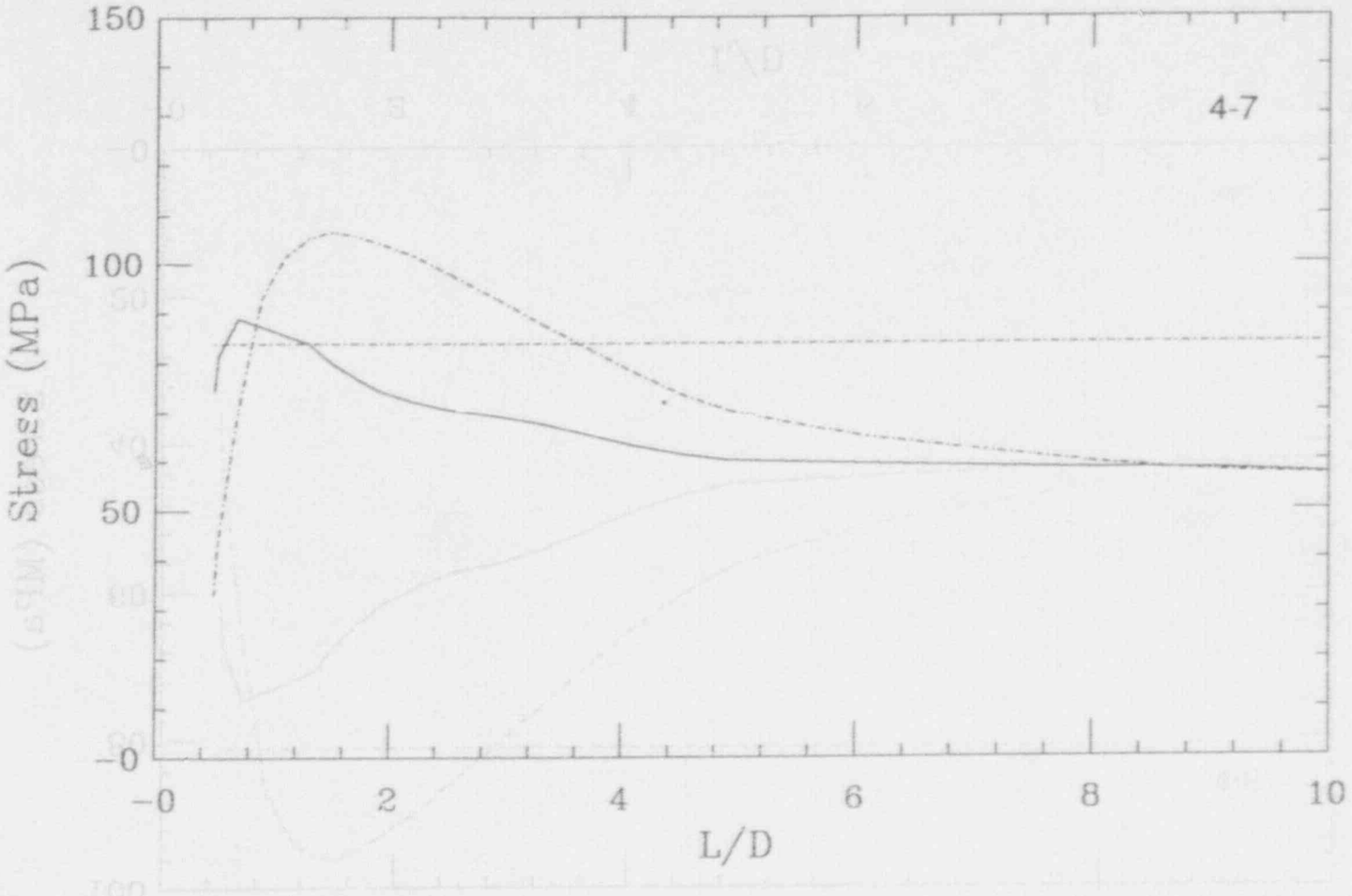
4-7
150
100
50
0
Stress (MPa)
0
2
4
6
8
10
L/D

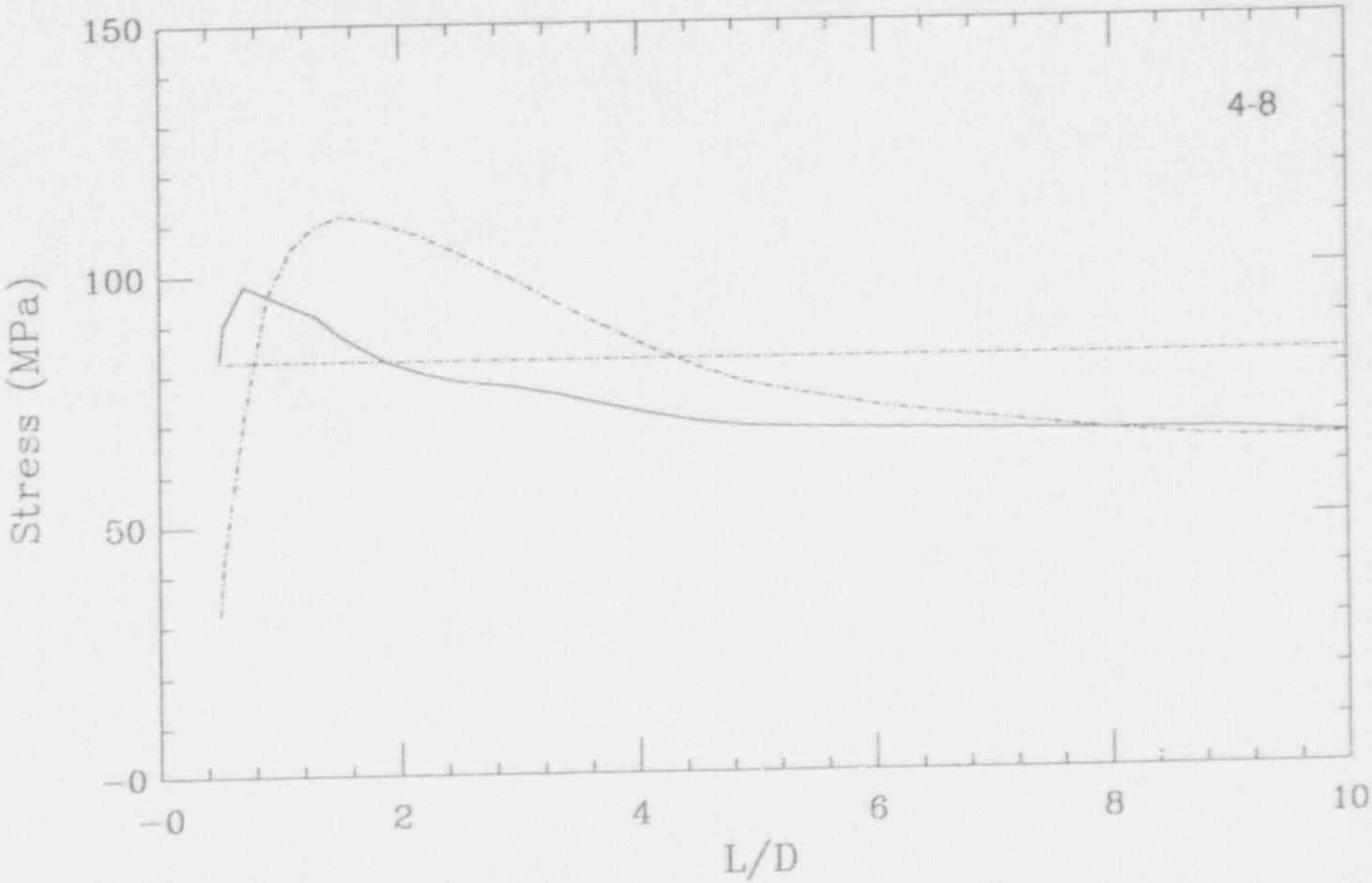
150
100
50
-0
Stress (MPa)
4-8
-0
2
4
6
8
10
L/D

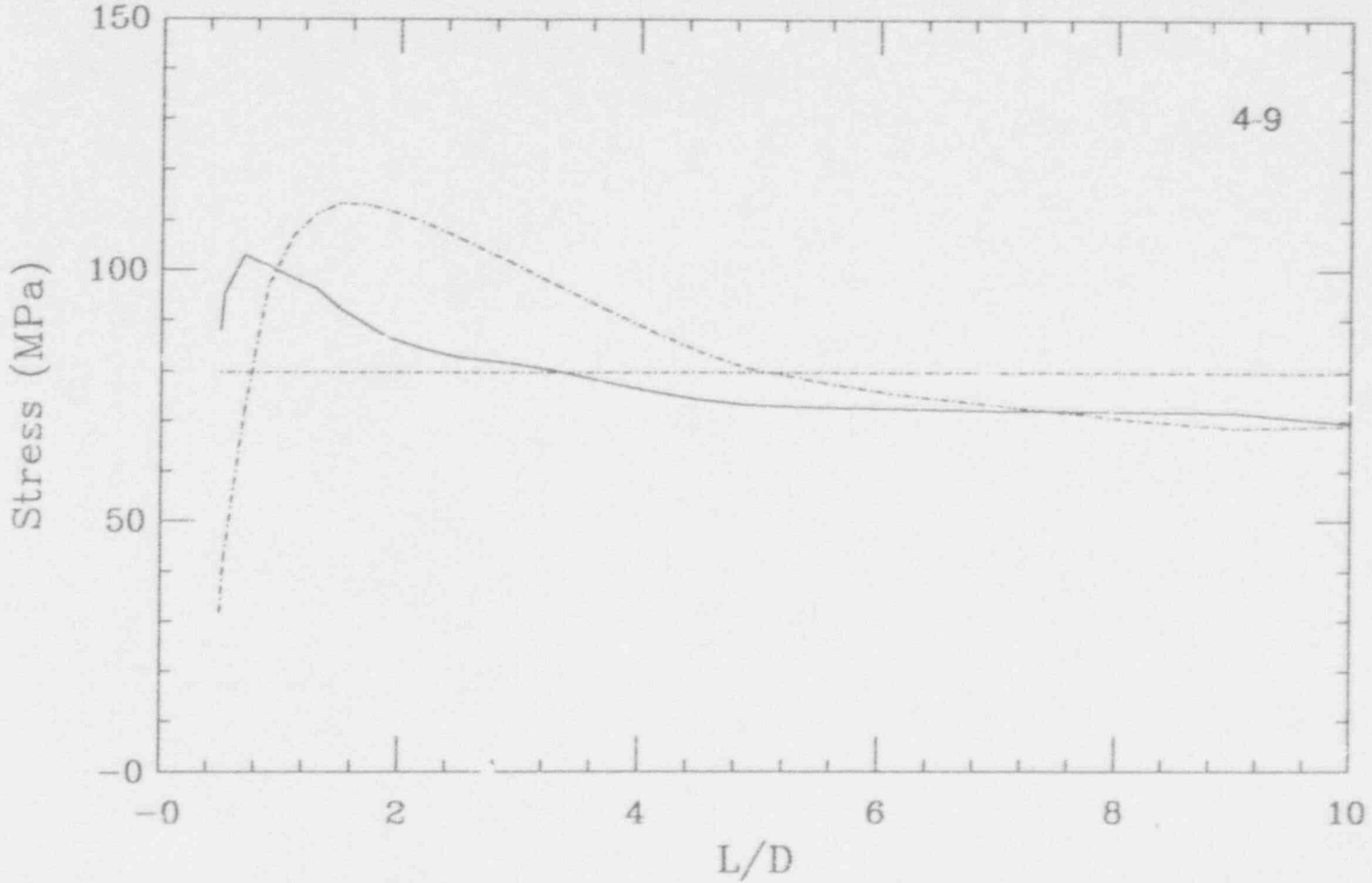
150
100
50
-0
Stress (MPa)
4-9
-0
2
4
6
8
10
L/D

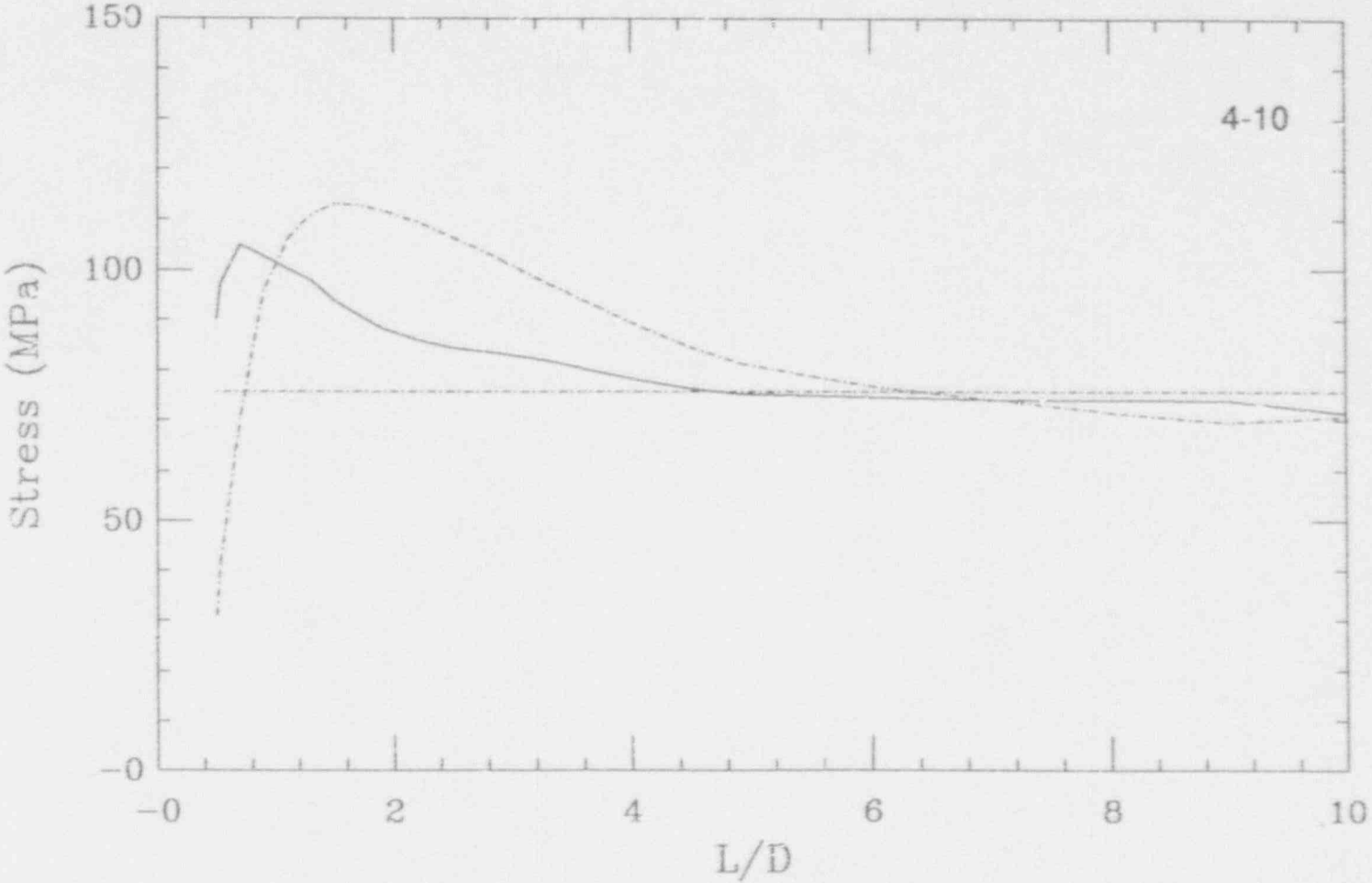
150
100
50
-0
Stress (MPa)
4-10
-0
2
4
6
8
10
L/D

NRC FORM 335 (2-89) NRCM 1102, 3201, 3202

U.S. NUCLEAR REGULATORY COMMISSION

# BIBLIOGRAPHIC DATA SHEET

(See instructions on the reverse)

1. REPORT NUMBER (Assigned by NRC, Add Vol., Supp., Rev., and Addendum Numbers, if any.)

NUREG/CR-5854

2. TITLE AND SUBTITLE

Universal Treatment of Plumes and Stresses for Pressurized Thermal Shock Evaluations

3. DATE REPORT PUBLISHED

MONTH: June YEAR: 1992

4. FIN OR GRANT NUMBER

D1634

5. AUTHOR(S)

T.G. Theofanous, S. Angelini, H. Yan

6. TYPE OF REPORT

Technical

7. PERIOD COVERED (Inclusive Dates)

8. PERFORMING ORGANIZATION – NAME AND ADDRESS (If NRC, provide Division, Office or Region, U.S. Nuclear Regulatory Commission, and mailing address; if contractor, provide name and mailing address.)

Department of Chemical and Nuclear Engineering
Center for Risk Studies and Safety
University of California
Santa Barbara, CA 93106

9. SPONSORING ORGANIZATION – NAME AND ADDRESS (If NRC, type "Same as above"; if contractor, provide NRC Division, Office or Region, U.S. Nuclear Regulatory Commission, and mailing address.)

Division of Systems Research
Office of Nuclear Regulatory Research
U.S. Nuclear Regulatory Commission
Washington, D.C. 20555

10. SUPPLEMENTARY NOTES

11. ABSTRACT (200 words or less)

The thermal field in a reactor vessel downcomer and resulting thermal/stress response in the adjacent reactor vessel wall during high-pressure safety injection are examined, especially with regard to departures from one-dimensional behavior. Similarity solutions for the stratification (in the cold leg) that creates the downcomer plumes, and scaling considerations for the thermal conduction and stress fields in the vessel wall are developed to provide generalized criteria for the adequacy of the one-dimensional treatrent.

12. KEY WORDS/DESCRIPTORS (List words or phrases that will assist researchers in locating the report.)

Pressurized thermal shock, thermal stresses, thermal mixing

13. AVAILABILITY STATEMENT

unlimited

14. SECURITY CLASSIFICATION

(This Page) unclassified

(This Report) unclassified

15. NUMBER OF PAGES

16. PRICE